Department of Imaging and Applied Physics

Curtin Institute of Radio Astronomy

A Radiometric Receiver for Measuring Red-shifted 21cm Emission from the Epoch of Reionisation

Mehran Mossammaparast

This thesis is presented for the degree of

Master of Philosophy (Physics)

of

Curtin University

March 2014

DECLARATION

To the best of my knowledge and belief this thesis contains no material previously published by any other person except where due acknowledgment has been made. This thesis contains no material which has been accepted for the award of any other degree or diploma in any university.

ABSTRACT

Radio astronomers at the forefront of cosmology are building novel instrumentation to investigate the period when the Universe was ~50 to ~900 million years old, a time when structures developed in the previously uniform, gaseous medium to form the first stars and galaxies. Observing this period, between the cosmic recombination and the Epoch of Reionisation (EoR) during which hydrogen was ionised by radiation from the first stars and galaxies, requires state-of-the-art radio receiver systems.

This thesis presents design, construction and testing of a specialised, low noise, radiometric receiver optimised for EoR experiments. This project is aimed at designing the optimum radiometer configuration to achieve calibration stability below 100 mK, followed by building and testing a compact receiver to demonstrate the design. The radiometer may be operated in different radiometric modes such as total power, noise adding, comparison switched or hybrid mode.

The receiver design was extensively researched for development before its implementation. Subsequently, the prototype receiver performance has been comprehensively and meticulously measured and examined. The radiometric receiver characteristics were then analysed in terms of RF performance, noise temperature, radiometric resolution and temperature stability to provide required and sufficient information most useful for an EoR experimental system.

The radiometer receiver is enclosed in an aluminium RF-sealed enclosure to minimise susceptibility to EMI. The thermal mass of the box also serves to reducing internal temperature changes caused by ambient temperature variations; thus helping to stabilise the radiometer components. The receiver also monitors the temperature of the critical RF radiometer sections so that an external processing unit can assess and possibly correct for some variations. In addition, the receiver design includes integrated temperature control circuitry. Once the thermal behaviour of the radiometer is measured, and studied in the field trials, a thermal control strategy can then be determined and implemented to regulate the internal thermal environment.

Finally, the radiometer stability test using a hot load at 6778.3 K showed the detector output voltage was stable, and gave a standard error of mean of 1.02 K. The sensitivity limitation may be attributed to the limited integration time (~10ms) and bandwidth of the on-board rms detector in the receiver. The radiometric receiver is expected to achieve a 100 mK resolution for a 9 day of observation once integrated into an experimental EoR system.

PUBLICATIONS AND PRESENTATIONS

[1] Mossammaparast, Mehran; Wayth Randall; Tingay, Steven; Hall, Peter; Staveley-Smith, Lister; Waterson, Mark, Clarke, Nathan; Jiwani, Aziz and Roberts, Paul Roberts (2011) BIGHORNS: Broadband Instrument for the Global HydrOgen ReionisatioN Signal, *SKA-LOW Workshop, Poster*.

[2] Mossammaparast, M. (2012). The BIGHORNS Radiometric Receiver. *CAASTRO EoR Global Signal Workshop*.

ACKNOWLEDGEMENTS

There are several people I would like to thank and acknowledge their assistance during my project.

Firstly, I am extremely grateful and indebted to my wife for her ongoing and loving support during the course of the project.

Secondly, I wish to express my immense appreciation and deepest gratitude to my supervisors Dr Randall Wayth, Prof Steven Tingay and Prof Peter Hall for their continuous support and words of encouragements.

As an experienced radio engineer, I can appreciate that the build and development of a global signal project such as the BIGHORNS (Broadband Instrument for measuring Global Hydrogen ReionisatioN Signal) is a team effort and requires different team members to fulfil different roles. My sincere thanks go to the brilliant BIGHORNS team members Dr Randall Wayth, Dr Steven Tremblay, Dr Marcin Sokolowski who aided me during the development of the receiver hardware, pointing out the critical aim of this radio astronomy project, the associated issues and challenges and helped developing the overall system architecture. My earnest thanks also go to the ICRAR (International Centre for Radio Astronomy Research) Lab team of engineers and technicians at Curtin University especially to Mr Mark Waterson for his invaluable engineering inputs in the hardware design as well as during the writing of the thesis.

I would also like to extend my gratitude to Prof Bryan Gaensler, CAASTRO (the ARC Centre of Excellence for All-Sky Astrophysics) director, who provided the initial funding for the project. I am proud to be part a student member of CAASTRO, an elite group of researchers and innovators in the field of astronomy and astrophysics.

In addition, I would like to offer my appreciation to my CAASTRO mentor, Prof Frank Briggs at ANU, who I met briefly in a workshop and be friended with straightaway. I am extremely grateful to him for his expert and sincere guidance and encouragement extended to me during the writing of the thesis.

Furthermore, I would like to thank my manager, Jesse Searls at Poseidon Scientific Instruments (now Raytheon Australia) who has supported me

wholeheartedly to pursue my higher education degree in the field of radio astronomy while I was working full time during the last three years. I would like to acknowledge the support of the Raytheon management who allowed me the use Poseidon laboratory and equipment day and night to carry out the time-consuming and days-long tests. To my colleague, Nigel Gaylard, who helped me in the build of the controller board and microcontroller programming. My sincere gratitude to the Poseidon crew who assisted in the assembly and debugging of the hardware prototypes. And last but not least, to Fritz Berrer at Technical and Mechanical Innovations, WA, who populated the PCB prototypes with absolute care and uncompromising attention to details.

TABLE OF CONTENTS

LIST OF FIGURES

LIST OF TABLES

ABBREVIATIONS

ADC	Analog to Digital Converter
BIGHORNS	Broadband Instrument for measuring Global Hydrogen ReionisatioN Signal
CAATSRO	ARC Centre of Excellent for All Sky Astrophysics
CMB	Cosmic Microwave Background
COBE	COsmic Microwave Background Explorer
CoRE	Cosmological Reionisation Experiment
DAQ	Data Acquisition unit in the BIGHORNS back-end rack
EDGES	Experiment to Detect the Global EoR Signature
EMI	Electro Magnetic Interference
ENR	Excess Noise Ratio
EoR	Epoch of Reionisation
ICRAR	International Centre for Radio Astronomy Research
IGM	Intergalactic Medium
LabVIEW™	Laboratory Virtual Instrument Engineering Workbench, National Instrument system design software platform
LOFAR	LOw-Frequency Array for Radio astronomy
MCU	Master Control Unit in the BIGHORNS back-end rack
MWA	Murchison Widefield Array
NACR	Noise Adding Comparison Radiometer
NAR	Noise Adding Radiometer
PCB	Printed Circuit Board
PIC™	Programmable Interface Controller, Microchip Technology
PNA-X	Agilent high Performance Network Analyser
PSU	Power Supply Unit in the BIGHORNS back-end rack

R&S	Rohde & Schwarz network analyser
RF	Radio Frequency
RFI	Radio Frequency Interference
rms	Root Mean Square
RSSI	Receiver Signal Strength Indicator
SKA	Square Kilometre Array
SM	Surface mount
SMD	Surface Mount Device
TPR	Total Power Radiometer
VNA	Vector Network Analyser
VSWR	Voltage Standing Wave Ratio

CHAPTER 1

1 Introduction

An expanding Universe that originates in a hot Big Bang will cool as it expands. Cooling leads to the Recombination Epoch when the ionised matter created in the Big Bang recombines to make a uniform medium of mostly hydrogen and helium atoms, an evolutionary stage that gives rise to the Cosmic Microwave Background (CMB) (Gawiser & Silk, 2000). Subsequent expansion and further cooling allows gravitational collapse leading to formation of the first stars and galaxies whose radiation progressively ionises the nearby neutral hydrogen atoms. This period is known as the Epoch of Reionisation (EoR) (Zaroubi, 2012), and the effect is profound, since once reionised, the Intergalactic Medium (IGM) has been so diluted by the expansion that it remains ionised until the present (S. Furlanetto, Oh, & Briggs, 2006).

Radio astronomers are playing a key role in the study of the EoR, since neutral hydrogen emits a distinct spectral line, the 21 cm line, which becomes red-shifted to radio frequencies below 200 MHz for redshifts $z > 6$ (S. Furlanetto et al., 2006). As the first stars and galaxies form during this epoch, they change the excitation temperature of the neutral hydrogen, T_S, the spin temperature and can cause the emission line to appear in emission or absorption against the CMB. Today, cosmologists can learn when and how the reionisation process happened by studying the presence or absence of this emission line. Telescopes such as the Murchison Widefield Array (MWA) (Lonsdale et al., 2009; Tingay et al., 2013) and Low-Frequency Array for radio astronomy (LOFAR) (van Haarlem et al., 2013) have been designed to detect spatial structure in the 21 cm line, but the reionisation is expected to affect the whole Universe synchronously, leading to what is generally referred to as the "global signal", which comes from the whole sky (P.A. Shaver, Windhorst, Madau, & de Bruyn, 1999). The sky averaged global signal is extremely weak compared to other sources of radio emission from the sky such as Galactic emission. As such, it makes the measurement challenging and requires a stable and well-calibrated antenna and receiver system.

This thesis provides a detailed design and implementation of a low noise radio receiver for measuring the sky averaged red-shifted 21 cm line of neutral hydrogen (HI) during the EoR.

1.1 Aim

The aim is to design, develop and calibrate a low noise radiometric receiver in the radio frequency band between 50 and 250 MHz, corresponding to redshift $5< z < 25$, to measure the averaged all-sky spectrum. The design of the radiometric receiver is based on a hybrid of a comparison switch (Dicke, 1946) at the antenna input and a noise adding type radiometer, in addition employing temperature compensation techniques. In this work the radiometer calibration is based on measurements of a calibrated noise source and an internal blackbody reference operating in a comparison switched mode.

This portable battery operated receiver, combined with a frequency independent antenna and a high speed digital back-end system, could be deployed at a radio quiet site to search for the global signature from the averaged all-sky spectrum. The successful execution of this experiment could help identify the nature of structure formation for the first luminous sources, processes of reionisation as well as complementing other techniques in cosmology (Barkana & Loeb, 2005; S. R. Furlanetto, Zaldarriaga, & Hernquist, 2004).

The primary motivation for the development of this radiometric receiver is the BIGHORNS project, which is a CAASTRO supported project led by Curtin University, to detect the faint 21 cm global signature of neutral hydrogen (HI) prior to and during the EoR. These observations are extremely challenging as the 21 cm global signal is predicted to be much weaker than foreground signals, by a factor of order 10^5. Hence, the stability and sensitivity requirements of the whole system are stringent in this experiment. In the radiometric receiver alone, to achieve this level of sensitivity demands that critical radiometer components be designed, constructed and monitored with a high degree of accuracy and care. By closely monitoring the physical temperature of the radiometer components, such as the internal reference sources, input coupler, and RF switches of the receiver front-end, it is expected that the instrumental artefacts due to the amplifier gain and noise variations within the band can be compensated for.

A resolution in the order of 100 mK for a week of integration time is initially targeted for the radiometer. Furthermore, it is expected that once the radiometer is employed in the BIGHORNS system and exercising a temperature compensation technique in the receiver, this resolution can be reduced to under 10 mK for long integration times of a week-long or more.

1.2 Thesis outline

This thesis consists of five chapters followed by a conclusion. A brief outline of the work contained in this thesis is given below on a chapter by chapter basis.

In chapter 2 a short literature review of the observation and physics of the Epoch of Reionisation is presented in order to set the context in which this work should be viewed. Some observational constraints obtained using other probes of the intergalactic medium are briefly discussed, followed by a discussion of the 21 cm global signal as an ideal probe of the intergalactic medium during the epoch of reionisation. The goal of this work is to contribute to the understanding of the Epoch of Reionisation through observation of the 21 cm global signal.

The design of a radiometric receiver appropriate for this application is introduced in chapter 3. A general description and different type of radiometers will be presented and compared based on their resolution. This is followed by the detailed description of the radiometer chosen for this experiment.

Chapter 4 delivers the detailed hardware designs and architecture of the receiver sub-assemblies methodically. The build and construction require careful attention to every aspect of the receiver design and choice of components. This includes the components in the radiometer section to amplifiers, regulators and detectors in the following stages of the receiver chain. All the key components in the receiver have been chosen carefully for low noise, high dynamic range, excellent stability and low power dissipation. In some cases, different types of components have been selected and tested to find a suitable one.

Chapter 5 presents the receiver RF characteristics and thermal testing of the radiometer measured in a controlled laboratory environment to determine its thermal characteristics as well as short and long term stability. The receiver performance has been carefully evaluated over the temperature range of 10 ºC to 50 ºC and the frequency range of 50 to 250 MHz and the individual radiometer

subsystems have been characterised. The results would help developing a receiver stabilisation technique to compensate for temperature variations during long integration time in the BIGHORN system. The standard error of the mean and Allan deviation have been used to determine the uncertainty in the sample mean of the input load as measured by the internal RF detector in the laboratory.

Furthermore, the main characteristics of the radiometric receiver designed and developed in this project are summarised in Table 1.

Table 1 Radiometer receiver parameters

Parameter	Value
Receiver noise temperature	214K between 50-250 MHz
Gain flatness (50 – 250 MHz)	Front-end module: 36.4 ± 0.6 dB Gain module: 41.5 ± 0.5 dB
Gain Adjustment	0 to 30 dB in 0.5 dB steps
Instrument control and monitor	x3 Temperature sensors: T1, T2, T3 x1 Humidity sensor: H Voltage and Current monitors Receiver gain adjustment Radiometer noise injection adjustment
Input DC voltage & Current	15 to 18V at 700mA
Measured radiometric resolution over 6 hours, ΔT_m	1 K @ T_{hot} = 6778 K
Front-end Dicke switching rate	0 to 65535 in 0.25sec step
RS485 communication data rate	32kbps

In conclusion, a summary and recommendations for future research will be presented.

In addition, a mathematical derivation of the radiometer output has been presented in Appendix A. The top level diagrams of the receiver printed circuit boards (PCBs) are included in Appendix B. Included in Appendices C and D are the main software codes written in Matlab and LabVIEW™ computer packages for simulating, testing and calibrating of the radiometer. Publications by the author are included in the beginning.

CHAPTER 2

2 Science and Theory

2.1 Epoch of Reionisation

Observations of CMB fluctuations and high redshift galaxies using high precision and sensitive instruments such as the Hubble Space Telescope and the Wilkinson Microwave Anisotropy Probe (WMAP) confirmed the theoretical models that the galaxy formation was a gradual process in the standard Big Bang cosmology (Schneider, 2004). One of the current main challenges in cosmology is then to identify the details of these density distributions and how they evolved into cosmic structures as are observed now. The Epoch of Reionisation is a crucial period in the early Universe when baryonic matter, mainly in the form of neutral gas, started to reionise as the first generation of stars began to collapse and formed (Schneider, 2004; Zaroubi, 2012). Prior to this, the evolution of structure formation is expected to have been dominated mostly by dark matter, while the remaining baryonic matter played perhaps a marginal role. In this scenario, the EoR is associated with the onset of these early stages of star formation and the appearance of the first quasars and proto-galaxies (Barkana & Loeb, 2001; Fan, Carilli, & Keating, 2006).

As these early luminous objects came to life, perhaps at redshift z >30 (S. Furlanetto et al., 2006) and filled the Universe with ultraviolet photons capable of ionising hydrogen gas, huge pockets of ionised gas were formed in the surrounding intergalactic medium (IGM) in subsequent times. During this transition phase, as the number of luminous objects and supermassive structures increased and evolved, the neutral gas concentration mainly in the form of neutral hydrogen (HI) clouds decreased. Eventually after a sufficient amount of time, the ionised fraction of the gas increased until the whole Universe filled with the overlapping ionised regions (HII) by the time it was less than a billion years old, z ~6 (Barkana & Loeb, 2001; Fan, Carilli, et al., 2006; Loeb & Pritchard, 2012).

The behaviour of HI, such as its distribution, brightness temperature, density and abundance, is of primary importance during this epoch. It is an important ingredient in the study of the structure formation, the emergence of the first luminous objects and the dynamics of galaxy evolution in the early Universe. From an observational point of view, the reionisation phase transition, from HI to HII is currently one of the most important unknowns in cosmology (Pritchard & Loeb, 2010).

Figure 2-1 shows a schematic of cosmic history as the Universe expanded and cooled after the Big Bang. Initially after inflation, the Universe was filled with a mix of high energy photons, baryons and Dark Matter in the form of hot plasma. The Universe was opaque to light and radiation. At Recombination, around redshift z~ 1100 (400,000 years after the Big Bang) the primordial plasma in the Universe cooled sufficiently until it became favourable for protons and electrons to combine into neutral atoms. At this point, the photons began to travel freely through space. The Universe became transparent to photons instead of being opaque. Cosmological models suggest that in the next few hundred million years as gravity took over and compressed the gas into denser regions following the Dark Matter distribution, the first stars evolved (Yoshida, 2003) and ended the cosmic Dark Ages. This was followed by a period characterised by the appearance of first luminous objects known as Cosmic Dawn (Schneider, 2004). The Cosmic Dawn is the onset of Epoch of Reionisation, during which the primordial gas was reionised within approximately a billion years of the Big Bang.

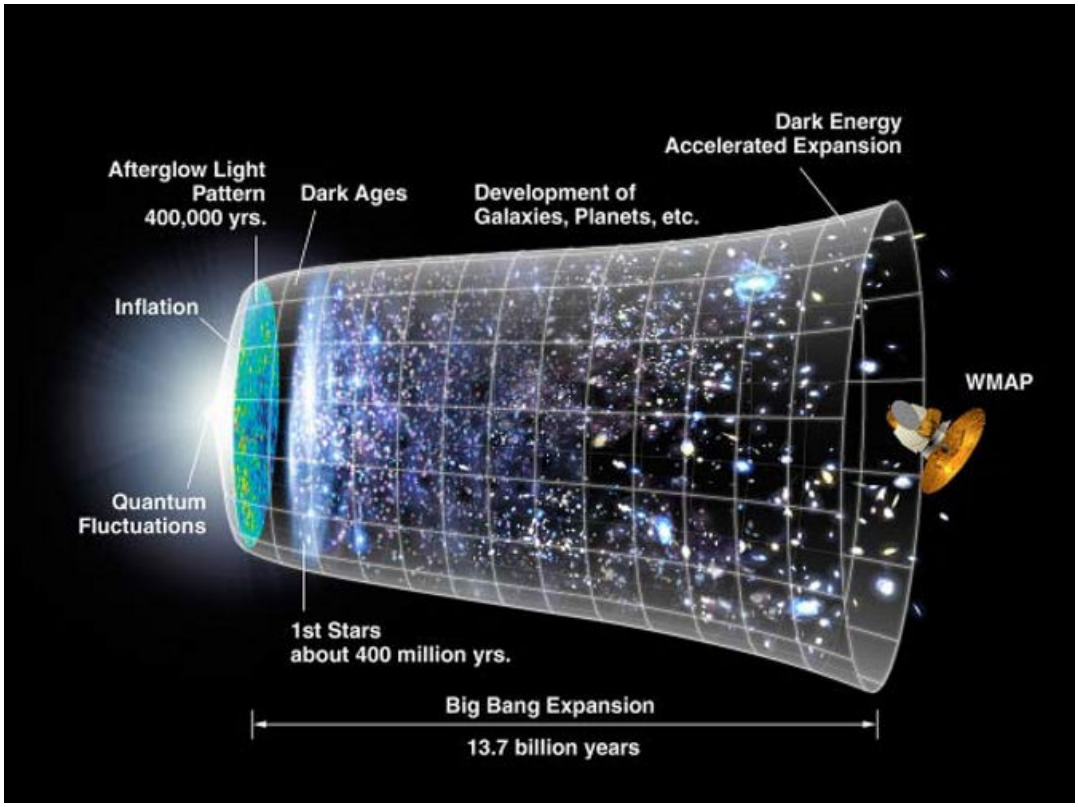

Figure 2-1 Cosmic history (NASA WMAP Science Team, 2010a)

Not much is known about the Dark Ages, Cosmic Dawn and the Epoch of Reionisation. Some key questions are (S. R. Furlanetto et al., 2009):

1) When did reionisation occur and what type of photon sources were responsible for reionisation?
2) When did the first stars and galaxies form and what were their characteristics?
3) How did the first stars and galaxies evolve and affect the Universe around them?
4) How were the reionising sources distributed relative to the gas in the IGM?
5) What were the size, geometry, and topology of the ionised zones, and how did these properties evolve?
6) What fraction of the primordial hydrogen remained neutral as a function of time?

2.2 Probes of the Intergalactic Medium after Reionisation

Over the last decade, several astrophysical observations have helped constrain the redshift range where one might search for answers to the above questions. Three independent probes of the IGM out to the redshift of the EoR are briefly introduced, each of which suggests star formation activity may extend well into the redshift range $6 < z < 25$, followed by a more detailed discussion of the 21 cm HI line as a direct probe of reionisation.

2.2.1 Lyman Alpha Forest Absorption

The condition of the IGM may be studied through the analysis of the Lyman-α forest (Zaroubi, 2012). This is the combination of the absorption lines arising from the first transition in the Lyman series of neutral hydrogen. The Lyman-α transition can be observed in absorption when neutral hydrogen in the ground state (n=1) absorbs a photon and moves to the first excited state (n=2).

This absorption feature is observed in the spectra of background quasi-stellar objects (QSOs) due to intervening intergalactic gas clouds at lower redshifts. The QSOs are strong sources of optical, ultraviolet and X-ray continuum emission against which intervening gas clouds can leave their imprints as absorption lines at a range of wavelengths in the spectrum. When observed at high redshifts, QSO spectra contain an abundance of absorption lines concentrated blue-wards (i.e. at shorter wavelength) of the Lyman-α emission line of the quasar itself, creating the Lyman-α forest.

Figure 2-2 shows a comparison of the Lyman-α forest of two QSOs spectra, the nearby 3C273 (z=0.158) and the distant Q1422+2309 (z=3.62) (Pradhan & Nahar, 2011). The observed spectra have been corrected to rest-frame wavelength for direct comparison. The broad and distinct emission line at the right of figure is the Lyman-α emission (1216Å)

from the quasar itself. The intervening clouds that produce the absorption lines in the red-shifted Q1422 are very dense resulting in a Lyman-α forest.

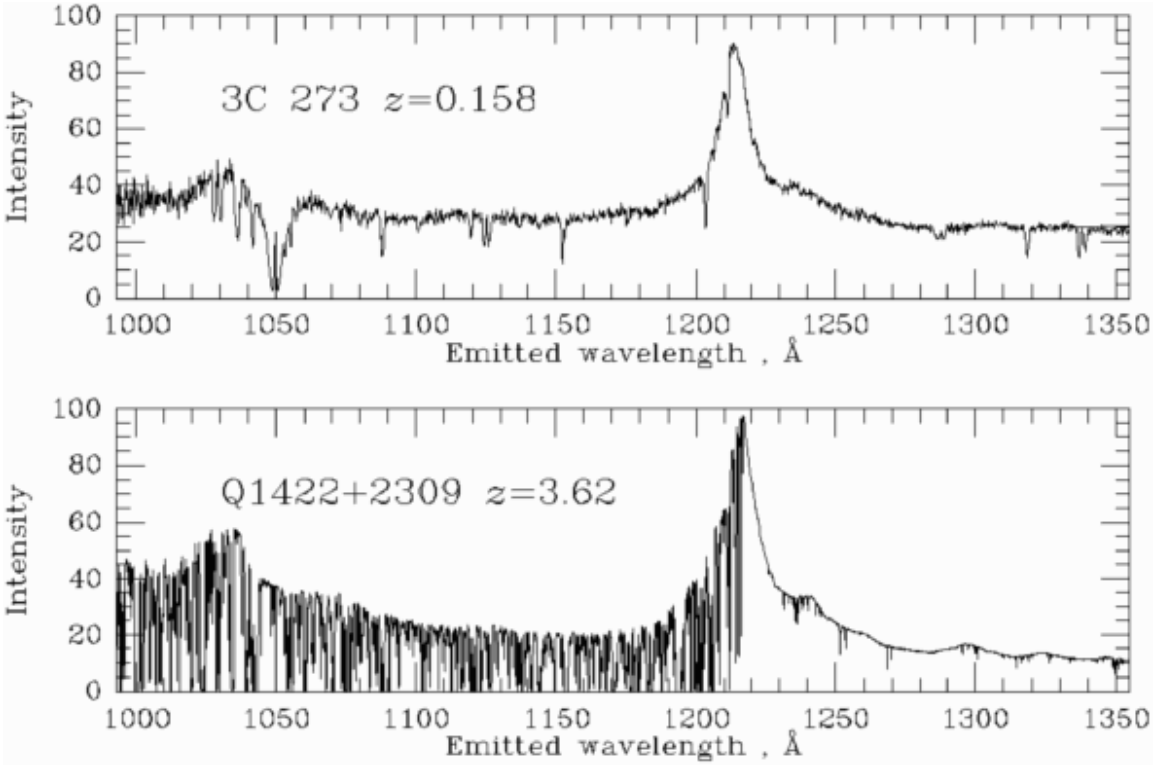

Figure 2-2 Spectra of a low and high red-shifted quasars showing the Lyman-α forest, most pronounced in Q1422+2309 (Keel, 2002).

The Lyman-α forest is an important probe of the moderate redshift, 2<z<4, Universe and reflects the neutral hydrogen (HI) distribution on small scales in the IGM (Jena et al., 2005). The Lyman-α forest absorption spectra toward high redshift galaxies show that the opacity of the IGM to photons at Lyman-α energy is rapidly increasing at z > 6 (Fan, Carilli, et al., 2006). This is an indicator that the primordial hydrogen gas has undergone a phase transition from a neutral to an ionised condition around z ~ 6.

2.2.2 Observation of Gunn Peterson Trough

Becker et al. (2001) observed that the Lyman-α absorption in the spectra of high redshift quasars in the range z = 5.8 to 6.28, declines rapidly with redshift. At around a redshift of z~6 the absorption forest, immediately blueward of the Lyman-α emission line, turns into an absorption trough, known as the Gunn-Peterson (GP) trough, an effect first pointed out by Gunn and Peterson (1965).

Furthermore, the study of a sample of 19 moderate resolution spectra of QSOs in the range z=5.74 to 6.42 by Fan, Strauss, et al. (2006) using the Sloan Digital Sky Survey imaging

data also provides evidence of this accelerated evolution in the ionisation state of the IGM at z > 5.7.

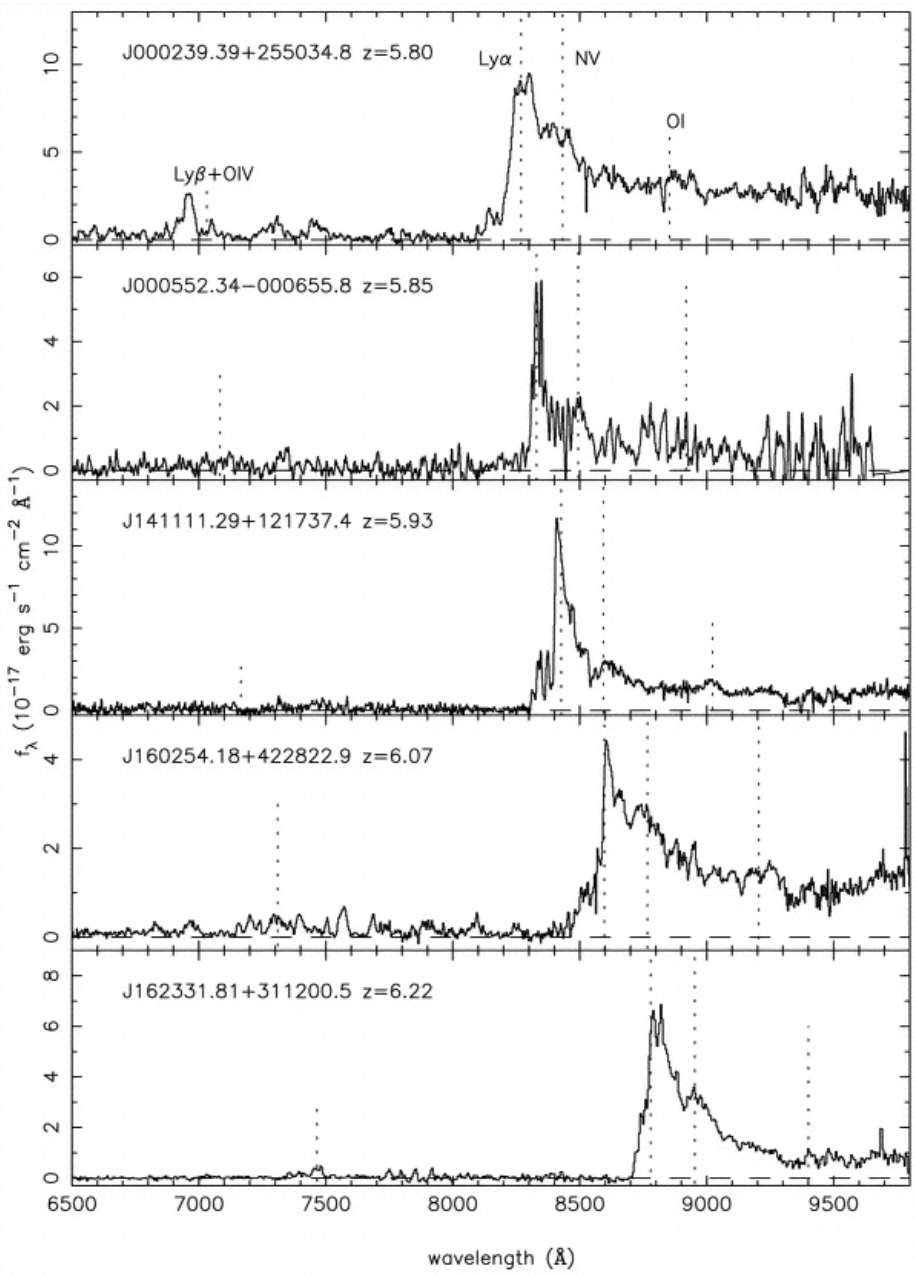

Figure 2-3 Optical spectra of z ≳ 5.8 quasars observed with Keck/ESI (Becker et al., 2001)

The detection of GP trough and GP optical depth >>1 indicates a rapid change in the neutral fraction of the gas in the IGM at redshift z > 6. In other words, the neutral fraction of the gas in the IGM decreases rapidly from $x_{HI} > 10^{-3}$ at z > 6 to $x_{HI} < 10^{-4}$ at z ~ 5.5 (Fan, Carilli, et al., 2006). However, even a small HI fraction in the IGM could account for an undetectable flux of the Lyman-α photons at the intervening redshifts in the Lyman-α forest region, which may also be a local effect (McGreer, Mesinger, & Fan, 2011). Consequently, the existence of the GP trough on its own is not an indicator of the end of

the EoR, but the fast evolution of the mean absorption in these high red-shifted quasars suggests that the mean ionising background along the line of sight to these QSOs has declined significantly from z ~ 5 to 6 as indicated by Becker et al. (2001) and Fan, Strauss, et al. (2006).

Because complete GP absorption can be seen with x_{HI}, as low as 10^{-3}, the presence of the GP trough by itself cannot provide stringent constraints on x_{HI} over cosmic history, so alternate methods of determining x_{HI} are required (McGreer et al., 2011).

2.2.3 CMB Polarisation and Temperature Anisotropy

The Cosmic Microwave Background, as the oldest observable radiation source, also provides crucial information relevant to the history of reionisation (Gawiser & Silk, 2000). The CMB temperature is extremely uniform all over the sky. Nonetheless, minute temperature variations exist at part per million levels that correspond to regions of slightly different densities at very early times, representing the seeds for the structure of the Universe today. NASA's COsmic Background Explorer (COBE) satellite and subsequently Wilkinson Microwave Anisotropy Probe (WMAP), launched 2001, and ESA's Planck, launched 2009, measured these tiny fluctuations (Ade et al., 2013; Bennett et al., 1996; Komatsu et al., 2011).

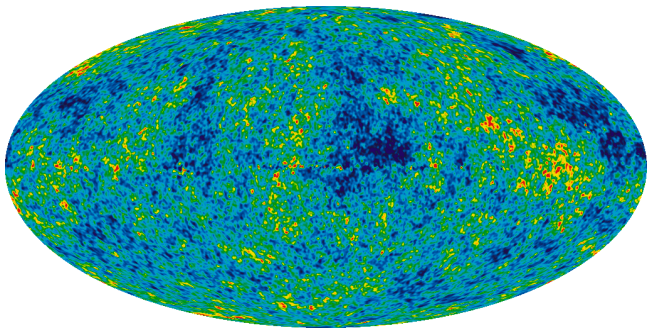

Figure 2-4 The Temperature fluctuations in the CMB (NASA WMAP Science Team, 2010b)

Reionisation places its characteristic marks on the CMB through the interaction between the CMB photons and free electrons. During the onset of EoR, as free electrons are released from neutral atoms due to ionising UV radiation, they scatter CMB photons, known as Thomson scattering, resulting in the CMB polarisation (Haiman, Knox, & Tegmark, 1999). This leaves imprints on the CMB polarisation and temperature anisotropies in the form of minute temperature fluctuations from point to point across the whole sky. These effects have been observed by WMAP and Planck measurements providing evidence of reionisation in the CMB anisotropy results (Komatsu et al., 2011).

The large scale polarisation of the cosmic microwave background implies a significant ionisation fraction extending to high redshifts z~11 ±3 assuming instantaneous reionisation. Combining with the GP trough observations of high red-shifted quasars, the results suggest that reionisation could begin as early as z ~14, and with the overlap phase ending at z ~ 6 (Fan, Carilli, et al., 2006). However, in the intervening period there are a number of questions un-answered as indicated in section 2.1. One way to obtain answers is to improve on these techniques and the other is to use observational techniques using the 21 cm neutral hydrogen line, which is expected to be a promising probe of the early Universe, opening perhaps new insights into the early phases of cosmic structure formation. This is the subject of the next section.

2.2.4 The 21 cm Hydrogen Hyperfine Structure Line

Neutral hydrogen (HI) consists of a single proton bound to a single electron. Both the proton and the electron also possess "spin" (Seeds & Backman, 2010). They can spin in the same direction (parallel) or in opposite directions (anti-parallel). The energy carried by the hydrogen atom in the parallel spin state is slightly higher than the energy it has in the anti-parallel spin state. In the ground state atomic hydrogen can be in one of these two closely spaced energy levels.. The transition between these energy levels has a ΔE of $5.9 \times 10^{-6} eV$ and is called the "hyperfine transition of hydrogen" (Kraus, 1986).

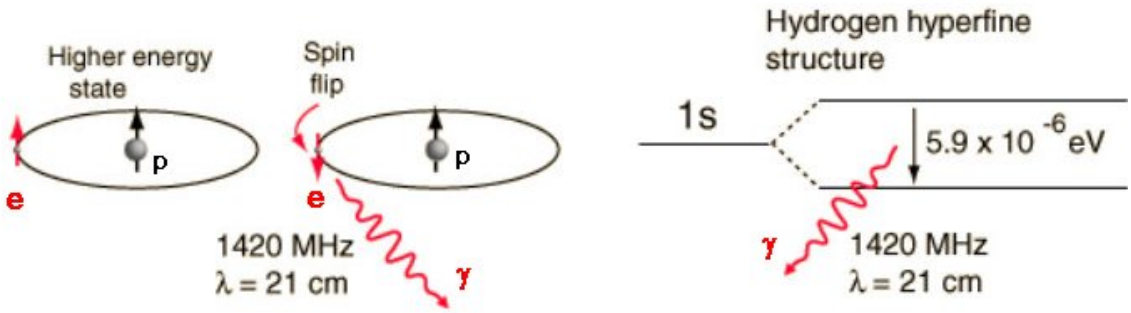

Figure 2-5 The spin flip transition of neutral hydrogen atoms emitting a 21 cm photon

A photon is emitted when the hydrogen spin "flips" state from the parallel to the anti-parallel configuration (see Figure 2-5). This magnetic dipole transition is extremely rare, with a transition probability of $A_{10} \sim 2.85x10^{-15}s^{-1}$ (or mean lifetime of 11 Myr). Hendrick van de Hulst had predicted in 1944 that owing to the abundance of neutral hydrogen in the interstellar medium (ISM), emission could be observed at 21.1cm wavelength (or 1420.2 MHz). The hyperfine transition was first detected in emission in

1951 by Ewen and Purcell (Ewen, 1951) at Harvard and is referred to here as the "21 cm HI line" or "21 cm signal" for short.

The 21 cm HI line produced by neutral hydrogen in the ISM provides a useful probe for studying the dynamics of galactic rotation (Burke & Graham-Smith, 1997; Giovanelli & Haynes, 1988). By mapping the distribution of neutral hydrogen in the Milky Way, using observations of the 21 cm spectral line, the complex picture of its spiral structure was first deduced by Kerr and Westerhout in 1964 (Kerr, 1969).

2.2.5 The Red-shifted 21 cm HI Line

Of particular interest in this thesis is the red-shifted 21 cm HI line during the EoR, when large HII regions are expected to have generated substantial fluctuations in the 21 cm background as a function of direction on the sky and redshift (S. Furlanetto et al., 2006).

The 21 cm HI line during the EoR is red-shifted by the expansion of the Universe to wavelengths in the VHF radio band and should appear as a faint and diffuse signal at radio frequencies below 200 MHz for redshifts above 6 according to $f_{obs} = \frac{f_{21cm}}{(1+z)}$ (Gnedin & Shaver, 2004; P.A. Shaver et al., 1999).

In this way, the redshifting of the photons of light allows one to examine the history of the Universe as a function of time, as each frequency corresponds to a different redshift of the Universe and, as a result, obtain a three-dimensional map of the diffuse 21 cm HI distribution in it. It can also enable us to measure the properties of the first stars and black holes inside galaxies that are much too small to be directly imaged (Burns et al., 2012).

2.2.6 The 21 cm Brightness Temperature

The 21 cm signal from the neutral IGM during and prior to reionisation may be predicted analytically (G. Santos et al., 2008) or numerically through simulations (Ciardi & Madau, 2003). The sky averaged 21 cm brightness temperature, T_b , of an IGM gas, at an observed frequency υ corresponding to a redshift of $1 + z = \upsilon_0/\upsilon$, relative to the CMB can be shown to be as follows (Zaldarriaga, Furlanetto, & Hernquist, 2004):

$$T_b\,(\mathrm{z}) \approx\ 23\, X_{HI}(1+\delta_b)\left(\frac{1+z}{10}\right)^{0.5}\left(1-\frac{T_{CMB}}{T_s}\right)\left(\frac{\Omega_b h^2}{0.02}\right)\left(\frac{\Omega_m h^2}{0.15}\right)^{-0.5}[mK], \qquad \textbf{Eq 2-1}$$

where $\delta_b, T_s, X_{HI}\ and\ T_{CMB}$ are redshift dependent. $X_{HI}$is the neutral fraction of hydrogen, δ_b is the fractional IGM over-density of HI, T_{CMB} is the temperature of the CMB at redshift

z, T_s is the spin temperature describing the relative population of the ground and excited states of the hyperfine transition of neutral hydrogen and where Ω_b, Ω_m, h are the parameters of ΛCDM cosmology. The fifth and sixth terms, $\left(\frac{\Omega_b h^2}{0.02}\right)\left(\frac{\Omega_m h^2}{0.15}\right)^{-0.5}$, are approximately 1.

Eq 2-1shows that the 21 cm brightness temperature at different stages of the evolution is dominated by different contributions. It indicates that the observability and hence strength of the 21 cm hydrogen spectral line depends on the spin temperature and the mechanisms evolving with redshift, that drives it below and above the CMB temperature. For $T_s \sim T_{CMB}$ there would be no observable 21 cm signal. For $T_s \ll T_{CMB}$ there would be a strong absorption signal relative to the CMB and for $T_s \gg T_{CMB}$ the brightness temperature saturates, passes from absorption to emission and becomes independent of the spin temperature.

Figure 2-6 shows a theoretical representation of the expected evolution of the sky-averaged 21 cm brightness temperature relative to the CMB temperature, from the redshift of z~200 to the time it approaches complete reionisation around redshift z~6 (Pritchard & Loeb, 2010).

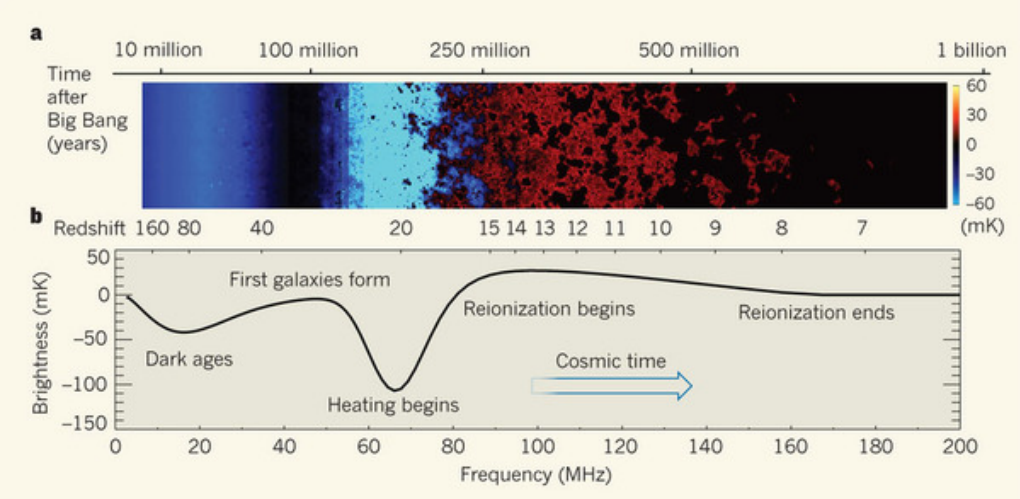

Figure 2-6 Brightness temperature (Loeb & Pritchard, 2012)

The ordinate (y axis) on the lower panel shows the red-shifted 21 cm brightness temperature and the abscissa (x axis) shows the redshift and on top the red-shifted frequencies. The figure also shows a series of simulated images of the 21 cm fluctuations during the Dark Ages when there was only neutral gas, and as the first stars born causing ionised bubbles to appear, grow, and merge until they fill up the Universe, when it reaches a billion years of age.

There are still substantial uncertainties in the exact evolution of the 21 cm signal, arising from the properties of the early structures in the Universe, making the potential implications of measuring the 21 cm signal very exciting.

2.3 The 21 cm Global Signal History

As shown in Figure 2-7, the 21 cm HI line should produce a signal over the redshift range of approximately 6 < z <200. Around redshift z~200 is the period before the birth of first stars and galaxies, when the hydrogen gas was only influenced by gas collisions and absorption of CMB photons at high redshifts. Redshift z~6 corresponds to the period when the neutral gas was destroyed and the Universe is expected to be fully ionised (Pritchard & Loeb, 2008).

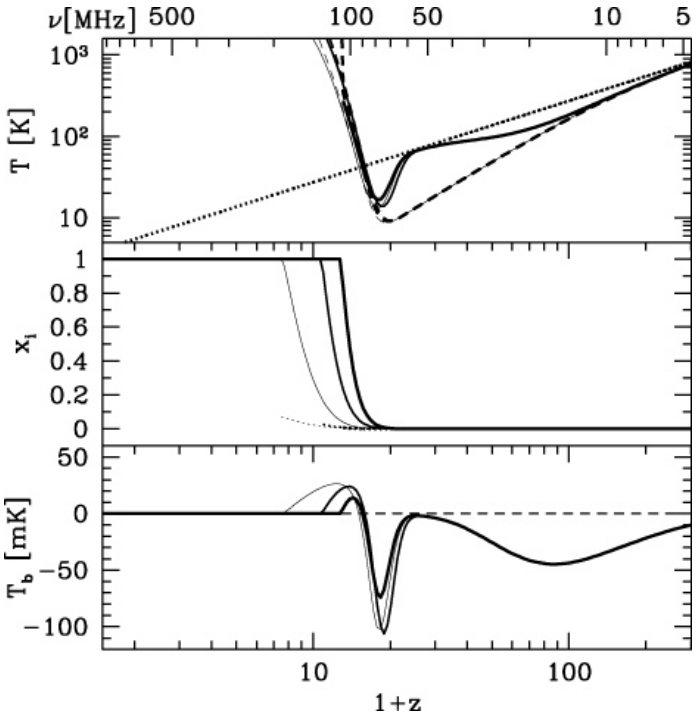

Figure 2-7 The expected variation of the CMB temperature T_{CMB}(dotted), the gas kinetic temperature T_K (dotted), the spin temperature T_S (solid) on the top panel, the expected variation of the gas fraction on the middle panel, and the expected variation of the brightness temperature, T_B , of neutral hydrogen with redshift during the EoR for 3 different models (Pritchard & Loeb, 2008)

The evolution of the 21 cm global signal as modelled by Pritchard and Loeb (2010) consists of several distinct phases evolving with redshift, though the exact timing and details of the signal history are uncertain and depend on astrophysical details about the early Universe. These peaks and troughs designate key physical events which are due to the interplay between the first luminous sources and the physics of the neutral hydrogen

gas at the onset and during EoR. Moreover, the relative timing of these phase transitions can set the observability of the 21 cm signal.

These phases are depicted schematically in Figure 2-8, beginning at redshift z~200 before the Cosmic Dark Ages, going on to the start of Cosmic Dawn at redshift $z = z_*$, to the ionisation phase at redshift $z = z_R$~6. Based on the observability of the 21 cm brightness temperature, T_b , the key features can be described following Fan, Carilli, et al. (2006) , (Pritchard & Loeb, 2008) and Loeb and Pritchard (2012):

1) $T_b < 0$: Before the first stars, at redshift 30 < z < 200, as the gas in the IGM cools adiabatically with temperature due to expansion of the Universe, the gas kinetic temperature, T_K , is falling as $(1+z)^2$ while the CMB temperature, T_{CMB} falls as $(1+z)$ resulting in $T_s \sim T_K < T_{CMB}$ (Loeb & Zaldarriaga, 2004). As a result, the 21 cm HI signal may be observed in absorption against the CMB temperature. This period is shown schematically in Figure 2-8.

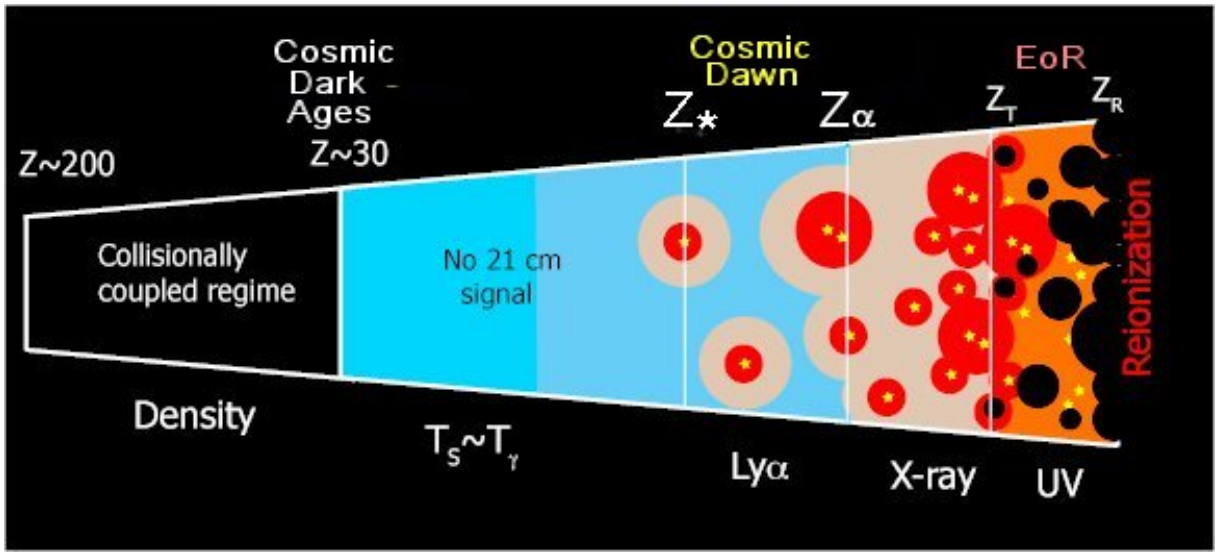

Figure 2-8 Schematics of the different phases of the 21 cm signal (Loeb & Pritchard, 2012)

2) $T_b \sim 0$: At redshift $z_{\star} < z < 30$, during the Dark Ages and before the first stars switch on at redshift $z_{\star}$, as the Universe expands and further cools, the gas density decreases reducing the collision rate. Collisions can no longer couple T_s *to* T_K and absorption of CMB photons drives the spin temperature, T_s , into equilibrium with T_{CMB} and the 21 cm signal fades away against the CMB temperature. This period is shown schematically in blue in Figure 2-8.
3) $T_b < 0$: At redshift $z_\alpha < z < z_{\star}$, when the early luminous objects formed and before saturation of Lyman-α coupling at redshift z_α , they emit Lyman-α photons

causing the local coupling of T_K to T_s, leading to a 21 cm absorption trough. The transition phase trough, in this case, is determined by the intensity of Lyman-α emissions due to luminous sources, so this period is much more uncertain but the relative brightness temperature is expected to be deep, approximately <100 mK.

4) $T_b > 0$: At redshift $z_T < z < z_\alpha$, as heating continues and before the 21 cm signal is saturated against the CMB temperature at redshift z_T , accreting black holes are likely to form and begin to radiate X-rays. The energetic X-ray photons then begin to heat the gas in the IGM. The X-ray heating will subsequently transform the 21 cm signal from absorption to emission above the CMB temperature, $T_s \gg T_{CMB}$ at z_T and the filling fraction of HII significantly increases.
5) $T_b > 0$: At redshift $z < z_R$, reionisation is complete and any 21 cm signal originates primarily from collapsed islands of neutral hydrogen.

2.4 The 21 cm EoR Experiments

There are two observational methods of using the red-shifted 21 cm signal to trace the cosmic history of the EoR. One approach is to characterise the local fluctuations in the background and the other is to constrain the global evolution of the sky-averaged 21 cm brightness temperature with redshift.

Directly measuring the 21 cm fluctuations and mapping of the power spectrum of neutral hydrogen during the EoR will require large radio arrays (Pritchard & Loeb, 2008) such as the first generation projects in operation the MWA, the LOFAR, the Precision Array for Probing the Epoch of Reionisation (PAPER) (Parsons et al., 2009) and the Giant Metrewave Radio Telescope (GMRT) (Paciga et al., 2011) and, in the future, the Square Kilometre Array (SKA) (M. G. Santos, Silva, Pritchard, Cen, & Cooray, 2011).

The other, complementary, technique is to measure the global time evolution of the red-shifted 21 cm signal as an independent probe of the reionisation history which should be visible over the entire sky. The expected magnitude of these phase transitions should still be well above the detection limits of a sensitive receiver and its sharpness could make it distinguishable from Galactic and other foreground noise sources (P.A. Shaver et al., 1999). This red-shifted 21 cm global signal can ideally be detected by making precise measurements in the radio frequency band below 240 MHz using an exquisitely well-calibrated antenna, tuned and matched to a low noise receiver with just a few hours or days of observation time, depending on the receiver resolution bandwidth, at an exceptionally radio quiet site (P. A. Shaver & de Bruyn, 2000).

2.5 Foregrounds to the EoR Signal

The extraction and identification of the red-shifted 21 cm global signature from observational data is one of the most challenging tasks in probing reionisation history. This is largely due to the fact that the received signal is a combination of a number of components which includes the 21 cm global signal, Galactic and extragalactic foregrounds, ionospheric distortion and instrumental response, each having its own origin and statistical properties (spatially and in frequency).

The foreground emission from the Milky Way galaxy and extragalactic sources dominate the sky. The recovered power from these sources is more than 5 orders of magnitude larger (refer to Figure 2-9) than the expected cosmological 21 cm global signal, but is expected to have a very smooth power law behaviour as a function of frequency (P.A. Shaver et al., 1999). However, resolving the red-shifted 21 cm contribution, which is thought to be tens of mK, from the all-sky spectrum requires identifying minute deviations in the power law behaviour of the foreground spectra to better than a few parts per million (ppm).

The Galactic synchrotron emission is the dominant component of the foreground, accounting for approximately 70% of the foreground at 150 MHz (Jelic, 2010; P.A. Shaver et al., 1999). Its spectrum can be estimated as a power law in temperature given by (Gleser, Nusser, & Benson, 2008):

$$T_{gal}(f) = T_{150}\left(\frac{f}{150MHz}\right)^{-\beta} + T_{CMB}(f) \qquad [K], \qquad \textbf{Eq 2-2}$$

where amplitude $T_{150}{\sim}290K$, and β , the spectral index, is 2.5 in the range 50-200 MHz and has generally small variations of 0.1 depending on the Galactic latitude (Bowman, Rogers, & Hewitt, 2008).

However, the averaged red-shifted 21 cm signal fluctuates, increasing with decreasing frequency to a maximum contribution of the order $T_b > 25mK$ during early EoR (100-200 MHz), and another transition (50-80 MHz) diping into an absorption trough of the order T_b <100 mK, referring to Figure 2-7.

Figure 2-9 shows graphically the expected sky-averaged 21 cm signal against the flat CMB temperature and the Galactic temperature curve based on Eq 2-2. This indicates a ratio of $\frac{T_b}{T_g} = \frac{10mK}{5030K} > 0.2x10^{-5}$ at 50 MHz and $\frac{T_b}{T_g} = \frac{10mK}{290K} > 0.3x10^{-4}$ at 150 MHz.

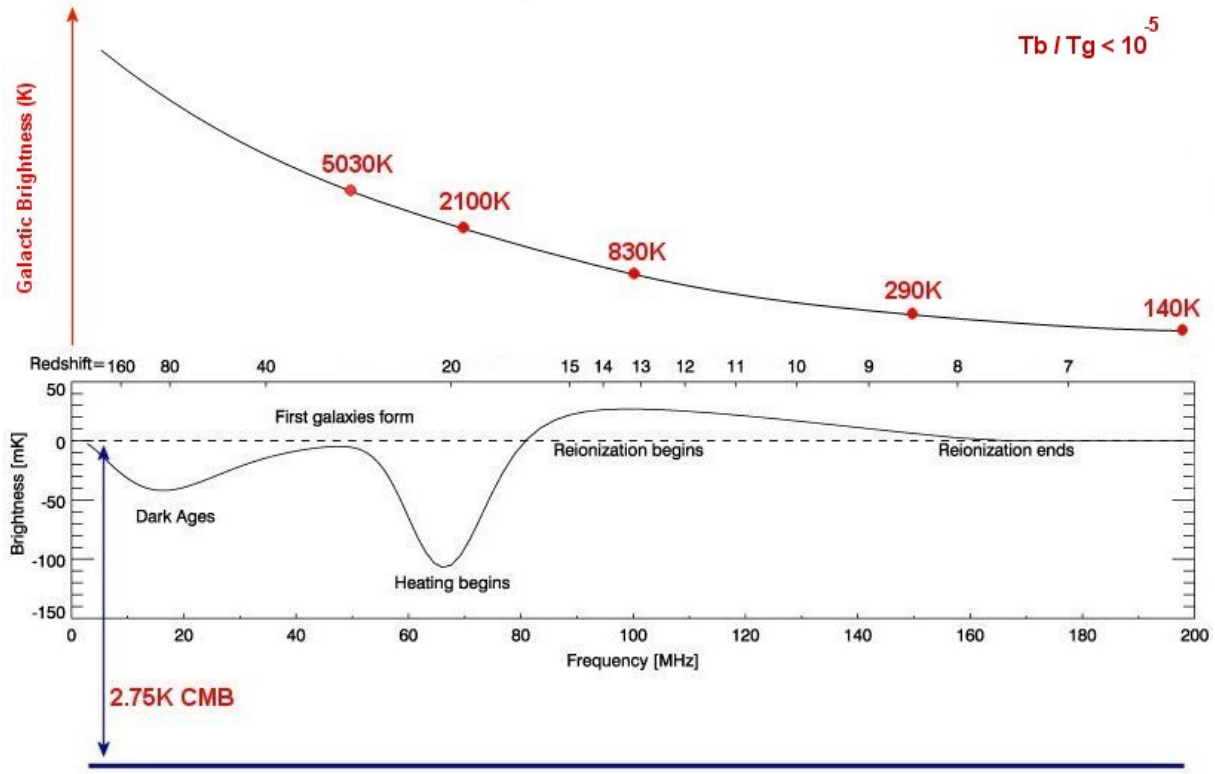

Figure 2-9 Comparison of the expected 21 cm signal vs Galactic foregrounds and CMB (Briggs, 2012; Loeb & Pritchard, 2012)

2.6 The Global EoR Experiments

Various astronomy groups around the world have attempted to design and develop sensitive hardware using single antennas to measure and constrain this faint global EoR signal. Of note are the EDGES and CORE experiments which will be discussed in this section.

2.6.1 EDGES Experiment

The Experiment to Detect the Global EoR Signature (EDGES) is an experiment developed by Judd D. Bowman at Arizona State University and Allan E. E. Roger at Massachusetts Institute of Technology in the USA, to make accurate measurements of the sky noise from 100 MHz to 200 MHz, which corresponds to the redshift range $13 > z > 6$. It uses a 3 position Dicke switch radiometer to derive a calibration spectrum from the sampled data captured from an antenna, a load and a calibrated noise source. The complete hardware system was based on off-the-shelf components, consisting of a low noise amplifier and switching front-end module connected directly to a single compact "Four-point" antenna (SeongYoup, 2004) and an off-the-shelf fast data acquisition back-end module. Based on the observation, an initial upper limit of 450 mK has been placed on the relative brightness

temperature of the red-shifted 21 cm signal during the EoR at z=8 (Bowman et al., 2008). Consequently, a lower limit of $\Delta z > 0.06$ has been placed on the duration of reionisation transition (Bowman & Rogers, 2010). The experiment is at its second phase, EDGES II, to improve the system calibration further and make accurate absolute calibrated measurements (Rogers & Bowman, 2012) . EDGES and EDGES II have been deployed at the Murchison Radio astronomy Observatory (MRO) in WA.

2.6.2 CORE Experiment

The Cosmological Reionization Experiment (Core Mk I) is another experiment that developed a radio telescope to measure the 21 cm signal in the frequency range 114 MHz to 228 MHz, which corresponds to the redshift range $11.5 > z > 5.2$. The approach was to combine a frequency independent antenna with a digital correlation spectrometer to form a correlation radiometer. The system was calibrated against injected noise and against a modelled galactic foreground.

Components were specified for calibration of the sky spectrum to 1 mK/MHz relative accuracy. Comparing simulated and measured spectra showed that band-pass calibration is limited to 11 K, due to a larger than expected frequency dependence of the antenna pattern. Overall calibration, including additive contributions from the system and the radio foreground, was limited to 60 K. Future refinements to reduce systematics are still required (Chippendale, 2009).

2.6.3 BIGHORNS Experiment

The BIGHORNS experiment is now being developed at ICRAR in the hope of providing further cosmological constraints on the early Universe. This thesis provides a detailed design of a multi-configurable RF radiometric receiver operating in the frequency range 50 to 250 MHz, corresponding to the redshift range $5 < z < 27$. This sensitive receiver may be deployed in the BIGHORNS experiment combined with a single frequency independent antenna and a data acquisition system to measure the sky spectrum.

2.6.3.1 BIGHORNS Receiver Hardware Requirements

As discussed in section 2.4, the complementary approach to observing the red-shifted 21 cm signal is to measure the evolution of the sky averaged global brightness temperature with redshift. Due to unique features of this red-shifted 21 cm global signal below 200 MHz as shown in Figure 2-9, a sensitive radiometric receiver tuned for this range can be exploited to separate the possible EoR features from supposed smoother foreground

contributions. Also, as the 21 cm global signal is expected to be visible in all directions on the sky, a wideband antenna tuned to the frequency range below 200 MHz could be utilised without loss of sensitivity. In addition, due to the sharp transition in the sky average 21 cm global signal against the smoother Galactic foregrounds, resolution below 10 mK is required. A digital acquisition system to capture power spectra to average and resolve data fluctuations would also be required. The measurements would need to be carried out at a radio quiet site and so portability of the receiver and the overall EoR system would be an advantage.

Based on the above theoretical knowledge of the 21 cm global signal, a preliminary specification for the receiver would be:

- Able to operate in the frequency range of 50- 200 MHz ($5 < z < 27$);
- Able to provide radiometric resolution better than 10 mK;
- Compact, weather-proof, portable battery operated;
- Temperature monitoring and control of the receiver may be required.

The following chapters describe the detailed design, development and implementation of such a receiver.

CHAPTER 3

3 Radiometric Receiver Design

The observation of the 21 cm global signal is very challenging, due to its extremely low signal strength, expected to be 10s of mK, against intense foreground contaminants of 1000s of K and higher below 200 MHz. Any distortion, mismatch or unwanted additive noise components in the receiver system may destroy the possibility of EoR detection. This demanding task requires a highly accurate and stable receiver. The steps towards accuracy include a methodical calibration process. The stability may be achieved by careful design and analysis of the individual components of the receiver. The aim here is to develop and design a modularised compact and portable low noise radiometer receiver in order to be integrated into reionisation experiments.

3.1 Introduction

This chapter begins with a general description of radiometers, specifically for radio astronomy applications, their purpose and main parameters, namely resolution and accuracy. This is followed by the description and comparison of the different types of radiometer related to this project. Finally, an analysis of the specific radiometer designed for the requirements of the EoR experiment is described. This is a hybrid type radiometer that may be configured remotely to operate in different modes, providing improved resolution, stability and flexibility during field tests.

3.2 Radiometric Receivers in general

A radiometric receiver is a highly sensitive and calibrated receiver, which can measure thermal electromagnetic radiation from material media (Ulaby, Fung, & Moore, 1981). In general, a radiometer has two parts, an antenna and a receiver. The main objective of a radiometer is to measure the averaged power of the input noise (from a radio telescope for instance) to a high degree of accuracy and resolution. The measurement accuracy is achieved through the use of calibration. The resolution is the smallest change in temperature the radiometer can measure and is achieved based on the radiometer type chosen.

In radio astronomy applications, noise power (dBm/Hz) at the input of an antenna may be expressed in terms of an equivalent noise temperature in Kelvin (K). This could be the temperature of a blackbody that radiates the power that is the "brightness temperature", T_B.

Consider an idealised radiometric receiver with the antenna pointed towards an astronomical object of brightness temperature, T_B, in the sky, as shown in Figure 3-1. The power radiated by the object, when intercepted by an antenna, generates a voltage at the antenna terminals. The antenna temperature, T_A, is now related to the brightness temperature of the object. Assuming the entire antenna pattern sees a uniformly radiated object and the antenna itself is lossless, then $T_B = T_A$.

To measure this antenna temperature (or namely the brightness temperature of the object), with the necessary resolution and accuracy a sensitive radiometer is required. The radiometer amplifies (G) this signal, integrates it over a certain bandwidth, B, and presents voltage fluctuations to a detector as:

$$P = \kappa GBT_A \,, \qquad \textbf{Eq 3-1}$$

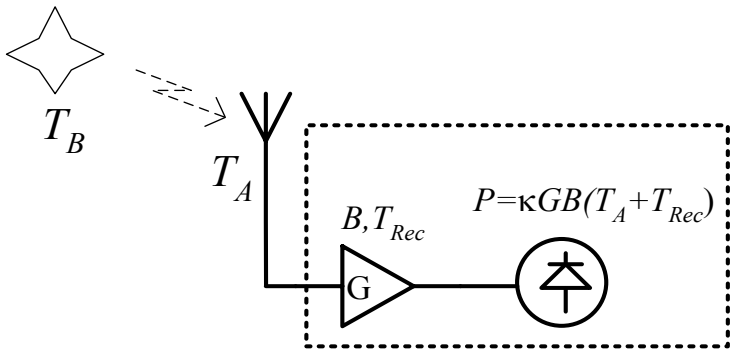

Figure 3-1 An idealised radiometric receiver

where κ is the Boltzmann constant with a value of 1.3806×10^{-23} J/K (or -198 dBm/Hz/K).

In practice, the power measured at the detector output is the sum of the power from the antenna and the receiver temperatures and Eq 2-1 can be re-written more appropriately as:

$$P = \kappa GB(T_A + T_{Rec}) \,. \qquad \textbf{Eq 3-2}$$

If the terms B, G, T_{Rec} above are constants, there are no stability problems. Additionally, if they are known constants there are no accuracy problems. By measuring the power P, the antenna temperature, T_A, can be calculated correctly from the known parameters above.

However, the various components in a receiver, such as amplifiers, filters, couplers and power detectors including the antenna do not have constant and stable frequency responses. These underlying fluctuations in the radiometer response arising from the stochastic nature of the signal and instabilities within the receiver are unavoidable and may occur due to supply voltage variations and to ambient temperature fluctuations over short or long periods, for example. In addition, the receiver components introduce their own noise power terms into the receiver system due to their intrinsic noise. As a result, the power measured at the detector output would be the sum of the power from the received signal and all the various gain stages, plus some uncertainties arising due to using imperfect calibrated data and components.

In the case of the 21 cm global signal experiment, the ratio of the expected signal to noise power is expected to be extremely low. To detect an EoR signature of 100 mK at around 70 MHz, for an antenna temperature, T_A of 2000 K and T_{Rec} of 150 K, the absolute accuracy of 10 mK corresponds to stability to within 1 part per 200,000.

3.3 Radiometer Resolution and Measurement Uncertainty

There are different types of radiometer configurations depending on the application of interest, such as a total power radiometer, a Dicke radiometer, a correlation radiometer and others (Ulaby et al., 1981). Ideally, radiometers may be assessed based on their "minimum detectable sensitivity" or "resolution". The radiometric resolution is the minimum change in the input level that can be resolved at the radiometer output (Ulaby et al., 1981). However, when evaluating the performance and limitations of actual radiometers it is more meaningful to use the term "measurement uncertainty". The measurement uncertainties include the uncertainties in the measurements due to fluctuations in the characteristics of the receiver components in addition to the radiometric resolution for a particular implementation. Consequently, the radiometric resolution is just one of the

components of the measurement uncertainty. However, in radiometers where the gain or other uncertainties are assumed to be zero or negligible, the term radiometric resolution may be more appropriate to use.

Figure 3-2 shows a model of a basic radiometer in total power mode, consisting of an amplifier, pre-detection filter, a square law detector and a post-detection filter. The equivalent system noise temperature, T_{sys}, at the receiver input is equal to the noise temperature of the receiver, T_{Rec}, plus the effective antenna noise temperature, T_A, delivered to the amplifier. The radiometric resolution of the radiometer in this case is given by (Ulaby et al., 1981):

$$\Delta T_n = \frac{T_{sys}}{\sqrt{B\tau}} = \frac{T_A + T_{Rec}}{\sqrt{B\tau}} \,, \qquad \textbf{Eq 3-3}$$

where τ is the integration time constant, B is the receiver bandwidth. In the ideal case, a 10 mK radiometric resolution can be achieved assuming B=100 kHz, T_A =50 K, T_{Rec}=150 K and an integration time of τ ~1hr. This also suggests that a fractional accuracy of 10 mK in 200 K ($or\ 10\log\left\{1-\frac{0.01K}{200K}\right\} = 0.0002dB$) in the measurement of the output power is required.

In the case of the amplifier gain fluctuations in the total power radiometer, this term adds an additional uncertainty to the radiometric resolution obtained above. As a result, it is more appropriate to define the total measurement uncertainty, in this case, as the root mean square (rms) sum of the two terms:

$$\Delta T_{rms} = \sqrt{\Delta T_n^2 + \Delta T_G^2} \,, \qquad \textbf{Eq 3-4}$$

where $\Delta T_n = \frac{T_{sys}}{\sqrt{B\tau}}$ is the radiometer resolution intrinsic in the total power radiometer and $\Delta T_G = T_{sys}\frac{\Delta G}{G}$, is the term added due to the amplifier gain fluctuations. The total rms uncertainty is now:

$$\Delta T_{rms} = (T_A + T_{Rec})\sqrt{\frac{1}{B\tau} + \left(\frac{\Delta G}{G}\right)^2} \,. \qquad \textbf{Eq 3-5}$$

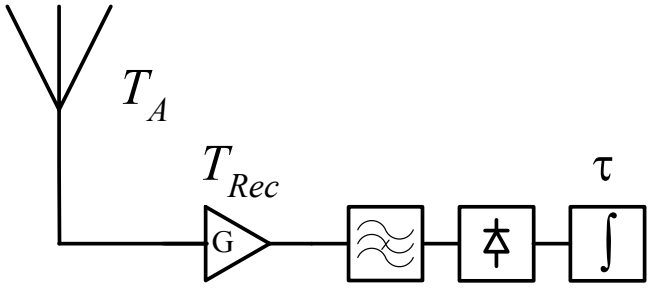

Figure 3-2 Total power radiometer

Eq 3-5 indicates that the gain instability, $\frac{\Delta G}{G}$, decreases the sensitivity in the same way as variations of the receiver noise temperature or of the bandwidth of the receiver. For the above example and assuming a total power radiometer having a gain variation of $\frac{\Delta G}{G} = 0.025 (\sim 0.1 dB)$ the total rms uncertainty would be:

$$\Delta T_{rms} = 200K \sqrt{\frac{1}{100k * 4000} + (0.025)^2} \sim 5K ,$$

which is 500 times the required sensitivity, mainly dominated by the receiver gain variation, $\frac{\Delta G}{G}$. To improve the radiometer measurement uncertainty due to gain variations and other instabilities, calibration is required.

3.4 Radiometer Calibration Techniques

To alleviate these measurement uncertainties, corrections for the radiometer gain variations are required. There are a number of calibration methods available to improve radiometer performance (Tiuri, 1964; Ulaby et al., 1981). For the requirements of this project some of the relevant techniques will be discussed in the following sections.

In one implementation, the radiometer can be used to measure the difference between the antenna temperature and some known reference temperature (Ohm & Snell, 1963), or the receiver may be switched periodically between the antenna and a reference load at rates such that the receiver gain remains essentially steady over the switching period and the output is synchronously detected. This is the idea behind a Dicke or Comparison Switched radiometer (Dicke, 1946).

3.5 Comparison Switched or Dicke Radiometer

The output voltage of a Dicke switch radiometer looks at reference and antenna at different periods of time for synchronous detection, as shown in Figure 3-3. The output of the radiometer in this case can be regarded basically as the difference between two total power radiometers, where one is measuring the antenna temperature and the other the reference noise temperature. The output voltage of the Dicke radiometer, assuming equal integration times between the antenna and reference signals ($\tau/2$), can then be written as:

$$V_{out} = 0.5G\left[(T_A + T_{Rec}) - \left(T_{Ref} + T_{Rec}\right)\right]. \qquad \textbf{Eq 3-6}$$

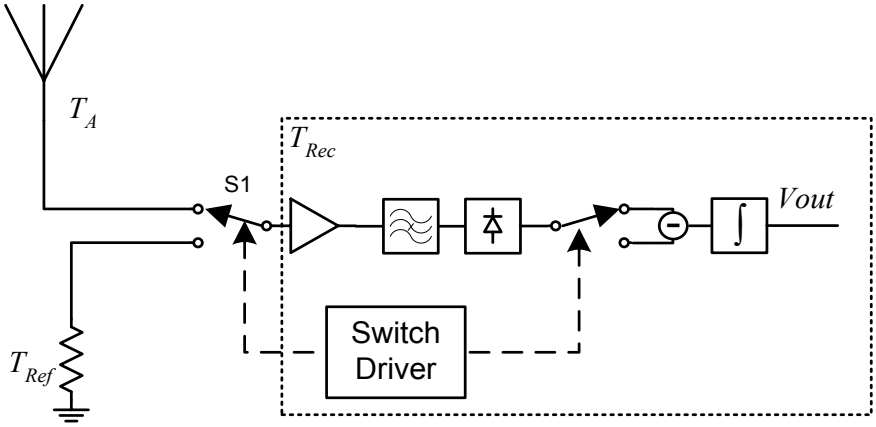

Figure 3-3 Block diagram of a Dicke or comparison switched radiometer

where T_A, T_{Ref}, T_{Rec} is the noise temperature of the antenna, reference load and receiver respectively as shown in the figure above.

The total rms uncertainties due to the intrinsic radiometer resolution of this type and some unknown gain fluctuations are the rms sum of the two terms as follows:

$$\Delta T_{rms} = \sqrt{\Delta T_n^2 + \Delta T_{Gamp}^2} = \sqrt{\Delta T_{NAnt}^2 + \Delta T_{NRef}^2 + \Delta T_{GAmp}^2}\ , \qquad \textbf{Eq 3-7}$$

where $\Delta T_{NAnt} = \frac{T_A + T_{Rec}}{\sqrt{B\tau/2}}$ and $\Delta T_{Nref} = \frac{T_{Ref} + T_{Rec}}{\sqrt{B\tau/2}}$.

ΔT_{NAnt} is the uncertainty due to noise when looking at the antenna arm and divide by two is due to comparison switching intervals. ΔT_{NRef} is the uncertainty due to noise in the reference arm and the uncertainty due to gain fluctuations, in this case, is:

$$\Delta T_{GAmp} = \left(T_A - T_{Ref}\right)\frac{\Delta G}{G}. \qquad \textbf{Eq 3-8}$$

Hence, the total rms uncertainty, ΔT_{rms} , when $T_A \neq T_{Ref}$, can then be written as:

$$\Delta T_{rms_{(ub)}} = \sqrt{\frac{(T_A+T_{Rec})^2}{B\tau/2} + \frac{\left(T_{Ref}+T_{Rec}\right)^2}{B\tau/2} + \left(T_A - T_{Ref}\right)^2\left(\frac{\Delta G}{G}\right)^2}. \qquad \textbf{Eq 3-9}$$

This is known as the unbalanced Dicke Radiometer. The gain fluctuations are now proportional to $\left(T_A - T_{Ref}\right)$ rather than to $(T_A + T_{Rec})$ for a total power radiometer, which is much smaller for T_A values close to T_{Ref} .

In the case of a balanced Dicke radiometer, when $T_A = T_{Ref}$ (ie when the gain fluctuations can be ignored) the total rms uncertainty reduces to radiometer resolution, ΔT_n , as follows:

$$\Delta T_{rms_{(bal)}} = \Delta T_n = \sqrt{\frac{2(T_A + T_{Rec})^2}{B\tau/2}} = \frac{2(T_A + T_{Rec})}{\sqrt{B\tau}}, \qquad \textbf{Eq 3-10}$$

where the radiometric resolution is twice the ideal radiometer of Eq 3-1.

Table 2 shows the comparison of measurement uncertainties for the different types of radiometers described above. It can be seen as T_A approaches T_{Ref} the unbalanced Dicke uncertainty decreases as compared with the total power radiometer.

Table 2 Receiver resolution for different radiometer type

T_A (K)	T_{Ref} (K)	Ideal ΔT_{rms}	Total Power ΔT_{rms}	Unbalanced Dicke $\Delta T_{rms_{(ub)}}$	Balanced Dicke $\Delta T_{rms_{(bal)}}$
290	290	22 mK	11 K	0.25 K	44 mK
100	290	12.5 mK	6.25 K	5 K	-
70	290	11 mK	5.5 K	5.75 K	-

There are different techniques that can be used to minimise the gain fluctuations in a radiometer (Ulaby et al., 1981). Some are discussed in the next section.

3.5.1 Gain Modulated Method

To minimise gain fluctuations in the implementation of a Dicke radiometer, the receiver is switched periodically between the antenna and a reference load at rates that the receiver gain remains essentially steady over one period.

In this case, the receiver gain is dynamically adjusted during the time the Dicke switch is connected to the reference load so as to balance the radiometer output:

$$(T_A + T_{Rec}) = \alpha\left(T_{Ref} + T_{Rec}\right). \qquad \textbf{Eq 3-11}$$

The radiometric resolution is then:

$$\Delta T_n = \sqrt{\frac{(T_A + T_{Rec})^2}{B\tau/2} + \frac{\left(T_{Ref} + T_{Rec}\right)^2}{B\tau/2}}\ , \qquad \textbf{Eq 3-12}$$

which does not depend on gain fluctuations but depends on the receiver's noise temperature. The gain adjustment can be achieved by a voltage controlled or digital step attenuator at the receiver last stage amplifier as shown in Figure 3-4.

One of the advantages of this technique is a simple insertion of an attenuator in the receiver to control gain and balance the radiometer. The disadvantage is that small variations in the receiver noise due to attenuation variations over temperature (in the order of ±0.1 dB) can directly affect T_A if the receiver is not temperature controlled.

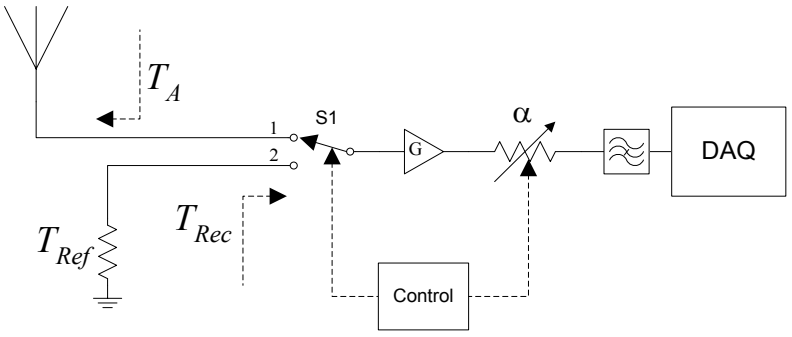

Figure 3-4 Balanced Dicke radiometer using gain modulated method

3.5.2 Reference Channel Method

In this case, the reference noise temperature, T_{Ref}, is adjusted by controlling a variable attenuator at a physical temperature, T_0, which is connected to a noise source, T_N, as shown in Figure 3-5. The reference noise temperature measured

here is the combination of noise temperature of the noise source and the attenuator according to:

$$T_{Ref} = \frac{T_N}{L_0} + T_0\left(1 - \frac{1}{L_0}\right). \qquad \textbf{Eq 3-13}$$

The attenuator is adjusted so that T_{Ref} becomes equal to T_A. Using this method, T_{Ref} can vary between $L_0 \sim 1$ $\left(ie\ T_{Ref} = T_N\right)$ and $L_0 \sim \infty$ $(ie\ T_{Ref} = T_0)$. T_N and T_0 should cover the expected range of the antenna noise temperature, T_A. For a digital step attenuator range of 1.26 (1 dB) to 1000 (30 dB), noise source temperature of T_N = 400,000 K (~ -143 dBm/Hz) and $T_0 = 300\ K$, T_{Ref} will be between 320,060 K and 700 K.

The radiometer resolution, in this case, is:

$$\Delta T_n = \frac{2(T_A + T_{Rec})}{\sqrt{B\tau}}. \qquad \textbf{Eq 3-14}$$

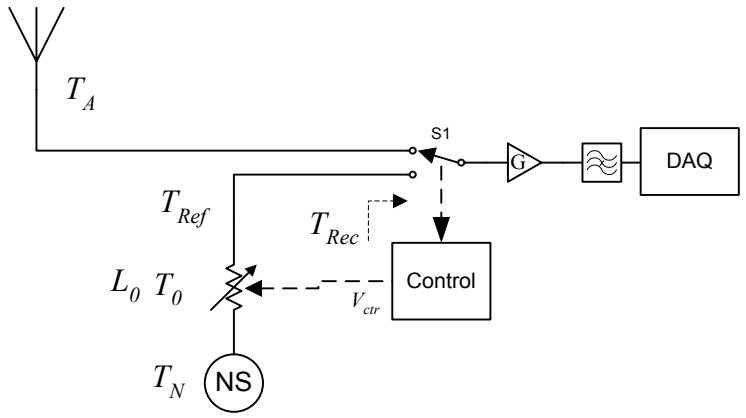

Figure 3-5 Balancing Dicke radiometer using reference channel method

One of the advantages of this technique is that a voltage controlled attenuator or a digital step attenuator can be used to control the reference temperature, T_{Ref}. The disadvantage is that the impedance mismatches between when the switch is at the reference arm position and the antenna arm may not be stable during the calibration cycle.

3.5.3 Noise Injection Method

In a modified implementation, a known amount of noise can be coupled into the antenna port to balance with the antenna noise temperature, during half the period of Dicke switching, as shown in Figure 3-6.

In this method, a known amount of noise, T_N, is injected into the antenna port using a directional coupler, with a coupling factor of L_{cpl}, to balance the reference arm, T_{Ref}, with the input noise temperature at the input switch, $T''_A = T_A + T'_N$, so $T_A + T'_N = T_{Ref}$. This can be carried out by adjusting an attenuator at the output of the noise source and the radiometric resolution is thus equal to:

$$\Delta T_n = \frac{2\left(T_{Ref} + T_{Rec}\right)}{\sqrt{B\tau}}. \quad \textbf{Eq 3-15}$$

The input noise temperature at the input switch can be written as:

$$T''_A = \frac{T'_N}{L_{cpl}} + T_A\left(1 - \frac{1}{L_{cpl}}\right), \quad \textbf{Eq 3-16}$$

where the noise source temperature at the coupled port, T'_N, is:

$$T'_N = \frac{T_N}{L_0} + T_0\left(1 - \frac{1}{L_0}\right). \quad \textbf{Eq 3-17}$$

Combining the two equations above, attenuation loss, L_0, can be calculated as:

$$L_0 = \frac{T_N - T_0}{\left(L_{cpl} - 1\right)(T_0 - T_A)}, \quad \textbf{Eq 3-18}$$

where T_0 is the physical temperature of the attenuator kept at the same temperature as the reference, T_{Ref}. If the control voltage, V_{ctr} is scaled and linearised so that $V_{ctr} = 1/L_0$ then it becomes proportional to T_A, assuming T_0 and T_N remain constant, and Eq 3-18 can be re-written as:

$$V_{ctr} = \left(L_{cpl} - 1\right)\frac{(T_0 - T_A)}{(T_N - T_0)}. \quad \textbf{Eq 3-19}$$

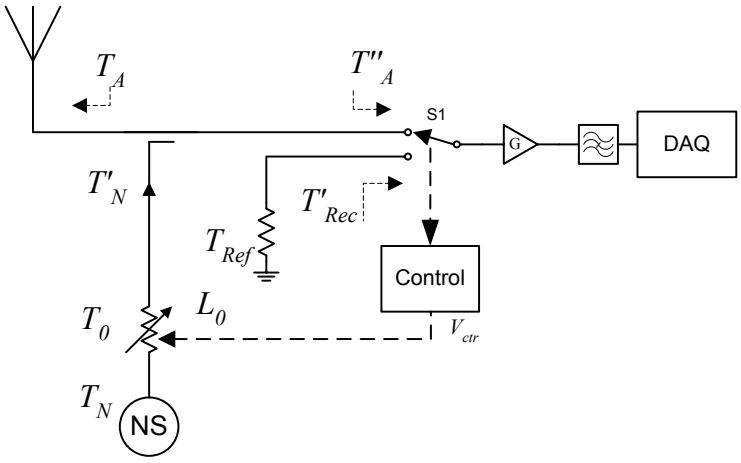

Figure 3-6 Balancing Dicke radiometer with antenna noise injection method

One of the advantages here is that depending on the range of T_A, an acceptable range of attenuation can be realised easily. On the other hand, the switch insertion loss can increase the receiver noise figure decreasing the radiometric sensitivity. In addition, the switch isolation determines the measure of leakage between the antenna arm and the reference arm. A 20 dB isolation between the two channels couples 1% of noise from one arm to the other arm. Reference arm leakage may be factored out as it is kept stable, but received noise from the antenna arm leakage may vary and cannot be factored out. So a high isolation switch may also be required.

3.6 Correlation Radiometer

This is a dual input radiometer with a digital correlator. The received signals from the two inputs are amplified, digitised and processed in a digital correlator.

In the correlation receiver, shown in Figure 3-7, the signal from the antenna arm and the reference arm are fed into a 180º wideband hybrid. The sum and difference of the two signals are then amplified in two low noise amplifiers. In the back-end the two channels are digitised and correlated. Assuming that the noise powers in each amplifier channel are uncorrelated and the coupling between the two arms are low enough; they are removed by cross-correlation at the output of the digital correlator. In this case:

$$T_{Ref} = \frac{T_N}{L} + T_0\left(1 - \frac{1}{L}\right). \qquad \textbf{Eq 3-20}$$

And the correlation radiometer resolution, in this case, is equal to:

$$\Delta T_n = \frac{\sqrt{2}(T_A + T_{Rec})}{\sqrt{B\tau}}. \qquad \textbf{Eq 3-21}$$

The insertion loss of the hybrid will be absorbed by cross correlation.

An advantage of the correlation radiometer is that it requires no switching scheme and as a result avoiding the input switch losses associated with a Dicke type radiometer.

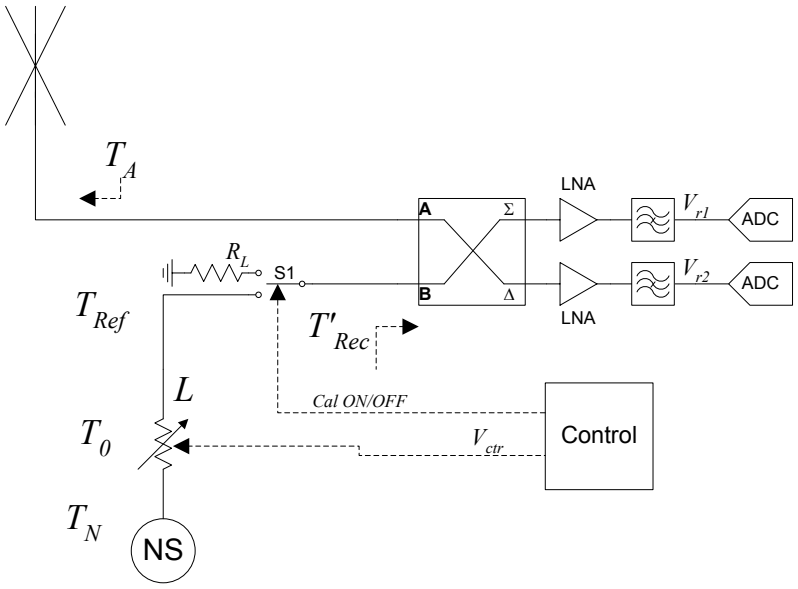

Figure 3-7 Block diagram of a correlation radiometer

3.7 Noise Adding Radiometer

This type of radiometer is useful to remove the effects of gain fluctuations without the use of a comparison (or Dicke) switch (Ohm & Snell, 1963). In this method, a known amount of noise, T_N, is periodically coupled into the antenna port and combined at the amplifier input as shown in Figure 3-8. This is known as the noise adding radiometer (NAR). By switching the noise source on and off periodically with the output voltage synchronously detected, an output voltage ratio V_r, can be formed as follows:

$$V_r = \frac{V_{Noff}}{V_{Non} - V_{Noff}} , \qquad \textbf{Eq 3-22}$$

where V_{Non} and V_{Noff} are the output voltages measured when noise source is on or off, respectively. The subtraction function in the above equation may be performed with analog or digital electronics.

Now substituting the output voltages with their equivalent noise temperatures, the voltage ratio can be written as:

$$V_r = \frac{(T'_A + T_{Rec})G}{(T'_A + T''_N + T_{Rec})G - (T''_A + T_{Rec})G} \qquad \textbf{Eq 3-23}$$

$$= \frac{(T'_A + T_{Rec})}{T''_N},$$

where T'_A and T''_N are the antenna and the calibrated noise source temperatures seen at the amplifier input and T_{Rec} and G are the receiver temperature and gain, respectively.

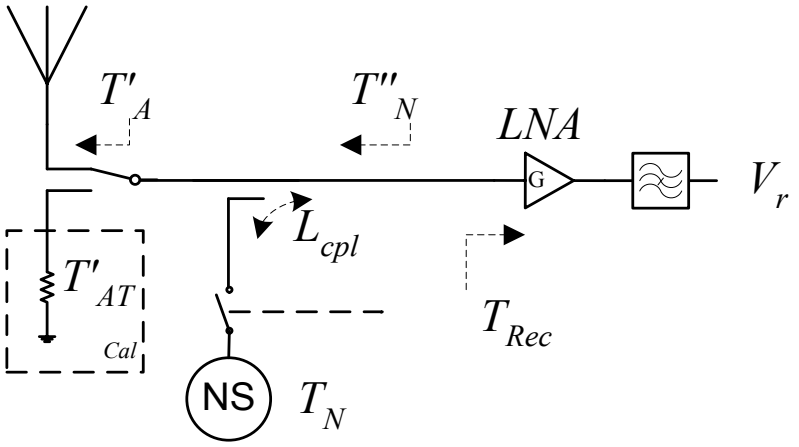

Figure 3-8 Noise adding radiometer

Eq 3-23 shows that this voltage ratio is independent of the receiver gain, G, when the noise source on period, V_{Non}, follows the noise source off period, V_{Noff}, so closely that the gain has not changed appreciably.

From the above, T'_A can be found from the measured voltage ratio results as follows:

$$T'_A = V_r T''_N - T_{Rec}\,, \qquad \textbf{Eq 3-24}$$

where T''_N is equal to T_N, the temperature of the calibrated noise source divided by L_{cpl}, the coupling factor, as follows:

$$T''_N = \frac{T_N}{L_{cpl}}\,. \qquad \textbf{Eq 3-25}$$

Substituting Eq 3-25 into Eq 3-24, the actual antenna temperature, T'_A, can then be determined according to:

$$T'_A = V_r \frac{1}{L_{cpl}} T_N - T_{Rec}. \qquad \textbf{Eq 3-26}$$

The noise source temperature, T_N, can be calibrated by connecting the receiver input to an ambient termination, T'_{AT}. Then knowing T_{Rec}, L_{cpl} and measuring the voltage ratio, V_r, the noise source temperature can be determined from Eq 3-26 as follows:

$$T_N = \frac{L_{cpl}}{V_r}(T''_{AT} + T_{Rec}) . \quad \text{Eq 3-27}$$

One of the advantages of this technique is that due to Eq 3-23, the measurement of T'_A is independent of the receiver gain variations. And as there is no comparison (or Dicke) switch, the receiver input loss associated with the switch (typically 14-35 K), assuming insertion loss associated with the directional coupler is negligible, is decreased therefore increasing the radiometric sensitivity.

However, as can be seen in Eq 3-26, the resultant accuracy is directly proportional to the stability of the receiver noise temperature, T_{Rec}, the calibrated noise source, T_N, and coupler loss used over the measurement cycle.

The resolution of the noise adding radiometer, for equal on and off integration periods, can be determined using the small signal approximation (Ulaby et al., 1981) and can be written as follows:

$$\Delta T_n = \frac{2(T'_A + T_{Rec})}{\sqrt{B\tau}}\left(1 + \frac{T'_A + T_{Rec}}{\frac{T_N}{L_{cpl}}}\right). \quad \text{Eq 3-28}$$

Eq 3-28 above indicates that for large values of T_N, i.e. $\frac{T'_A+T_{Rec}}{\frac{T_N}{L_{cpl}}} \ll 1$ and as long as the receiver amplifier is not saturated, the NAR resolution approaches that of the balanced Dicke radiometer of Eq 3-10. It should also be noted that for large values of T_N , the noise leakage through the switch can unintentionally add extra noise fluctuations to the measured antenna temperature. For a 60 dB isolation in the switch, and a $T_N = -130$ dBm/Hz (or 7,242,963 K) noise source, this would add (7.2 K) during the off state.

3.8 Noise Adding Comparison Radiometer

The radiometer developed in later chapters for the EoR experiment combines a noise adding radiometer with the addition of a comparison (or Dicke) switch. In this thesis, this is referred to as Noise Adding Comparison (NAC) radiometer. The Dicke switch can toggle between the antenna input and the reference input and the internal noise source can be added to both the antenna and the reference input for calibration purposes as depicted in Figure 3-9. The Dicke switch is the first element as close to the antenna input port as possible in the front-end module. The noise adding switch is between the output of the internal noise source and the

coupled arm of the directional coupler. The combination of the noise adding and Dicke switch is used to reduce receiver temperature and gain instabilities.

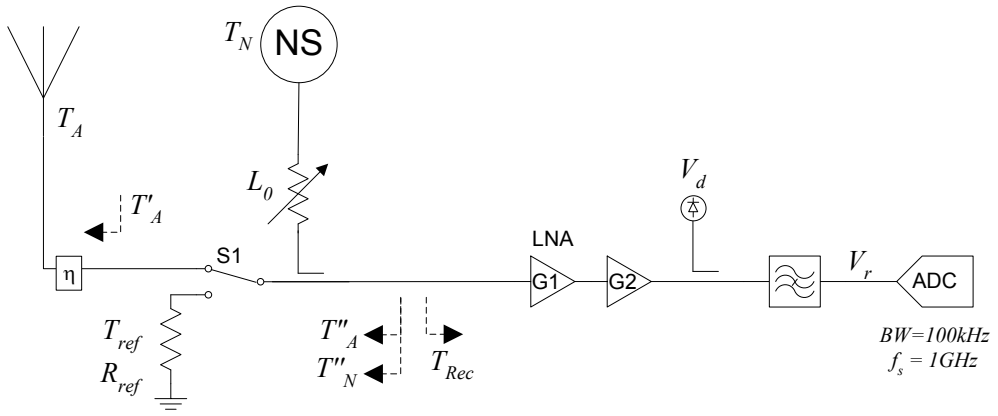

Figure 3-9 The proposed NAC radiometric receiver

The advantage of this type of radiometer is that it has the potential to improve the calibration stability by switching a calibrated noise source periodically as well as reducing radiometer sensitivity by cancelling out the gain and receiver noise temperature at the Dicke switching rate (Wilson & Tanner, 2002). Such calibrated noise sources are readily available off the shelf as a packaged surface mount component. Additionally, provided the physical temperature and bias current are kept constant, the output power is extremely stable over long periods of time.

As a result, the long term stability relies on the stability of the internal noise source and the front-end input losses and the accuracy of their measured temperatures.

In this method, the calibrated noise source is used to periodically inject a known amount of noise to the antenna port or reference port using a directional coupler. The noise source level injected through the coupling arm is adjusted by a digital step attenuator at the output of the noise source.

The excess noise temperature generated at the coupled port of the coupler due to the internal noise source, T_N , can be written as:

$$T'_N = \frac{T_N}{L_0} + T_0\left(1 - \frac{1}{L_0}\right), \qquad \text{Eq 3-29}$$

where T_N is the noise temperature of the noise source, T_0 is the physical temperature of the attenuator and L_0 is the attenuation loss factor. In the case of a

zero loss factor, when $L_0 = 1,\ T'_N = T_N$. This excess noise at the output of the coupler will then be:

$$T''_N = \frac{T'_N}{L_{cpl}} \qquad \text{Eq 3-30}$$

$$= \frac{1}{L_{cpl}}\left\{\frac{T_N}{L_0} + \left(1 - \frac{1}{L_0}\right)T_0\right\},$$

Now due to the insertion loss of the coupler and Dicke switch, the antenna temperature measured at the amplifier input port can be written as:

$$T''_A = \frac{T'_A}{L_1} + \left(1 - \frac{1}{L_1}\right)T_1, \qquad \text{Eq 3-31}$$

where L_1 is the combined loss of the Dicke switch (S1) and the coupler insertion loss at a physical temperature, T_1, as shown in Figure 3-10. Eq 3-31 indicates that when T''_A is measured, T'_A can be calculated using measured quantities of loss and the physical temperature.

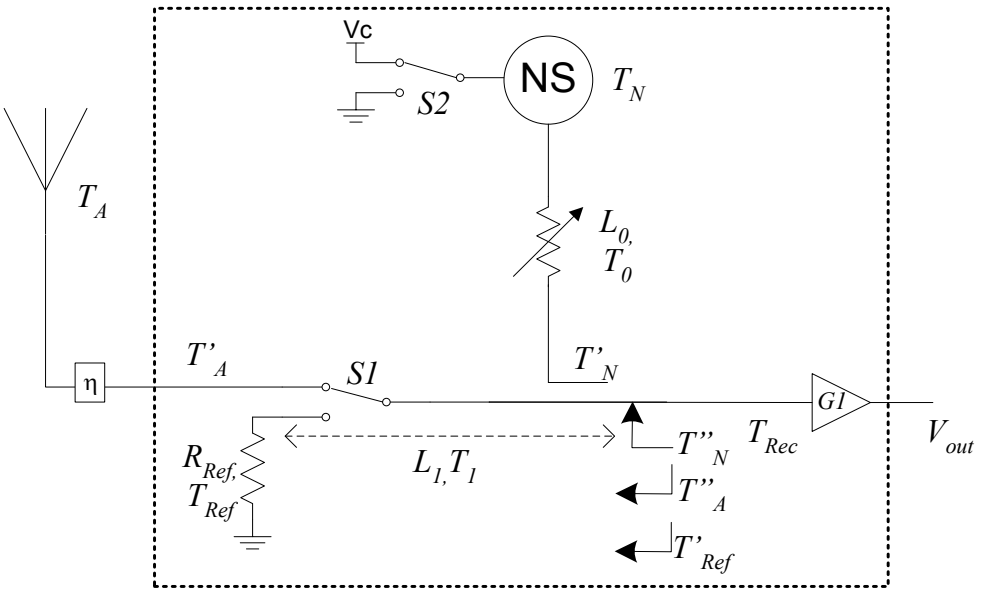

Figure 3-10 Schematic diagram of the DAC radiometer model

The system noise temperature when the noise source (NS) is off or on, and S1 is switched to the antenna input, can then be written as:

$$T_{sys(NSoff)} = T''_A + T_{Rec}\ , \qquad \text{Eq 3-32}$$

$$T_{sys(NSon)} = T''_A + T''_N + T_{Rec}\ . \qquad \text{Eq 3-33}$$

In this implementation, the combination of noise adding switch, S2 and comparison switch S1 can effectively measure $T'_A \; and \; G$ in real time at the Dicke switching rate and calibrate them out.

For the combined input switch loss of $L_{sw} = 0.2dB$ (1.047), and coupler insertion loss of $L_{il} = 0.7\ dB$ (1.175), at ambient temperature, $T_1 = 300\ K$, and the minimum antenna temperature, $T'_A = 80\ K$, the insertion loss contribution would be 56 K and the increase in the input noise temperature, ΔT, from Eq 3-31 would be 41 K. This indicates that a 0.9 dB front-end loss would add 41 K to the measured antenna noise at the output of the coupler.

$$L_1 = L_{sw} + L_{il} = 0.9\ dB\ (1.230). \qquad \textbf{Eq 3-34}$$

$$\begin{aligned} \Delta T &= T''_A - T'_A \\ &= (T_1 - T'_A)(1 - 1/L_1) \\ &= 0.187\ (T_1 - T'_A)\ K \\ &\sim 41\ K. \end{aligned} \qquad \textbf{Eq 3-35}$$

By the same token, any errors in the order of 0.01 dB (1.0023) in coupler and switch losses at physical temperature of 300 K, could contribute 690 mK of error to the calculated antenna noise temperature. However, these errors can be assumed fixed and thus will only add a constant bias and by accurate measurements the antenna temperature can be determined.

3.8.1 Radiometer Internal Calibration

The comparison (S1) and noise adding (S2) switches can be combined to provide a maximum of four measurement states. The measurement states of the radiometer correspond to observations of the antenna temperature, T_A, or internal calibration reference temperatures T_{AN}, T_{Ref}, T_{Cal}. As a result, the output of the radiometer at any instance corresponds to only one of these four states. Each state can be treated separately and operates as a total power radiometer.

Consequently, the input to the radiometer can be decomposed into the following four independent power spectra (Rogers & Bowman, 2008):

$$P_{Ref} = \left(T'_{Ref} + T_{Rec}\right)\kappa BG\ , \qquad \textbf{Eq 3-36}$$

$$P_{Cal} = \left(T'_{Ref} + T''_N + T_{Rec}\right)\kappa BG\ , \qquad \textbf{Eq 3-37}$$

$$P_A = (T"_A + T_{Rec})\kappa BG\ ,$$ **Eq 3-38**

$$P_{AN} = (T"_A + T"_N + T_{Rec})\kappa BG,$$ **Eq 3-39**

where $P_{Ref}, P_{Cal}, P_A, P_{AN}$ are the power spectra measured by the receiver for each state. In this case, κ is the Boltzmann's constant, B and G are the receiver bandwidth and gain, and $T'_{Ref}, T"_N, T_{Rec}, T"_A,$ are the ambient reference temperature, the calibrated noise source temperature, the receiver noise temperature, and the antenna noise temperature at the output of the coupler, respectively, as shown in Figure 3-9.

These four states can be combined to produce a calibrated estimate of the true antenna temperature. To estimate the antenna noise temperature, a power ratio can be formed based on the three states of the radiometer's observables, P_{Ref}, P_{Cal}, P_A, as follows:

$$E = \frac{(P_A - P_{Ref})}{(P_{Cal} - P_{Ref})}$$ **Eq 3-40**

$$= \frac{(T"_A - T'_{Ref})}{T"_N}.$$

Eq 3-40 shows that this ratio is independent of the receiver gain, G, and noise temperature, T_{Rec}, assuming the switching periods follow each other closely that the receiver gain has not changed appreciably.

Having measured the power ratio, E, the antenna noise temperature at the output of the coupler can be estimated from:

$$T"_A = T'_{Ref} + ET"_N.$$ **Eq 3-41**

Converting the noise temperatures at the output of the coupler to the front-end input reference, T'_{Ref} and $T"_N$ can be written as:

$$T'_{Ref} = \frac{T_{Ref}}{L_1} + \left(1 - \frac{1}{L_1}\right) T_1.$$ **Eq 3-42**

And

$$T''_N = \frac{1}{L_{cpl}}\left[\frac{T_{Non}}{L_0} + \left(1 - \frac{1}{L_0}\right)T_0 - \frac{T_{Noff}}{L_0} - \left(1 - \frac{1}{L_0}\right)T_0\right], \quad \text{Eq 3-43}$$

$$= \frac{1}{L_{cpl}}\left[\frac{T_{Non} - T_{Noff}}{L_0}\right],$$

$$= \frac{1}{L_{cpl}}\left[\frac{T_N}{L_0}\right],$$

where T_N, the calibrated internal noise source, is equal to $T_{Non} - T_{Noff}$ and L_0, L_1, L_{cpl} and T_0, T_1 are the losses and noise temperatures due to attenuators and the coupler used for calculating the radiometer input parameters.

Substituting, Eq 3-42, Eq 3-43 and Eq 3-31 into Eq 3-41 gives the actual antenna temperature, T'_A, at the front-end input, which can be determined as follows:

$$T'_A = T_{Ref} + EL_1 \frac{1}{L_0 L_{cpl}} T_N = T_{Ref} - L\,T_N, \quad \text{Eq 3-44}$$

where $L = EL_1 \frac{1}{L_0 L_{cpl}}$.

Eq 3-44 indicates that the antenna temperature is directly related to the reference temperature, T_{Ref}, the internal noise source temperature, T_N, and the front-end losses, L, and that these values have to be measured with a high precision.

In reality, the impedance match between the antenna and the front-end input port will not be ideal, and some of the noise may reflect back and introduce deviations between the estimated and the effective antenna temperatures. In this case, the effective antenna temperature can be found from:

$$T'_A = (1 - |\Gamma|^2)T_A, \quad \text{Eq 3-45}$$

where Γ is the antenna reflection coefficient.

3.8.2 Radiometer Resolution

If the first three power spectra (Eq 3-36, Eq 3-37, Eq 3-38) are used to calculate the power ratio C, the radiometer resolution, assuming equal integration times, can be written as the rms sum of the noise temperature terms in each radiometer state as follows (7.1 Appendix A):

$$\Delta T_{rms} = \sqrt{\frac{1}{B(\tau/3)}}\sqrt{(T''_A + T_{Rec})^2} + \sqrt{\frac{1}{B\tau/3}}\sqrt{\left(T''_A - T'_{Ref}\right)^2\left(1 + \frac{T'_{Ref} + T_{Rec}}{T''_N}\right)^2} + \sqrt{\frac{1}{B\tau/3}}\sqrt{\left(T'_{Ref} + T_{Rec}\right)^2\left(\frac{T''_A - T'_{Ref}}{T''_N} - 1\right)^2}. \quad \text{Eq 3-46}$$

When the receiver temperature is $T_{Rec} = 100\ K, T'_A = 300K, T'_{Ref} = 310K$, $T''_N = 1700$, $B = 100\ kHz$, integration time of $\tau = 1\ hr$, and equal time spent on each switching state, the radiometer resolution should be reduced to 0.8 K at the input antenna temperature of 5000 K (which is expected to be at frequency of 50 MHz). To reduce the resolution, ΔT_{rms}, to 50 mK this requires 9 days of continuous observations.

Figure 3-11 shows the comparison of radiometer resolution between a NAC and NA radiometer vs an ideal radiometer (Eq 3-3) plotted as a function of T'_A for the parameters mentioned above.

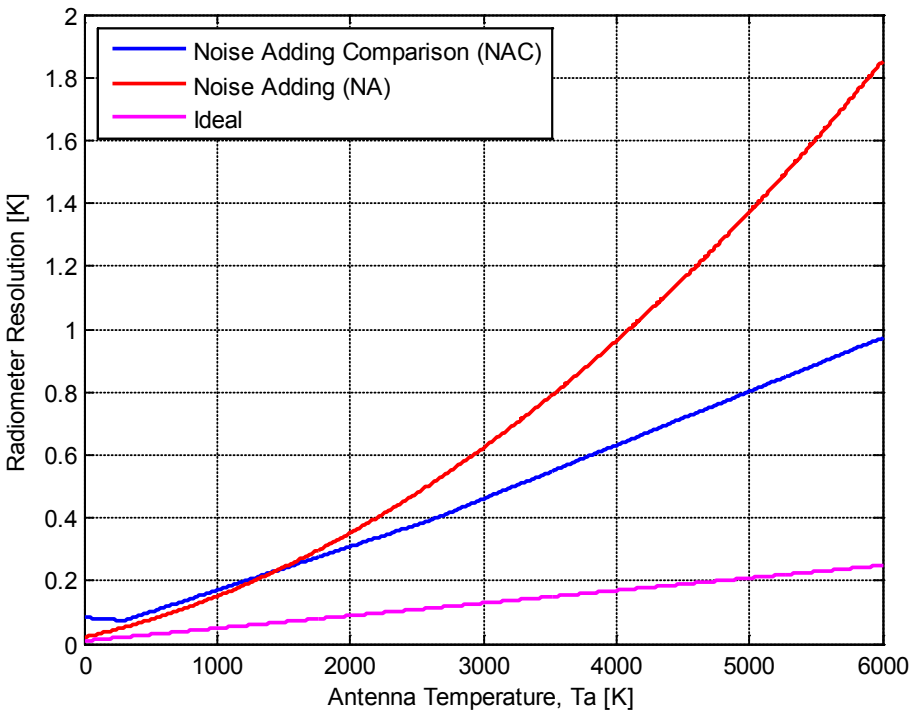

Figure 3-11 NAC vs. NA radiometer resolution using 3-state switching

For noise source temperature $T''_N \gg T'_{Ref}$, the radiometer measurement rms uncertainty can be simplified to:

$$\Delta T_{rms} = \sqrt{\frac{(T''_A + T_{Rec})^2 + \left(T''_A - T'_{Ref}\right)^2 + \left(T'_{Ref} + T_{Rec}\right)^2}{B(\tau/3)}}. \quad \textbf{Eq 3-47}$$

To configure the receiver as a noise adding comparison radiometer, a software program on the host computer in the back-end rack can appropriately send RS485 commands to toggle S1 and S2 switches periodically in the front-end module. A data acquisition unit in the back-end rack is then used to digitise the received signal, perform spectral analysis, and accumulate data for a predefined duration at each of the switch states. This loop is repeated for the duration of the observation period. The results are then recorded to a hard disk on the back-end for later post-processing of the antenna temperature.

3.8.3 Receiver Noise Budget

To design a radio receiver a noise budget analysis is required. This is to estimate the total gain required, accounting for any losses in the system from the antenna port to the digitiser input port. In this case the required input to an 8-bit data acquisition back-end system is approximately -10 dBm. The receiver bandwidth is expected to be between 50 MHz and 250 MHz. Based on the operating frequency range of the receiver for the EoR experiment, the expected sky temperature range is expected to be between 80 K (~ -180 dBm/Hz) and 5000 K (~ -162 dBm/Hz).

The receiver consists of two blocks, a front-end module and a gain module separated by 100 m of cable. Assuming a receiver noise figure of 2 dB for a -172 dBm/Hz minimum noise detection in the front-end module, and a 5 dB average loss in the cable, the total gain required can be determined as follows:

$$-172\ \frac{\text{dBm}}{\text{Hz}} + 83\ \text{dBHz} - 5\ \text{dB} - (-10\ \text{dBm}) = -84\ \text{dB}. \quad \textbf{Eq 3-48}$$

This means that 84dB gain is required in the receiver to provide -10dBm to the data acquisition system. In Eq 3-48 above, 83 dBHz on the left side of the equation, is the noise power due to receiver bandwidth of 200 MHz. This required receiver gain can be divided between the two receiver blocks with a front-end module having a 40 dB gain to improve sensitivity, and then 43 dB gain in the

gain module to raise the signal level to the required digitiser input level. A digital attenuator can be added in the gain module for fine adjustment of the amplification as required during observations.

Figure 3-12 shows the estimated gain calculations for individual blocks in the receiver.

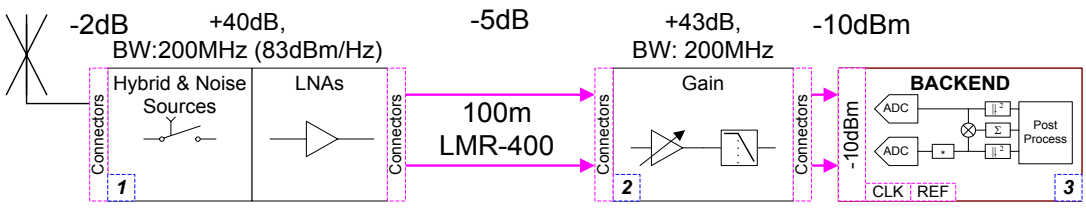

Figure 3-12 BIGHORNS receiver gain calculations

CHAPTER 4

4 Receiver Architecture

This chapter begins with a brief description and configuration of the EoR experimental system in which the radiometric receiver is to be deployed. It then describes the architecture and implementation of the radiometric receiver, as well as the calibration process. The thesis deals with the first type of calibration, referred to as internal calibration, to compensate for fluctuations in the active components of the receiver, using switched calibration references in the receiver. Descriptions of other steps to calibrate the overall system response including the effects of the antenna, external input balun, mismatches between balun and antenna, cable mismatches between balun and the receiver input before Dicke switch and temperature effects external to the receiver enclosure, are not within the scope of this thesis.

4.1 BIGHORNS Experiment

The EoR experimental system consists of three main interconnecting blocks, a broadband antenna, a low noise radiometric receiver, and a digital back-end, as shown below. This project was aimed at building the receiver block and integrating it with the rest of the system. The integration of the three main blocks will constitute a Broadband Instrument for the Global HydrOgen ReionisatioN Signal (BIGHORNS) as shown in Figure 4-1

The experimental system is a direct conversion (i.e. no mixing to intermediate frequency) receiver system. It uses no analog detection but instead direct sampling at the RF frequency in the back-end signal processing unit. The back-end processor is a combined multiple channel 1Gsamples, 8-bit data capture and spectrometer board (originally designed for the LUNASKA experiment) with four built-in Xilinx SX95 FPGAs (James et al., 2010) to channelise and accumulate data at a few second intervals. The digital back-end consists of a data acquisition unit (DAQ), a master control unit (MCU) and a power supply unit (PSU) in an RF shielded rack that includes the batteries to power the system. The output data are

transferred via optical fibre to a compact low power ruggedised PC in the MCU for storage and post-processing.

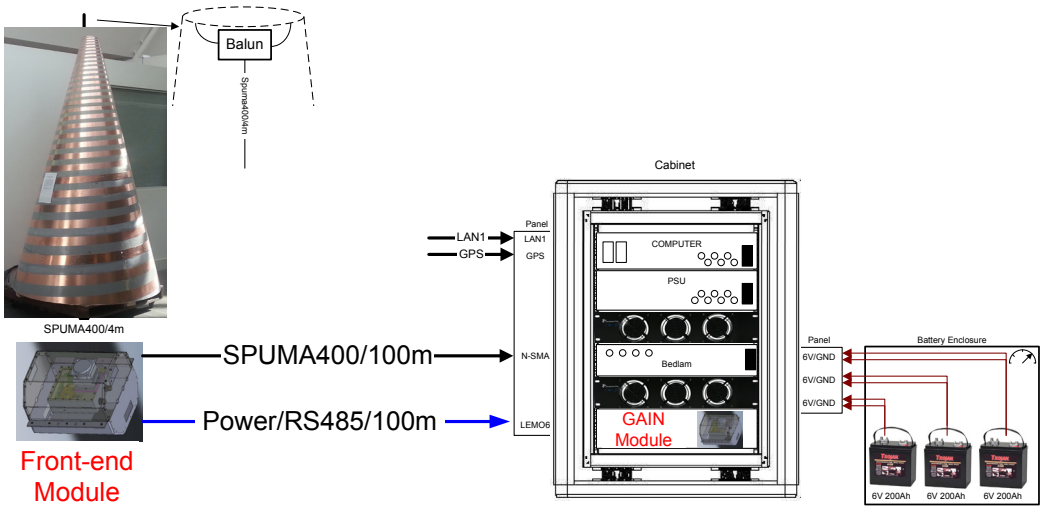

Figure 4-1 Conceptual setup of the BIGHORNS experiment

An antenna with a broad and smooth frequency response should be chosen to assist with accurate calibration of the receiver bandpass characteristics. This demands the antenna pattern to be near frequency independent, so the foreground sky noise does not cause erroneous results in the measurement of the global signature. The receiver front-end and antenna should also be well matched to reduce cable reflections between the antenna and the front-end. The receiver front-end is to be mounted as close as possible to the antenna terminals to reduce input loss variations to a minimum. A log conical spiral antenna has been chosen by the team at ICRAR for preliminary testing.

To connect the antenna and digital back-end, the receiver was implemented in two blocks, a front-end module and a gain module. The front-end module and antenna are separated by 100 m of high quality coaxial cable from the gain module and digital back-end rack as depicted in Figure 4-1.

4.2 Receiver General Description

The receiver consists of two interconnecting modules, a front-end module and a gain module, each having a microcontroller board for monitor and control by the digital back-end rack. The receiver gain is distributed in the two receiver modules. The front-end module comprises the radiometer components, a low noise high dynamic range gain section and a low pass filter. The gain module comprises of a

multi-stage gain control section followed by a digitally controlled attenuator and a sharp anti-alias filter. RF shielded coaxial cables run between the receiver front-end module and the gain module in the back-end rack. Another double shielded twisted pair cable provides DC voltage and control signals for the front-end and gain modules. Both receiver modules are powered by batteries in the digital back-end rack.

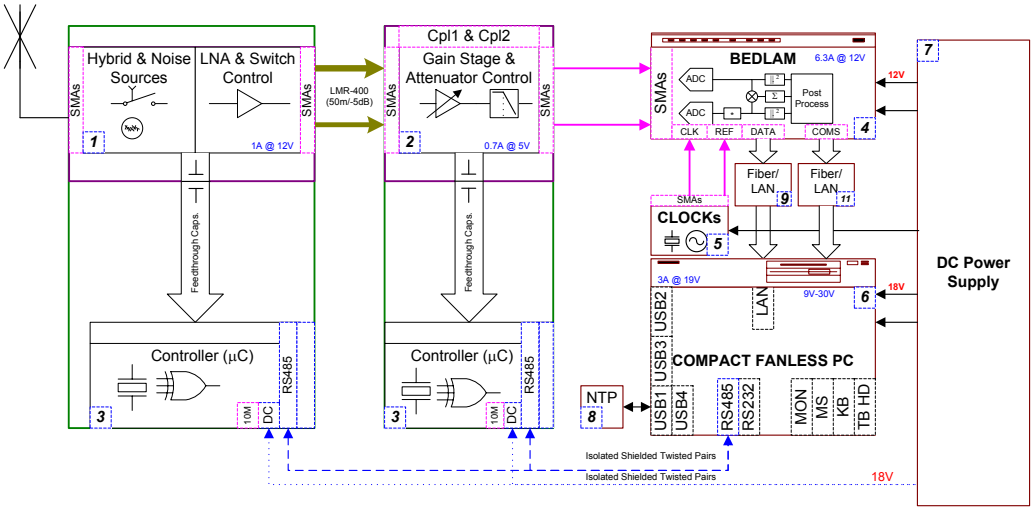

Figure 4-2 BIGHORNS receiver front-end and back-end integration

The receiver modules have been designed with the following common sections and interconnections:

i. A common controller PCB design having a dedicated RS485 transceiver, a 32-bit PIC flash microcontroller featuring a number of 10-bit ADCs, a dedicated SPI and a serial interface on-board for monitoring and controlling the RF boards;

ii. Precision Temperature Sensors (TI LM-35), T1 and T2, on the RF side to measure the board temperature where the reference sources (i.e. the internal 50Ω and internal noise source) and LNAs are;

iii. Temperature Sensor, T3, on the Controller side to measure the case temperature;

iv. Humidity Sensor (Honeywell HIH-5031), H, on the RF side to monitor internal humidity during field tests;

v. Serial peripheral interface (SPI) bus to control digital attenuators on the RF side;

vi. Voltage monitors to measure the input DC voltages supplied to the LNAs and noise sources, for instance.

A high level of RF shielding was mandated for the receiver modules. For this reason, the designed receiver enclosures were machined from a solid aluminium block with two cavities on the opposite side to isolate the RF and controller (MC) boards with each side having a separate lid. The two sides of the enclosure are shown in Figure 4-3. The receiver enclosure dimensions are 130x140x50 mm and weighs 2kg. There are two 50 Ω RF input and output connectors on either end, allowing for single or dual channel receiver configurations. The N-type RF and power connectors are ruggedised hermetically sealed and high isolation RF connectors for use in the outside environment. The aluminium enclosure is RF sealed using a solid circular strip of conductive silver plated elastomer around the perimeter. When compressed by screws on the lid it can provide high shielding effectiveness. The enclosure is finally nitrogen purged to essentially remove any residual humidity or moisture out of the system, keeping the internal circuitry moisture-free during its operational life in the field. This is needed to maintain the stability of the RF circuits as well as the FR4 circuit boards. The nitrogen purge can be injected through the sides. The controller address is configured using jumper leads on controller side to act either as a front-end (Address:1) or gain (Address:2) module.

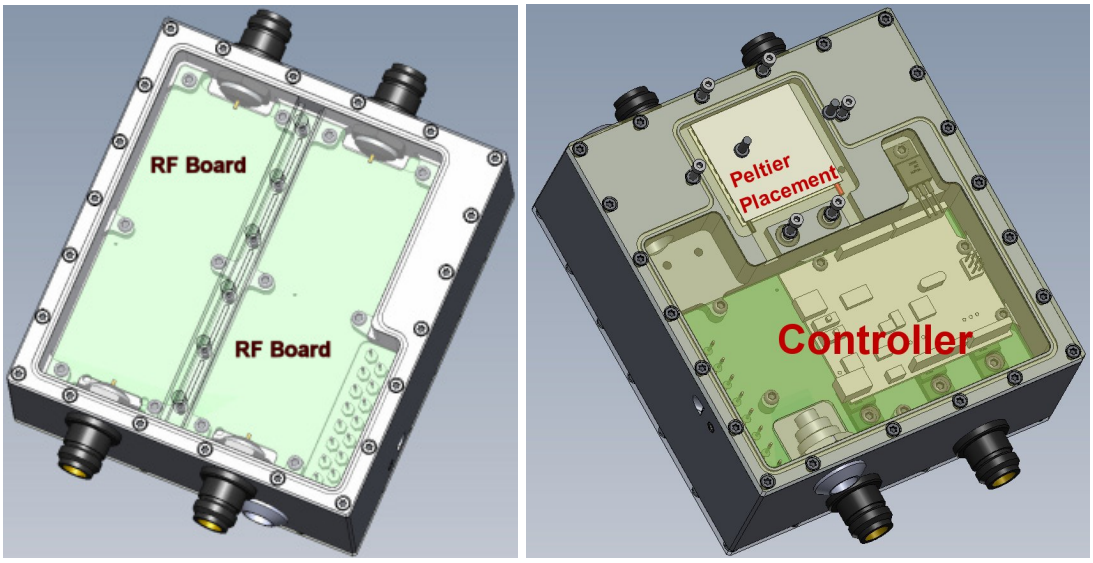

Figure 4-3 Receiver enclosure 3D model showing the RF board mounted on one side and the controller board mounted on the opposing side

4.3 Front-end Module Architecture

The front-end module consists of two 6-layer FR4 PCBs, an RF board and an MC board, on opposing side of the enclosure. The receiver front-end, consisting of radiometer components, low noise amplifiers and low pass filter, was implemented on the RF board. Surface mount components employed for the radiometer minimize the size and improve thermal stability by placing critical radiometer components and transmission lines in close proximity to the temperature sensors. The microcontroller, digital circuitry and regulators were implemented on the MC board on the other side of the enclosure.

The receiver front-end module is a noise adding comparison radiometer system that can be configured in different modes, such as total, noise adding and Dicke switching modes. In addition, the front-end module can be manually configured as a single input radiometer (CH1) or dual input for use in a correlation radiometer (CH1 and CH2) using an additional internal surface mount hybrid and a second low noise amplifier. There are two amplifier chains, CH1 & CH2, in the front-end module as a result. The CH2 chain amplifiers are turned off at start up by the microcontroller. The front-end block diagram for a single input arrangement is shown in Figure 4-4.

The front-end module consists of a Dicke relay switch (S1) at the input to the antenna port, followed by a 10 dB directional coupler, a dual stage low noise amplifier (LNA) and a lowpass filter (LPF) at the output. The placement of the comparison switch in this case is an important part of the front-end design. By placing the S1 switch right at the input of the front-end module, as will be shown in section 4.7, the systematic uncertainties due to the switch and coupler losses can be calibrated out right at the antenna input. A surface mount noise source (NS) module at the coupled input (CPL) is used to add a known amount of excess white noise to the antenna or reference arms to reduce the receiver gain variations. The reference arm (REF) consists of a microwave thin film surface mount 50 Ω resistor (Mini Systems WAMT-5A) with a 1% tolerance and temperature coefficient of 5 mΩ/K. An RF relay switch (S2) and a digitally controlled attenuator (L) in series with the noise source are also used to control the switching

period and level of injected noise to the input arm. The attenuator settings and switching rates are software controlled.

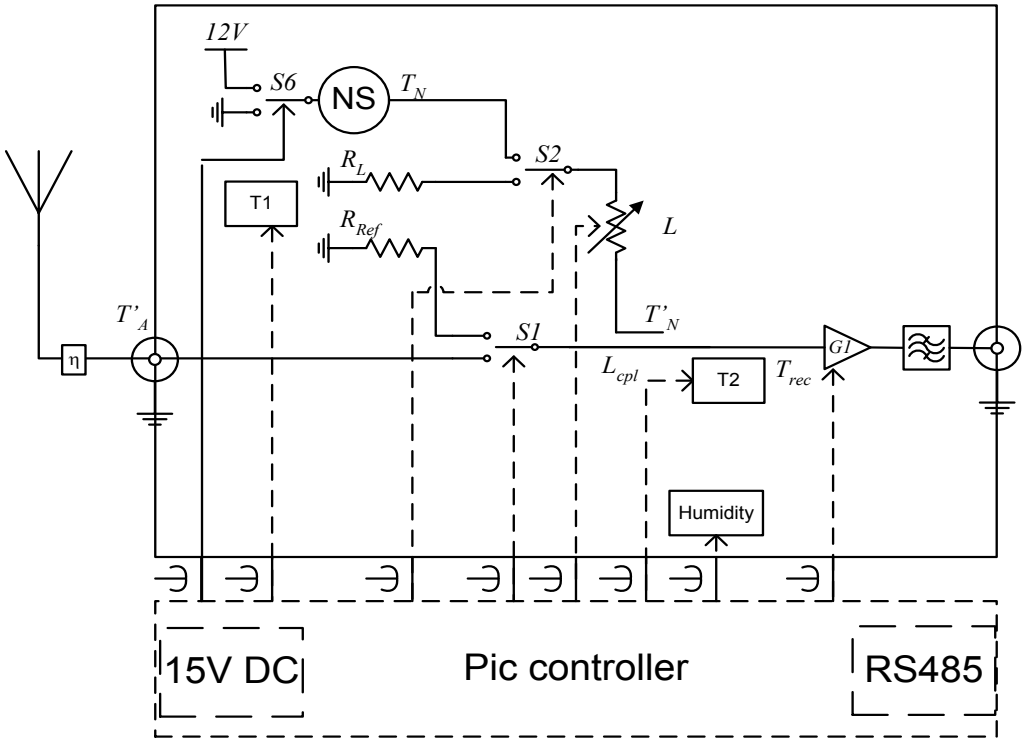

Figure 4-4 Block diagram of the single input radiometer in the front-end module

In addition, the internal noise source can be turned off by disabling its power supply regulator, S6, as depicted schematically in Figure 4-4. The regulator is placed underneath the board where the noise source mounted.

Two on-board temperature sensors, T1 and T2, measure the board temperatures. The temperature sensor, T1, measures the board temperature close to surface mount reference 50Ω load (R_{Ref}) and the internal noise source (NS) while T2 measures the board temperature close to the low noise amplifiers attached and heat-sinked to the board on the bottom.

The analog monitors (such as voltage and temperature monitors) and digital control lines (such as attenuator SPI control lines) on the RF board are routed to the microcontroller side via feed-through capacitors, and further filtered using RC networks on the controller side. In this way, any digital clock leakage (such as microcontroller 10 MHz reference clock) to the RF side within the band of 50 to 250 MHz could be isolated by more than 60dB.

Figure 4-5 shows the top view of the internal parts of one of the front-end modules when the RF board has been mounted in the enclosure and the amplifier EMI shield lids have been removed. The figure shows Ch1 on top and Ch2 on the bottom of the figure. However, in the current configuration, Ch2 power is disabled by default and is not used. Therefore, the RF input and output connectors for CH2 should be terminated by 50Ω connectorised loads during operation.

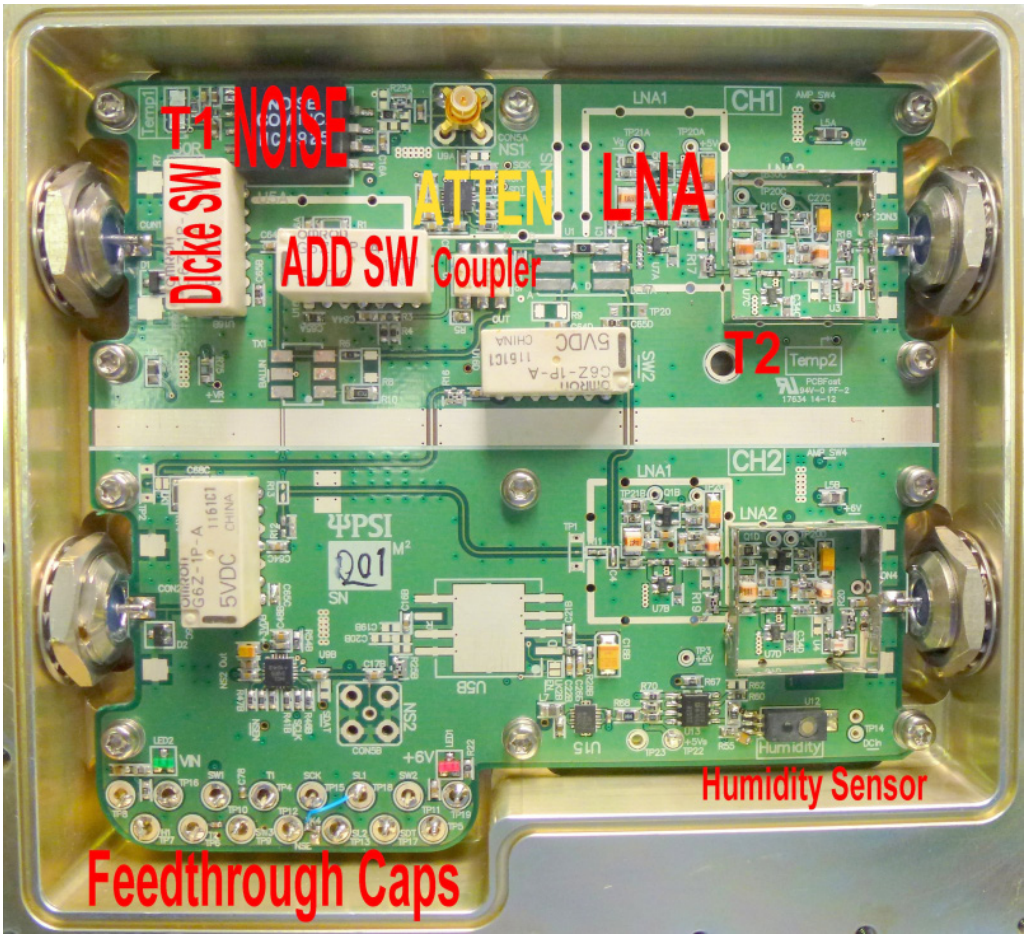

Figure 4-5 Photo of the front-end module RF board in enclosure

4.3.1 Front-end Configuration

The front-end board is a noise adding radiometer with the addition of a Dicke switch allowing up to four switching positions between S1 and S2, as shown in Table 3. The switches can toggle on and off independently at different rates. The switching rate is also software controlled remotely, from the back-end rack, allowing the receiver to operate under different modes, such as total power (TP), noise adding (NA), Dicke (D) radiometer or in a hybrid (H) mode. In the TP

mode, for instance, S1 will be on (i.e. connected) and S2 will be off (i.e. disconnected).

Table 3 The front-end four state switching combinations

S1	S2	Observable
ON (i.e. connected)	OFF	P_A
ON (i.e. connected)	ON (i.e. connected)	P_{AN}
OFF	OFF	P_{Ref}
OFF	ON (i.e. connected)	P_{Cal}

The S1 and S2 switches can be configured to provide four possible spectra as follows:

$$P_{Ref}(f) = \left(T'_{Ref} + T''_{Noff} + T_{Rec}\right)\kappa BG, \quad \text{Eq 4-1}$$

$$P_{Cal}(f) = \left(T'_{Ref} + T''_{Non} + T_{Rec}\right)\kappa BG, \quad \text{Eq 4-2}$$

$$P_A(f) = \left(T''_A + T''_{Noff} + T_{Rec}\right)\kappa BG, \quad \text{Eq 4-3}$$

$$P_{AN}(f) = (T''_A + T''_{Non} + T_{Rec})\kappa BG, \quad \text{Eq 4-4}$$

where $P_{Ref}(f)$ is the spectrum of the ambient reference load, $P_{Cal}(f)$ is the spectrum of the ambient reference plus calibrated noise source, $P_A(f)$ is the spectrum of the antenna, and $P_{AN}(f)$ is the spectrum of the antenna plus calibrated noise source. Solving for the antenna temperature, T''_A, using the results of the power ratios described in section 3.8.1, gives:

$$T''_A = T''_N \frac{\left(P_A - P_{Ref}\right)}{\left(P_{Cal} - P_{Ref}\right)} + T'_{Ref}. \quad \text{Eq 4-5}$$

And then from Eq 3-31, the effective antenna temperature at the input of the S1 switch, T'_A, can be determined as follows:

$$T'_A = L_1 T''_A + (1 - L_1)T_1, \quad \text{Eq 4-6}$$

where L_1 is the combined loss of the Dicke switch (S1) and the insertion loss of the coupler at a physical temperature, T_1.

4.3.2 Internal Noise Source

As discussed in section 3.8, ideally the radiometer accuracy will depend largely on the stability of its calibrated noise source and the receiver noise temperature. In this case, for a few mK resolution, the noise source should have:

i. An extremely flat frequency response between 50-250 MHz;
ii. A very low VSWR to reduce reflections;
iii. No gain deviations due to temperature variations.

In addition, in this experiment, the noise source had to be:

iv. Surface mount (SM) to fit in the receiver enclosure; and
v. Able to operate on a 12 V or lower battery supply.

For these reasons, it has been hard to find a highly accurate surface mount (SM) noise source with the above specifications for the front-end module in the frequency range of 50-250 MHz. It was decided to purchase a custom made noise source based on the specifications of a laboratory noise source unit. Other noise sources based on an input terminated RF amplifier can also be built and tested.

The laboratory calibrated noise sources, such as Agilent 346 series (Agilent Technologies, 2013), used for calibration purposes have only been calibrated at spot frequencies such as 10 MHz, 100 MHz, 1GHz at an ambient temperature of 23±1 C. The noise source excess noise ratio (ENR) uncertainty is also to within ±0.2 dB, and it has a typical temperature variation of 0.01 dB/ºC.

NoiseCom[1] was requested to provide a custom made SM noise source, having similar specification as Agilent 346 in terms of stability, but optimised for the 50-250 MHz frequency range as follows:

a) An ENR value of 36 dB (-138 dBm/Hz or 1,147,932 K);
b) Optimised flatness response between 50-250 MHz;
c) Run on supply voltage 12±0.2 V and less than 10 mA;
d) Temperature variations of 0.01 dB/ºC or better.

The SM noise source received was a NoiseCom NC4925 SM module. It was expected to have an internal attenuator for improved output VSWR, typical noise spectral density of -138 dBm/Hz @ 150 MHz and the output flatness of less than ±0.5 dB over the frequency range. During the tests it was found out that the noise sources delivered do not have any internal attenuators. Consequently, external

[1] http://noisecom.com/

attenuators in the noise adding radiometer arm (R25) may be used to improve the match.

Figure 4-6 shows the placement of the NC4925 noise source on the schematics of the RF board. The internal noise source in the noise adding radiometer arm is followed by a digital step attenuator (Mini Circuits DAT-31R5-SP) and a 10 dB directional coupler (Mini Circuits ADC104). The series combination would couple a maximum of -150 dBm/Hz (72,429 K) to the input of the LNA when the attenuator is set to 0dB.

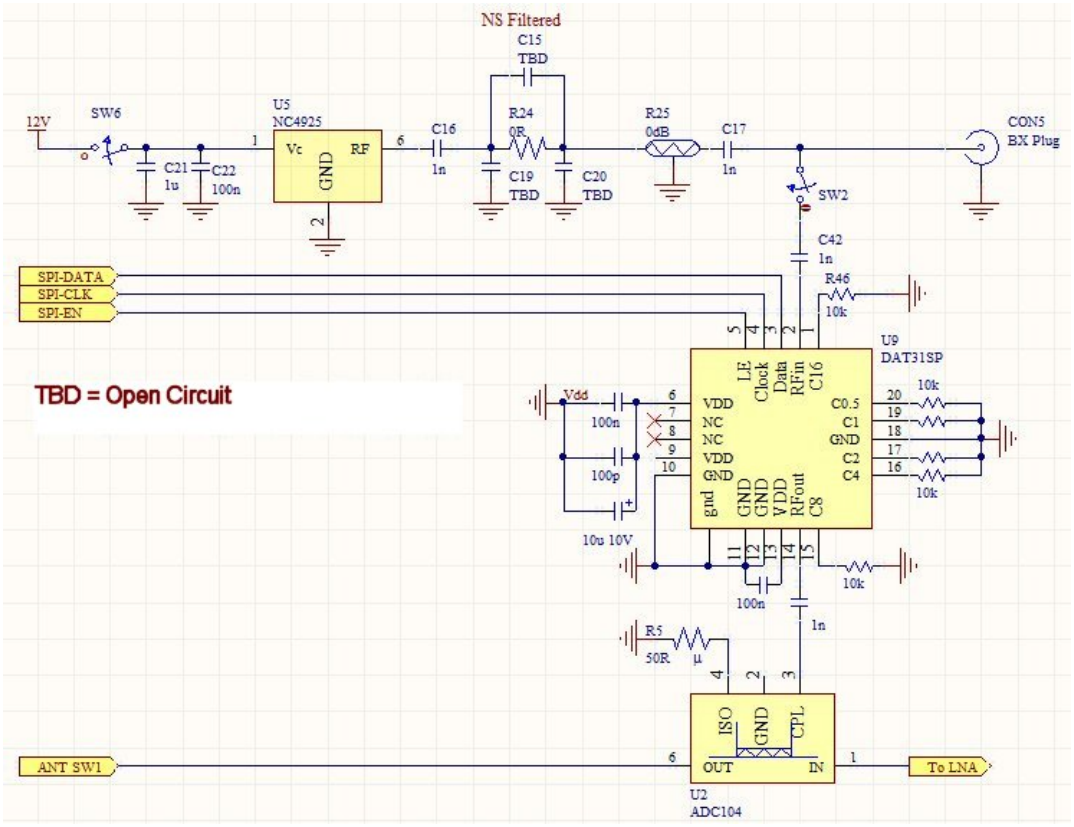

Figure 4-6 Noise adding section of the radiometer using NC4925 noise source

The S2 switch is used to either route the coupled input to the noise source or a 50 Ω terminator, R_{load}. However, the S6 switch is used to disable the dc regulator of the noise source therefore switching off the noise source.

4.3.3 Low Noise Figure Amplifier

The front-end radiometer design requires a moderate gain amplifier having a low noise figure, an unconditional stability, a high dynamic range to tolerate RFI, and highly matched input to reduce input reflections. Different types of amplifier prototypes have been simulated, designed and tested initially. The amplitude

flatness, temperature dependence and long term stability of the amplifiers were investigated.

Avago high linearity and high dynamic range GaAs E-PHEMT amplifiers, providing low noise figure, flat response and stable gain have been chosen for the receiver design. These have a high 1 dB compression point ensuring the receiver front-end stays in the linear operating range. Additionally, using Enhanced mode PHEMT amplifiers no negative biasing was required. To improve the temperature stability, the active bias circuitry was used to keep the amplifier quiescent bias point constant. Two-stage cascaded amplifiers have been implemented in the receiver front-end.

The output of the front-end coupler is connected to dual cascaded amplifiers (Avago ATF-54143) as shown in Figure 4-7. The dual cascaded amplifiers have a combined gain of 40 dB. The amplifiers have been designed and tested to have a high input and output VSWR, low noise figure and high reverse isolation over the frequency range of 50-250 MHz.

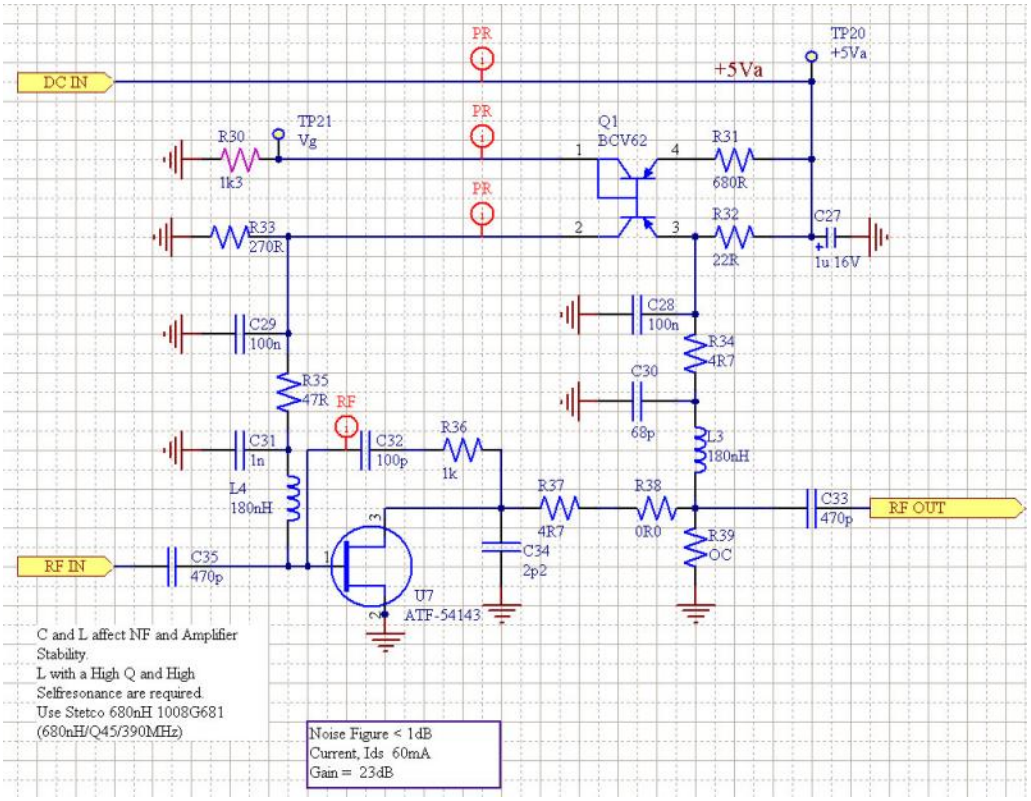

Figure 4-7 Schematics of one of the low noise amplifier stage

The cascaded amplifiers have been tuned to provide a noise temperature of less than 100 K over the bandwidth, especially at the higher end of the band where the

sky noise is expected to be of the same order. At the lower end of the band (<100 MHz) where the 21 cm global signal is expected to appear in absorption with the deepest EoR signature, the sky noise is expected to be greater than 800 K (see Figure 2-9). The amplifier noise in this frequency region is not of major concern.

The amplifier design uses an RC feedback network across the transistor to increase the stability factor and provide a broadband match across the bandwidth between the two stages. The amplifier also uses a highpass impedance matching network at its input to match to the internal directional coupler output. The built-in highpass filter acts as impedance matching as well as to reduce undesirable signals in the HF band (HF radios and high power repeaters in 80 to 10 metre band) below 50 MHz. The amplifier feedback components and source capacitor and inductor values have been manually tuned for each receiver module to achieve the lowest ($\sim 20dB, \rho = 0.1$) return loss across the band and to have smooth highpass roll off characteristics.

The 5V DC bias lines for the cascaded amplifiers in each chain are connected to a linear low voltage noise regulator (linear Technology LT1763) to reduce any cross-coupling and conductive feedback between the two chains. The regulators have been placed close to the amplifiers on the PCB bottom layer.

An active DC biasing network is used to provide a means of keeping a stable quiescent bias point for the amplifier over temperature. A Mini-circuits 7^{th} order filter is used at the output to reduce the noise power beyond 400 MHz. This helps prevent it from saturating the amplifiers in the next stage.

The second amplifier stage has also been shielded in an RFI can soldered directly to the PCB, as shown in Figure 4-5, to reduce radiated coupling between the two stages in each chain.

Heat sink blocks have been placed and glued to the bottom layer of the PCB underneath the amplifiers to conduct the heat generated on the board directly to the chassis. A surface mounted temperature sensor (LM35) close to the amplifier also monitors the board temperature.

4.3.4 RF Switches

The RF switches chosen for the front-end housing were surface mount 50Ω high frequency latching relays (Omron G6Z-1PE), having an excellent return loss of > 40dB, an insertion loss of < 0.2 dB and > 60dB of isolation at frequencies below 500 MHz. The relays have operating set and reset time under 10ms which makes them suitable for high speed Dicke switching rate in the radiometer.

Figure 4-8 shows the isolation response of the S1 relay switch measured using a network analyser between the front-end input port and the output of the coupler when the switch was terminated to the internal reference.

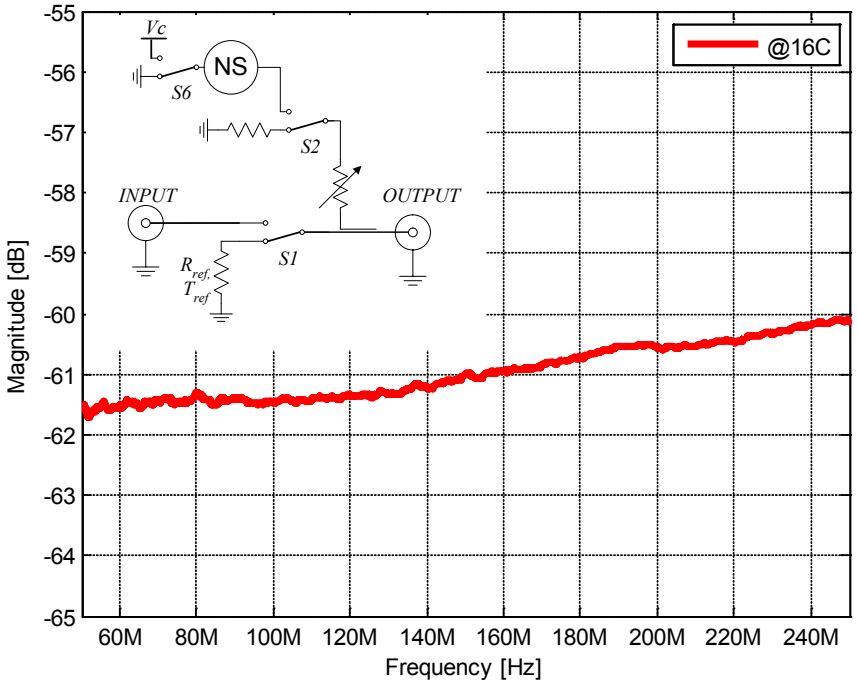

Figure 4-8 G6Z-1PE relay (S1) isolation as measured in the front-end module

For a 60 dB isolation in the switch, and a -137 dBm/Hz (or 1,445,149 K) noise source, this would add −197 dBm/Hz (1.4 K) during the S2 off state to the 50Ohm load. When the load is at 310 K, this translates to a 4 mK rise. As a result, 60 dB of isolation should be sufficient for the purpose of the experiment. However, if it is necessary to remove this excess rise in temperature, the microcontroller can also disable the regulator powering up the noise source, in conjunction with S2 RF relay. This is achieved by controlling the disable/enable pin (S6) on the regulator.

4.4 Power Control and RF Cables

The RF cable is expected to run for 100 m between the front-end module attached to the antenna and the gain module in the shielded back-end rack. As the cable is expected to be lying on the ground for days during field tests, cable ruggedness, temperature stability, loss factor and shielding effectiveness were the main criteria in cable selection. A low loss foamed polyethylene (PE) dielectric RF cable was chosen for this reason. The foam PE dielectric cable has a low loss and has an excellent typical electrical length (or phase) stability with temperature of about 25ppm/ºC. The RF cable is 100 m of Huber Suhner double shielded SPUMA-400 with a typical return loss better than 28 dB below 500 MHz. Based on the Huber Suhner datasheet, typical cable attenuation per metre can be calculated as follows:

$$A = 0.1241\sqrt{f_{GHz}} + 0.008 f_{GHz} \, . \qquad \textbf{Eq 4-7}$$

A metre of this RF cable at 250 MHz would have a typical insertion loss of 0.065 dB.

The front-end and gain module also requires a minimum of 14 V to 18 V DC input and a RS485 interface. RS485 differential signalling is used between the receiver modules and the MCU in the back-end rack. A 100 m length of double shielded Beldon 3082A pairs was obtained for this purpose. This cable has two individually foil shielded 15 and 18 AWG pairs as well as an overall tinned copper braid for improved shielding effectiveness. The 18 AWG pair, having a characteristic impedance of 120 Ω, is used for RS485 signalling and 15AWG is used for DC input power.

4.5 Gain Module Architecture

The block diagram of the gain module is shown in Figure 4-9. There are two amplifier chains, CH1 & CH2, in the gain module. The CH2 chain is turned off at start up by the microcontroller. Each chain consists of three stage cascaded amplifiers followed by a digital step attenuator (Mini Circuits DAT31R5) to adjust the output level to the digital backend data acquisition input. The first and

second stage amplifiers chosen are GaAs E-PHEMT amplifiers with low noise figures similar to the front-end module (Avago ATF-54143). To boost the gain further, an optional third stage has also been designed and added using a high dynamic range, high IP3 GaAs HBT amplifier (Triquint AH118). This ensures that this high gain module will still operate in linear mode, and will not saturate at the maximum output level of -10 dBm required for the data acquisition input.

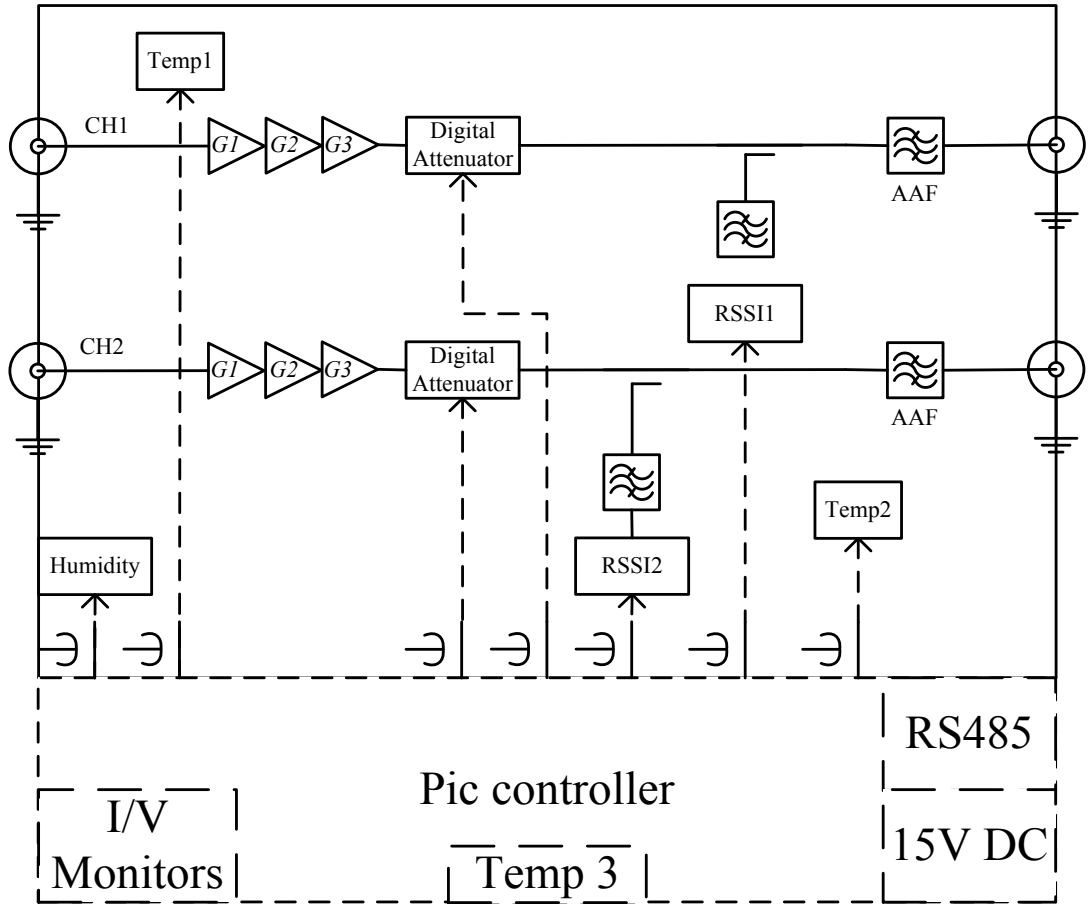

Figure 4-9 Dual channel gain module block diagram

A digitally controlled step attenuator follows the amplifiers. The digital attenuator has a 6-bit serial control interface and an attenuation range up to 31.5 dB in 0.5 dB steps with a typical accuracy of ±0.1 dB as well as a high input IP3 of greater than +50 dBm. Part of the power at the attenuator output couples to an integrated rms power detector for RF input power measurements.

A high roll-off anti-alias lowpass filter with a flat frequency response has been simulated, designed and tested for the output of the gain module. The output of the gain module connects using a short piece of RF cable to the digitiser unit

(DAQ) in the back-end rack. The filter has been designed using lumped elements and manually tuned for sharp roll off and low output VSWR.

4.5.1 Radiometer Detector

A directional coupler at the output couples part of the input signal to an integrated and temperature compensated rms power detector chip (Hittite HMC1020). The monolithic detector is an industrial grade integrated chip consisting of a full-wave rectifier, log circuitry and an integrator which incorporates temperature compensation circuitry to provide an accurate analog output over its full temperature range. It also includes active DC offset cancellation circuitry to cancel internal DC offsets. Its output is directly proportional to the logarithm of the time average of the input signal:

$$RMS_{out}(mV) = \frac{1}{a} * log(\int V_{in}^2 dt), \quad \text{Eq 4-8}$$

where a is the conversion factor of the detector in mV/dB. The analog output voltage of the detector, which is proportional to the logarithm of the time average of V_{in}^2, is read by the microcontroller ADC input. Once calibrated with an accurate signal source, the detector provides an accurate rms power of the RF input signal, having a 38mV/dB logarithmic slope, and an integration time constant of approximately 10ms set by external resistors on the PCB. Subsequently, the input power can be determined based on the values of output voltages read from the ADC as follows:

$$P_{in}(dBm) = \frac{RMS_{out}}{slope} + intercept\ (dBm), \quad \text{Eq 4-9}$$

where intercept has been calculated during the detector calibration based on a known input power.

The detector is used later on for radiometer internal calibration and to measure the stability of the radiometer.

4.5.2 Anti-alias Filter

An anti-alias bandpass filter using passive components has also been incorporated at the output of the gain module. The filter consists of a number of carefully chosen series and parallel resonant circuits combined to create a flat bandpass response as well as a sharp roll off providing a better than 50dB rejection for

frequencies above 500 MHz. The filter has also been manually tuned to provide a good output match to the digitiser unit in the back-end rack.

4.6 Controller Architecture

The controller board consists of a 32-bit PIC microcontroller (Microchip PIC32MX460F512L), an isolated RS485 transceiver (Analog Devices ADM2587), low noise voltage regulators under the board, a precision centigrade temperature sensor (TI LM35), high grade current sensors (TI INA219) and voltage monitors as shown in Figure 4-10.

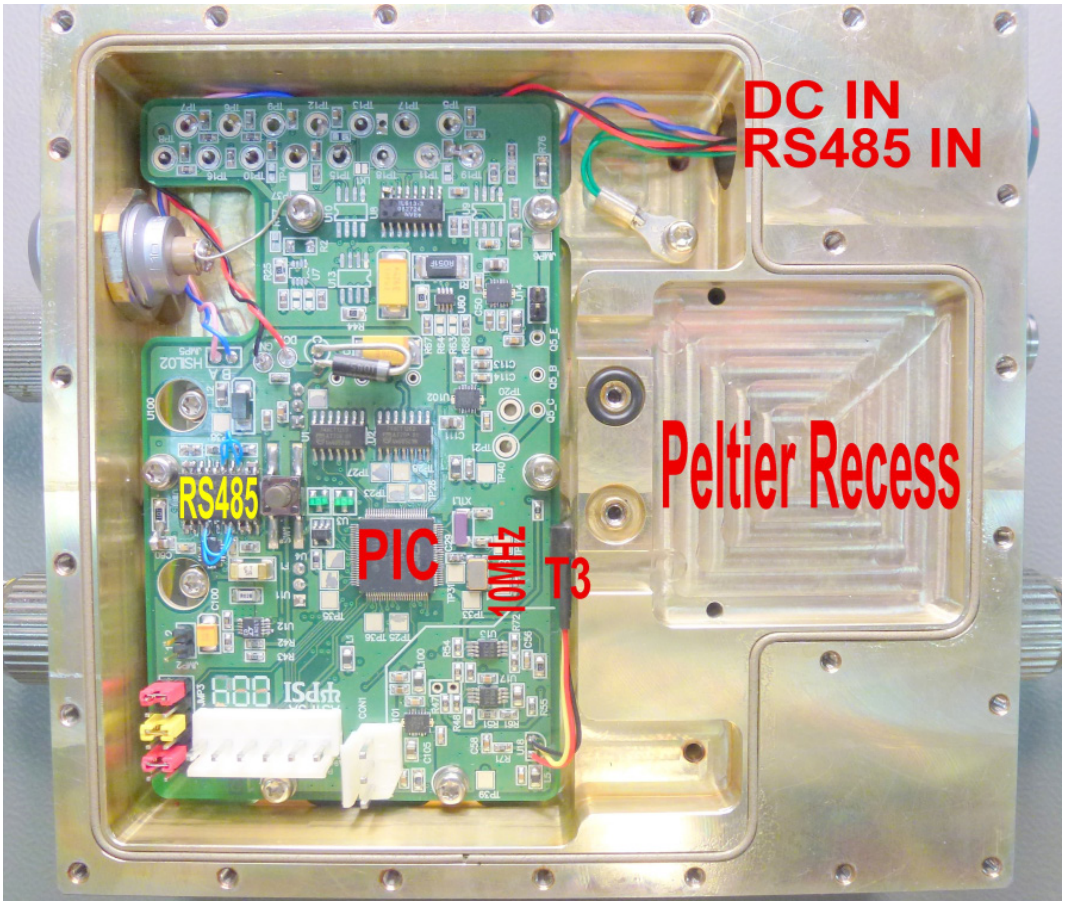

Figure 4-10 Controller side of the receiver module (MST-0512-SN5)

The microcontroller runs on a precision 10 MHz reference clock (IQD TCXO CFPT-9301) and is programmed to start up as soon as the receiver module is powered up. When requested through RS485 command it can provide the detailed status of the modules such as status of switches, attenuator levels, power detector outputs, voltage, current, and temperature monitors. These can be used for diagnostic purposes. Using the rms power detector output, the input noise

temperature level can be measured to indicate if high RFI signals (20 or 30dB above the measurement noise floor) are present in the band.

The microcontroller is connected to an isolated RS485 transceiver having an integrated dc-dc converter, and is programmed to sit idle unless it receives commands from the external master controller unit from the back-end rack. The RS485 transceiver is a fully integrated single chip featuring both isolation of the signal and power lines. It runs on a dedicated 3.3V regulator on the MC board and can be turned off by sending M019 commands to the microcontroller remotely.

The front-end and gain modules have different address lines to differentiate them from each other. The front-end commands start with address 1 and gain module commands with address 2.

4.6.1 Software Monitoring

The microcontroller communicates with the outside world through the RS485 transceiver on-board as shown in Figure 4-11. RS485 signalling with a host computer in the MCU is at a fixed 38400 baud rate. Data coming from the MCU will be transmitted to both modules. However, the module with the correct address (address 1 for the front-end and 2 for the gain module) will respond.

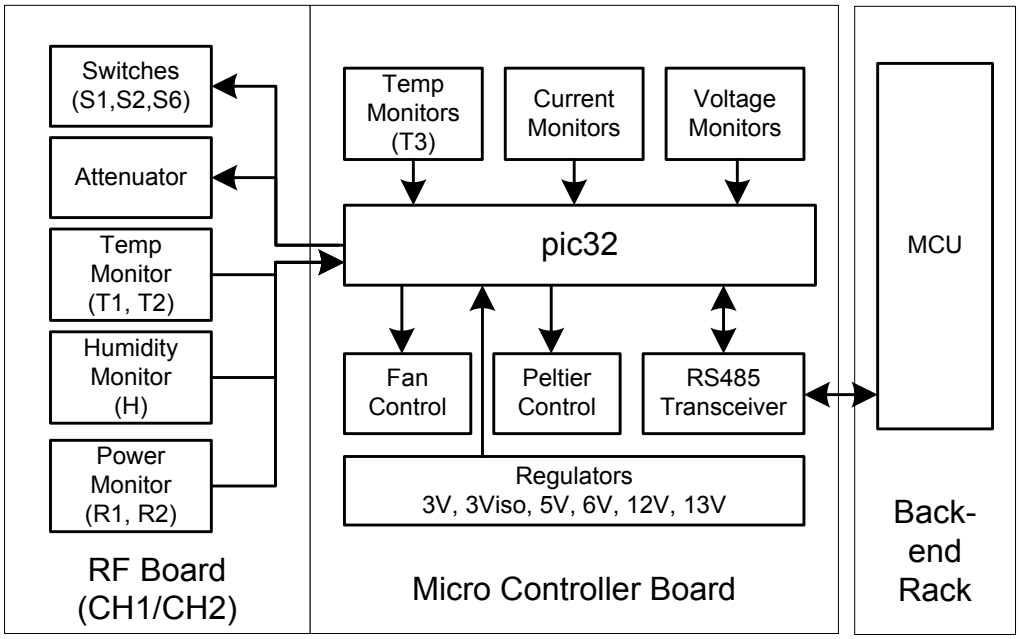

Figure 4-11 Microcontroller inter-connections with peripherals and back-end rack

The MCU in the digital back-end rack can, at any time, request access to various parameters of the receiver modules (such as state of the switches as well as

voltages, temperatures) to determine the status of the radiometer. The MCU can also control the states of the radiometer switches and noise adjusting attenuators in the front-end module as well as the attenuators in the gain module.

Temperature monitoring is accomplished using the LM35 integrated circuit which is calibrated directly in degree Celsius, and has a linear scale factor of +10.0 mV/°C and 0.5°C accuracy at +25°C. The chip is wafer-level trimmed for high accuracy and is rated for full −55° to +150°C range with low self-heating.

The regulated analog voltages, current sensors, and the two temperature sensor voltages (T1 and T2) from the RF board are connected to 10-bit ADC ports of the microcontroller for monitoring.

The analog filtered outputs of the detectors (in CH1 and CH2) are also routed to the microcontroller 10-bit ADC inputs and can be monitored by the software monitoring program. The rms power detectors (R1 and R2), are used to measure the true rms of the input power levels. When used as a Dicke Mode (DM) radiometer, the detector can be calibrated to measure and estimate the average input noise temperature over the receiver passband.

The controller code is a C-code program written under Microsoft Windows in MPLABX (Rev 1) and the PIC microcontroller is programmed using ICD3 programmer. The table of commands has been tabulated in Appendix E. When a status command such as 1002 is sent to the front-end or gain microcontroller, it responds with the status (in hexadecimal) of all receiver parameters such as temperatures, voltages and currents, attenuator settings, switch states, and so on.

A LabVIEW software program (Appendix D) in the Microsoft Windows operating environment has been written to monitor and control the receiver modules using RS485 differential signalling. It has been used to program the micocontroller to set the status of the front-end switches at known intervals so the receiver can operate in different modes; noise adding radiometer (NAR); total power radiometer (TPR); or noise adding comparison radiometer (NACR). The status of the receiver modules can be saved at multiples of 1sec interval.

Figure 4-12 shows a screenshot of the monitor/controller program. Having measured the insertion losses of the radiometer parameters in situ, using a known

source attached to the antenna input, the controller program is employed to calibrate the internal noise source temperature against the known noise source.

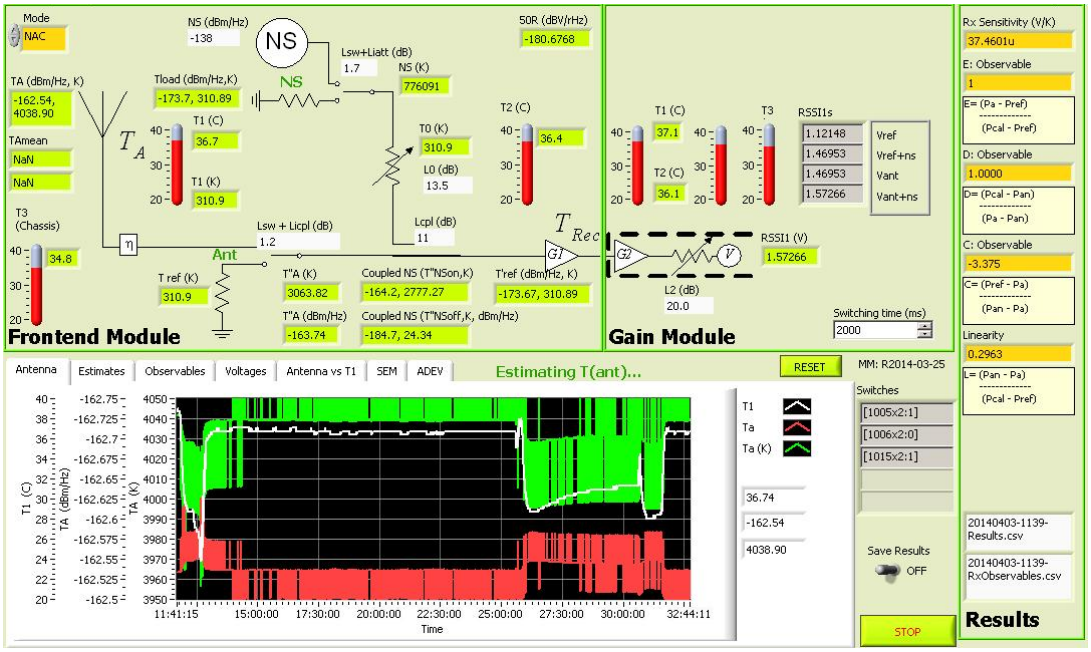

Figure 4-12 Controller program used for radiometer internal calibration

4.7 Radiometer Internal Calibration

In order to measure the receiver functionality and calibrate radiometer measurement uncertainties in the laboratory, the rms power detector on-board the gain module has been utilised. As the detector is temperature compensated with active DC offset cancellation, its output voltage can be used to initiate a first pass calibration and to estimate its sensitivity. Based on the 200MHz wideband input of the detector and its approximate 10ms integration time constant, the radiometer internal references can also be calibrated down to a few Kelvin. The detector output rms voltage has been tuned by external resistive networks for a conversion factor of 38 mV/dB and a better than 55 dB dynamic range over the band as shown in Figure 4-13. The analog detector output voltage is routed to the microcontroller ADC input having a 10-bit resolution (or 3 mV). This provides the absolute measurement resolution of approximately ±0.1 dB over its 55 dB range.

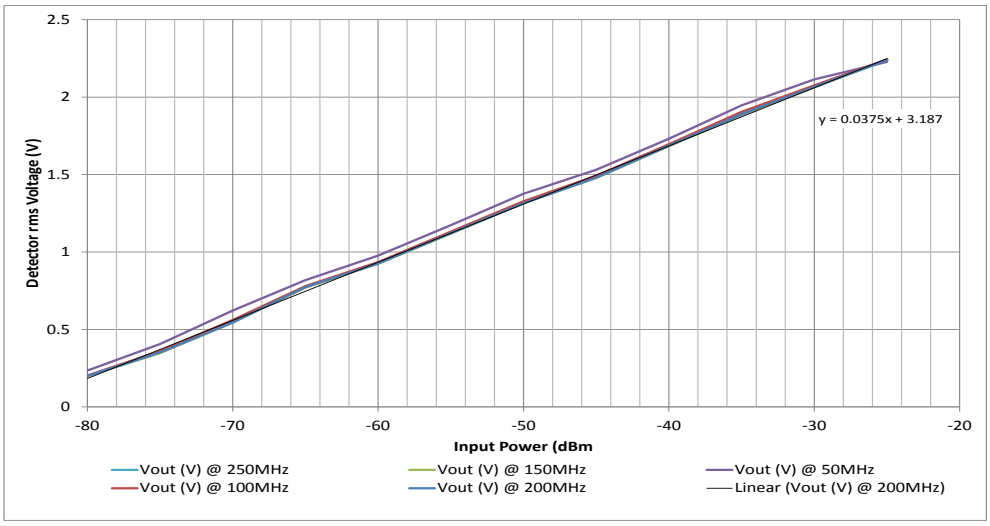

Figure 4-13 Detector Calibration

Now, if the front-end and the gain modules are connected back to back, and a calibrated load is connected to the antenna input, the detector output voltages read by the microcontroller can be used to estimate the internal noise source temperature, T_N, knowing the calibrated load temperature as discussed below. The measurement setup is shown in Figure 4-14.

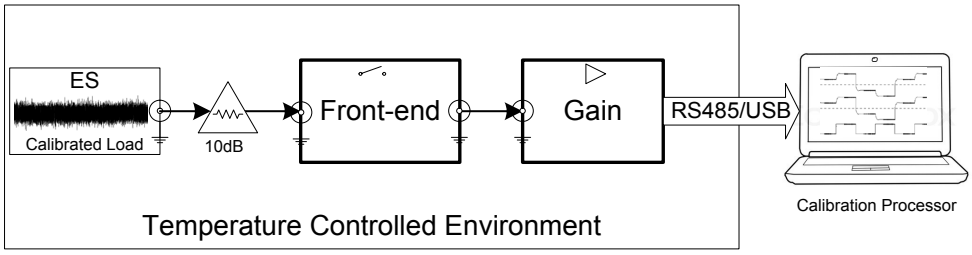

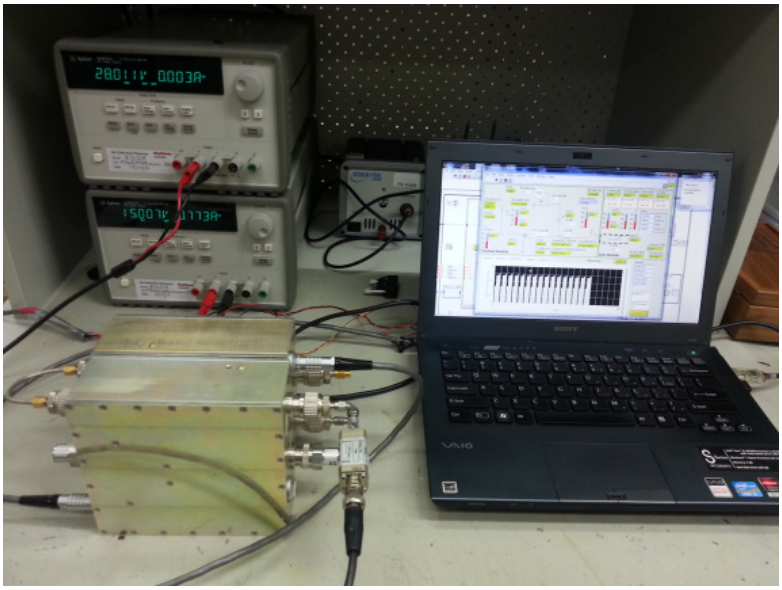

Figure 4-14 The Radiometer internal calibration configuration in the laboratory

For the purposes of calibration, a LabVIEW program has been written in the host computer using RS485 protocol to communicate with the microcontrollers in the front-end and gain modules, both to monitor and control the radiometer components. When the two S1 and S2 RF relay switches are toggled, there are four possible states related to each switch position.

In this case, the four detector output voltages in the gain module can be defined as follows:

$$V_{Ref} = \left(T'_{Ref} + T''_{Noff} + T_{Rec}\right)G\,, \quad \textbf{Eq 4-10}$$

$$V_{Cal} = \left(T'_{Ref} + T''_{Non} + T_{Rec}\right)G\,, \quad \textbf{Eq 4-11}$$

$$V_A = \left(T''_A + T''_{Noff} + T_{Rec}\right)G\,, \quad \textbf{Eq 4-12}$$

$$V_{AN} = \left(T''_A + T''_{Non} + T_{Rec}\right)G\,, \quad \textbf{Eq 4-13}$$

where $V_{Ref}, V_{Cal}, V_A, V_{AN}$ are the voltages measured by the detector for each state. In this case, G is the receiver total gain in V/K unit, and $T'_{Ref}, T_{Rec}, T''_A, T''_{Non}, T''_{Noff}$, are the ambient reference temperature, the receiver noise temperature, the antenna noise temperature, the calibrated noise source temperature, and the reference load temperature at the output of the coupler, respectively, as shown in Figure 4-15. The gain, G, in the equations above incorporates the detector sensitivity and the combined gain of amplifiers in the front-end and gain module over the integrated bandwidth.

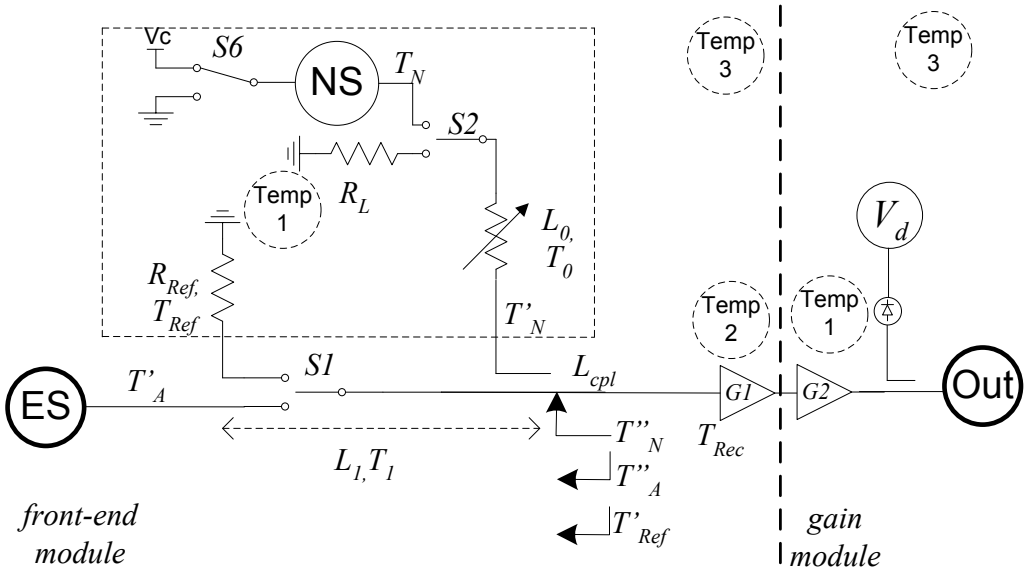

Figure 4-15 Radiometer internal calibration parameters

Using Eq 4-10 and Eq 4-11, the radiometer gain can also be estimated in each switching sequence according to:

$$G = \frac{V_{Cal} - V_{Ref}}{\left(T"_{Non} - T"_{Noff}\right)} \qquad (V/K), \qquad \textbf{Eq 4-14}$$

To estimate the calibrated load temperature connected to the input, the following voltage ratio, E, similar to the power ratio in section 3.8.1, can be calculated using the three states of the radiometer:

$$E = \frac{V_A - V_{Ref}}{V_{Cal} - V_{Ref}}. \qquad \textbf{Eq 4-15}$$

Substituting temperature terms for V_A , V_{Ref}, and V_{Cal} into Eq 4-15, the antenna noise temperature at the input to the amplifier, $T"_A$, can be estimated from:

$$T"_A = T'_{Ref} + E(T"_{Cal}), \qquad \textbf{Eq 4-16}$$

where $T"_{Cal} = \left(T"_{Non} - T"_{Noff}\right)$.

From Eq 4-16 and Eq 4-6, the measured antenna noise temperature, T'_A, at the input of the front-end module, can be found as follows:

$$T'_A = L_1\left(T'_{Ref} - T_1 + E\ T"_{Cal}\right) + T_1. \qquad \textbf{Eq 4-17}$$

From Eq 3-42, the reference noise temperature at the LNA input, T'_{Ref} , can be written in terms of the input loss (measured from the input of the S1 switch to the input of the amplifier including the insertion loss of the coupler), L_1 , and its physical temperature, T_1 , as follows:

$$T'_{Ref} = \frac{T_{Ref}}{L_1} + T_1\left(1 - \frac{1}{L_1}\right). \qquad \textbf{Eq 4-18}$$

Inserting this into Eq 4-17 gives:

$$T'_A = T_{Ref} + L_1 E\ T"_{Cal}\ . \qquad \textbf{Eq 4-19}$$

Similarly from Eq 3-43, the calibrated temperature at the LNA input, $T"_{cal}$, can be written in terms of the attenuator loss (measured from the input of the S2 switch to the input of the coupler), L_0 , the coupler coupled loss, L_{cpl} , and reference load temperature, T_L , as follows:

$$T"_{Cal} = \frac{1}{L_{cpl}}\frac{1}{L_0}(T_N - T_L). \qquad \textbf{Eq 4-20}$$

Inserting this into Eq 4-19 gives the antenna temperature with respect to the individual radiometer components:

$$T'_A = T_{Ref} + \left\{\frac{1}{L_{cpl}}\frac{1}{L_0}L_1\right\}ET_{Cal}, \qquad \textbf{Eq 4-21}$$

where $T_{Cal} = (T_N - T_L)$ is the difference between the noise source temperature, T_N, when the noise source is on, and the reference load noise temperature, T_L, when the noise source is off . During the internal calibration the antenna temperature, T'_A, is known and the noise temperature of the noise source, T_N, can be solved from Eq 4-21.

Eq 4-21 is an important equation for the hybrid radiometer. It can be used to estimate the input antenna temperature based on the known values of input losses, measured detector voltage ratio and reference sources.

Eq 4-21 indicates that, firstly, the change in antenna temperature is directly proportional to the change in the reference noise temperature, ΔT_{Ref} :

$$\Delta T'_A \propto (\Delta T_{Ref}). \qquad \textbf{Eq 4-22}$$

Secondly, the change in antenna temperature is proportional to the internal noise source temperature variations and the measured loss and voltage parameters as follows:

$$\Delta T'_A \propto \left\{\frac{1}{L_{cpl}}\frac{1}{L_0}L_1\right\}E(\Delta T_{Cal}). \qquad \textbf{Eq 4-23}$$

Since the antenna temperature, T'_A, is measured using the same values for input losses, $\frac{1}{L_{cpl}}\frac{1}{L_0}L_1$, with which the internal noise source temperature, T_{Cal} , is also measured, the systematic uncertainty in their determination does not contribute significantly to the overall uncertainty, as long as they stay constant during the four switching states. Similarly, it is fair to say that the detector temperature does change appreciably so voltage measurements are consistent.

4.8 Estimating Radiometer Sensitivity

If the first three detector output voltages (Eq 4-10, Eq 4-11, Eq 4-12) are used to calculate the ratio E, the radiometer resolution, assuming equal integration times, can be derived as the rms sum of the noise temperature terms in each radiometer

state (7.1 Appendix A). The resolution of the radiometer in this case can be written as:

$$\Delta T_{rms} = \sqrt{\frac{1}{B(\tau/3)}}\sqrt{(T''_A + T_{Rec})^2} + \sqrt{\frac{1}{B\tau/3}}\sqrt{\left(T''_A - T'_{Ref}\right)^2\left(1 + \frac{T'_{Ref} + T_{Rec}}{T''_N}\right)^2} + \sqrt{\frac{1}{B\tau/3}}\sqrt{\left(T'_{Ref} + T_{Rec}\right)^2\left(\frac{T''_A - T'_{Ref}}{T''_N} - 1\right)^2}, \quad \textbf{Eq 4-24}$$

where T''_A, T'_{Ref} and T''_N are noise temperatures measured at the input of the amplifier as defined in section 3.8.1 as follows:

$$T''_A = \frac{T'_A}{L_1} + T_1\left(1 - \frac{1}{L_1}\right), \quad \textbf{Eq 4-25}$$

$$T'_{Ref} = \frac{T_{Ref}}{L_1} + T_1\left(1 - \frac{1}{L_1}\right), \quad \textbf{Eq 4-26}$$

$$T''_N = \frac{1}{L_{cpl}}\left\{\frac{T_N}{L_0} + T_0\left(1 - \frac{1}{L_0}\right)\right\}. \quad \textbf{Eq 4-27}$$

Based on the radiometer parameters measured, when the receiver temperature is $T_{Rec} = 90\ K, T'_{Ref} = 300\ K$, $T''_N = 5000, B = 100\ kHz$, integration time is $\tau = 2\ hrs$, and equal time spent in each switching state, the radiometer resolution should be reduced to approximately ΔT_{rms}~$50\ mK$ at $T''_A = 300K$.

Figure 4-16 shows the difference between the resolution of a NAC and an ideal radiometer as antenna noise temperature changes from 0K to 6000K.

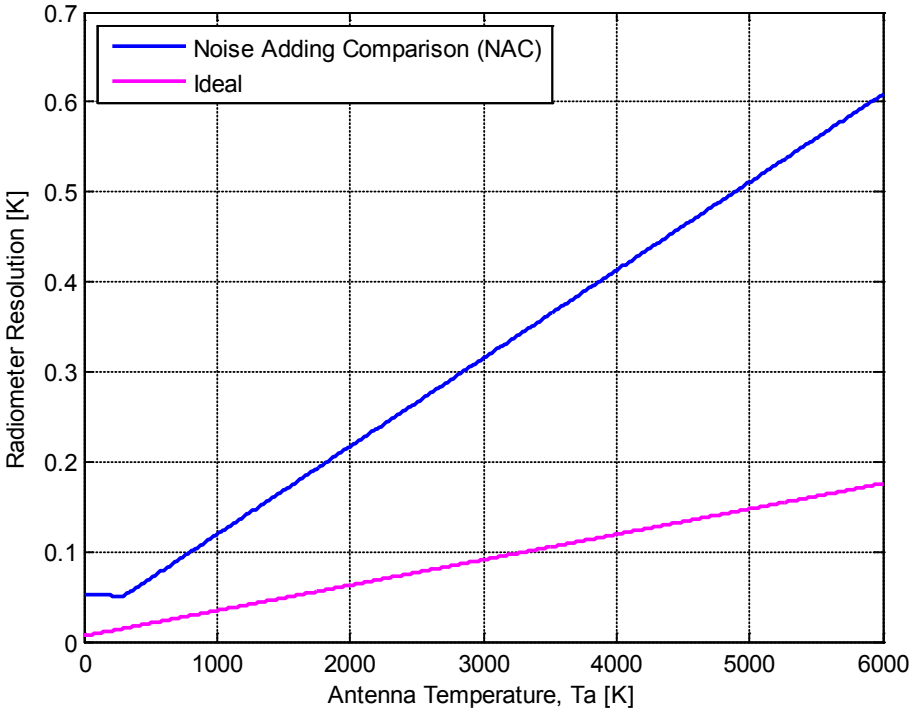

Figure 4-16 NAC radiometer resolution for BW=100 kHz and τ=2 hrs

CHAPTER 5

5 Radiometric Receiver Performance

In this chapter the measured performance of the radiometric receiver will be presented. The receiver performance has been carefully evaluated over the temperature range of 10 ºC to 50 ºC and the frequency range of 50 MHz to 250 MHz and the individual radiometer subsystems have been characterised. These characteristics can be used for the complete end to end calibration of the BIGHORNS system.

The vector network analysers (VNAs), R&S ZVB-20 with automatic calibration unit (ZV-Z52), and Agilent N5241 PNA-X with 346 noise source unit, have been utilised to measure various component characteristics such as frequency responses, amplifier compression points and noise temperatures of various devices. A full two-port calibration (both VNAs have vector error correction capability), at the required input power level to the device under test, has been performed over the frequency range of interest prior to measurements.

In addition, the spectrum analysers, Agilent E4407B and N9344C, have been used in the laboratory to measure and analyse the spectral contents of individual RF sections from 10 MHz to 1GHz. Unfortunately, the high resolution Agilent E4407B spectrum analyser had a malfunction and ceased to work. As a result, some of the subsequent measurements were carried out using the portable N9344C analyser.

Other data such as temperature, voltage and current in the receiver modules have also been captured from the microcontrollers in the receiver modules and saved for later access and analysis.

To reduce systematic errors, prudent RF measurement practices have been followed, such as allowing the instrument to achieve thermal equilibrium, using high-quality cables and connectors, selecting a small IF bandwidth as well as trace averaging. In some cases, averaging factors of > 2000 taking as long as 20 hours or so, have been used to reduce uncertainties in the measurements. Furthermore, the measurements described in this chapter, have been carried out in an air-conditioned laboratory environment to reduce the instrument thermal effects.

5.1 Receiver RF Characterisation

The front-end and gain module RF characteristics are now presented. Also included here are the RF characteristics of the 100 m cable to be used between the front-end and the gain module, and the system noise temperature of their combination, comprising the front-end module, cable and the gain module.

5.1.1 Front-end Module Characteristics

The channel 1 front-end module response over the frequency band has been measured on the VNA with the input switch (S1) enabled and the internal noise source turned off. The measurements have been made on the Rohde & Schwarz VNA, following the two-port calibration, at -40 dBm input using 16001 spectral points and more than 100 averages.

Figure 5-1 shows the s-parameter frequency response, S21, between the input and output N-type connectors, including the front-end input loss, having an average gain of approximately 36.4 d over the 200 MHz bandwidth.

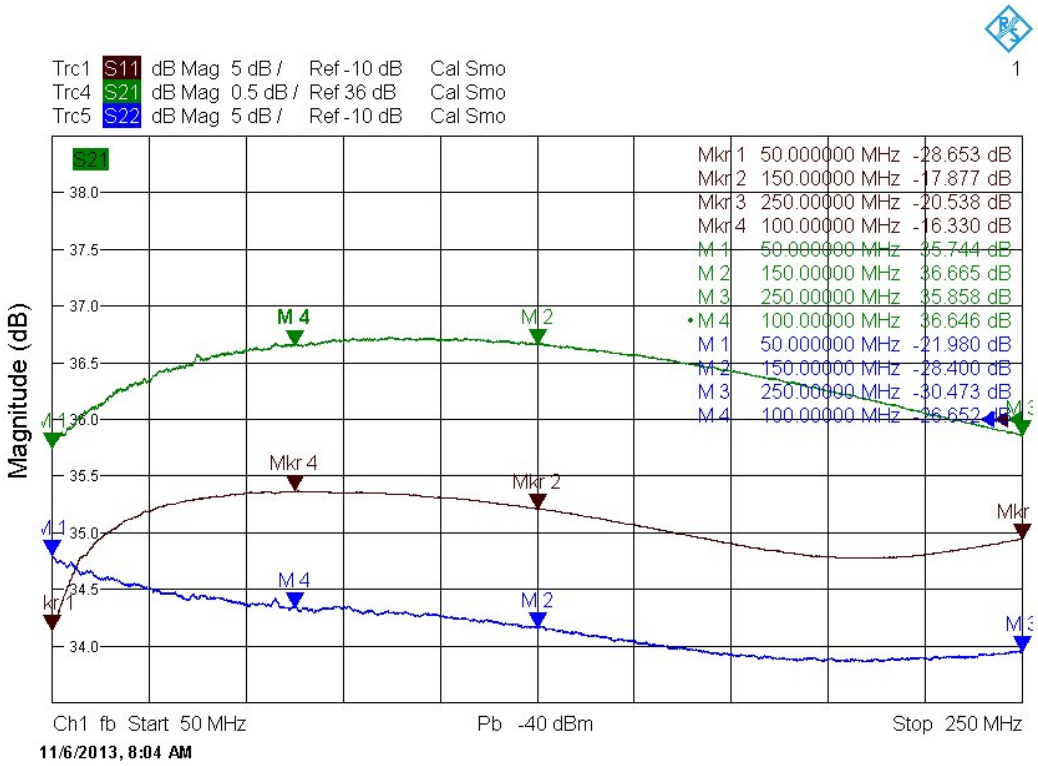

Figure 5-1 Frequency response of the front-end module (MST-0512-SN2)

The input and output return loss parameters, (S11 and S22) have also been represented in the plot but their y-axes have been scaled with an offset (shown on

top of the plot) so they can be displayed on the same plot. The input and output return losses are better than 16.3 dB (Γ=0.15). The level markers on the graphs display the S-parameter values at 50 MHz, 100 MHz, 150 MHz and 250 MHz.

Next, the Agilent PNA-X network analyser has been calibrated and used to measure the noise temperature of the front-end module as shown in Figure 5-2. The module (assembly serial number, MST-0512-SN2) has been optimised for noise temperatures below 220 K (noise figure of 2.4dB), including input losses (S1 switch and directional coupler). The level markers on the plot display the noise temperature values at 50 MHz, 150 MHz and 250 MHz. The y-scale unit has been converted to Kelvin and is in 0.1 kK (or 100 K) per division as set up by network analyser.

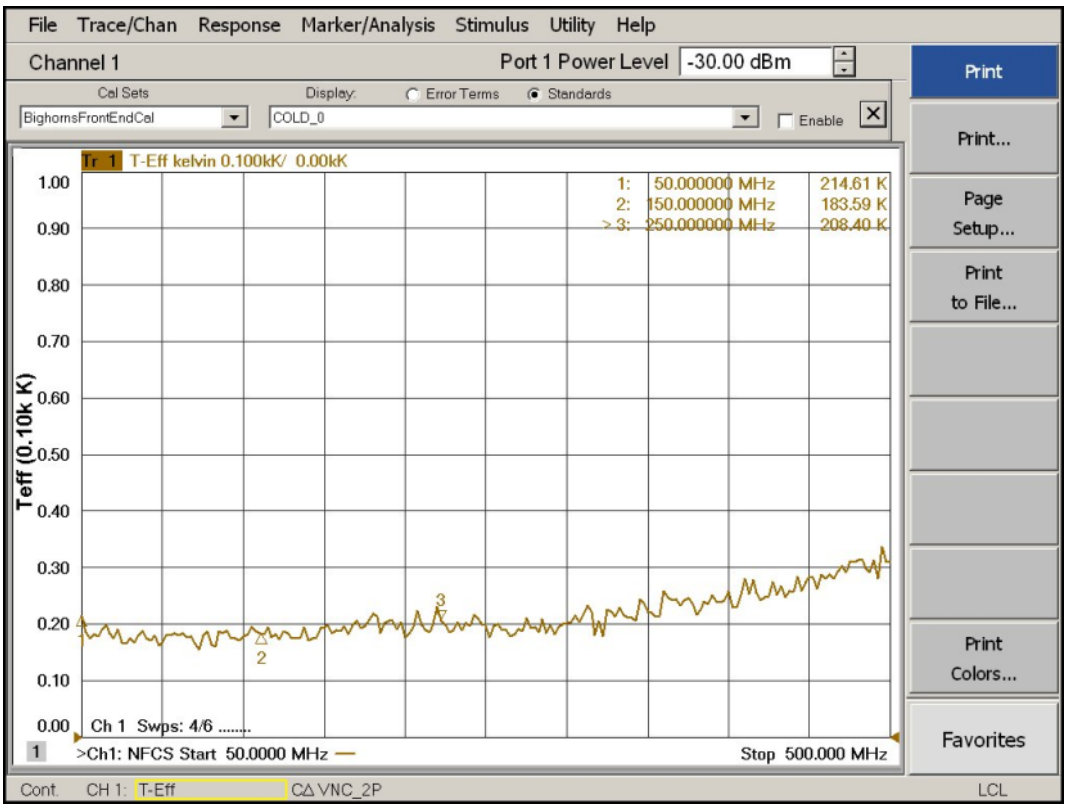

Figure 5-2 The noise temperature plot of the front-end module (MST-0512-SN2)

The front-end output spectrum has also been measured for different settings of the attenuator in the noise adding arm. In this case, the front-end input was terminated with a precision 50 Ω load and the internal noise source had been switched on. Figure 5-3 shows the output spectra when the attenuation setting was set to 1, 2, 3 and 20 dB.

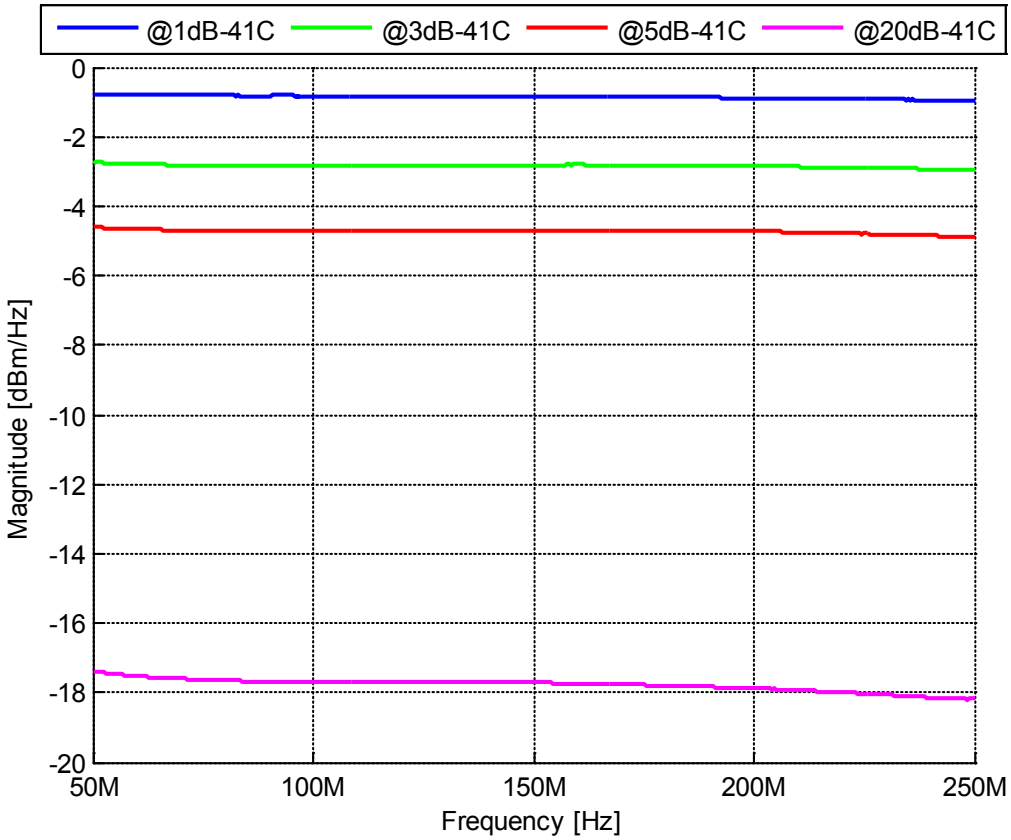

Figure 5-3 Output power spectra of the front-end module for attenuation settings

The above and other key parameters of the front-end receiver module, such as 1 dB gain compression, calibrated noise source noise temperature, radiometer switching rate, power supply voltage and current consumption, have been measured and are tabulated in Table 4. The channel 2 of the front-end module has similar gain characteristics. However, it has been disabled by default in this project.

Table 4 Measured parameters of the front-end module (MST-0512-SN2)

Parameter	Value
INPUT return loss (or reflection coefficient)	>16 dB (0.15) between 50-250 MHz
OUTPUT return loss (or reflection coefficient)	>22 dB (0.08) between 50-250 MHz
LNA 1 dB gain compression	+14 dBm
Gain	36.4 dB (50-250 MHz)
Gain flatness	± 0.6 dB (50-250 MHz)
Number of gain stages	2
Radiometer switching rate	0 to 65535 in 0.25sec step
Calibrated noise source (NC4925)	-137.5 dBm/Hz (1,288,001K)
Antenna switch isolation	> 60 dB (50-250 MHz)
Noise figure (including SW1/CPL/LNA)	< 2.4 dB (200 ± 20 K)
Noise figure (or noise temperature) of LNA	< 1.2 dB (< 90 K)
Power supply voltage	13.5 V_{min} to 20 V_{max} (15V nominal)
Current consumption	0.3 A_{min} to 0.6 A_{max} (400 mA when switching)
Weight	~ 2 kg

5.1.2 Reference Load Characteristics

The reference load resistor in the radiometer input arm is required to have a high value of return loss to reduce unwanted reflection during the Dicke switching. A resistor's DC characteristics (i.e. its resistance and tolerance) may not quite reflect its RF characteristics (in particular its reflection coefficient) at 100 MHz, for instance. Typical surface mount resistors may exhibit poor reflection coefficient at high frequencies due to the contribution from its internal parasitic inductances and capacitances. So a 50.5 Ω resistor may not provide a reflection coefficient, Γ, of 0.005 (46 dB) as expected.

Consequently, different types of 50 Ω surface mount (SM-1206) high quality and low tolerance resistors such as microwave thin film and high precision foil resistors have been selected for evaluation. The reference load chosen was a microwave thin film 50 Ω surface mount resistor (WAMT-5AT) with a 1% tolerance and temperature coefficient of 5 mΩ/K. This type of resistor is a specialised laser trimmed microwave chip resistor offering a high stability of value, flat frequency response, and low noise for frequencies up to 20 GHz. A test was conducted on a sample resistor to measure its return loss value over the

radiometer frequency range. The resistor had been mounted in an enclosure at the end of a 1cm long microstrip track on a Rogers 4003 RF board. An SMA connector on the other end of the microstrip track had been connected to one of the calibrated VNA ports. The S-parameter frequency response (S11) of the WAMT resistor was then measured using the VNA. The results showed a return loss of 48 dB (or Γ<0.004), 46 dB (or Γ<0.005), 41 dB (or Γ<0.009) at 50 MHz, 150 MHz and 250 MHz, respectively as depicted in Figure 5-4.

The return loss measurement made is consistent with the WAMT-5AT 50 Ω having a 1% tolerance specification. The measurements have been made on the R&S VNA, following the two-port calibration, at 0dBm input using 2001 spectral points and more than 500 averages.

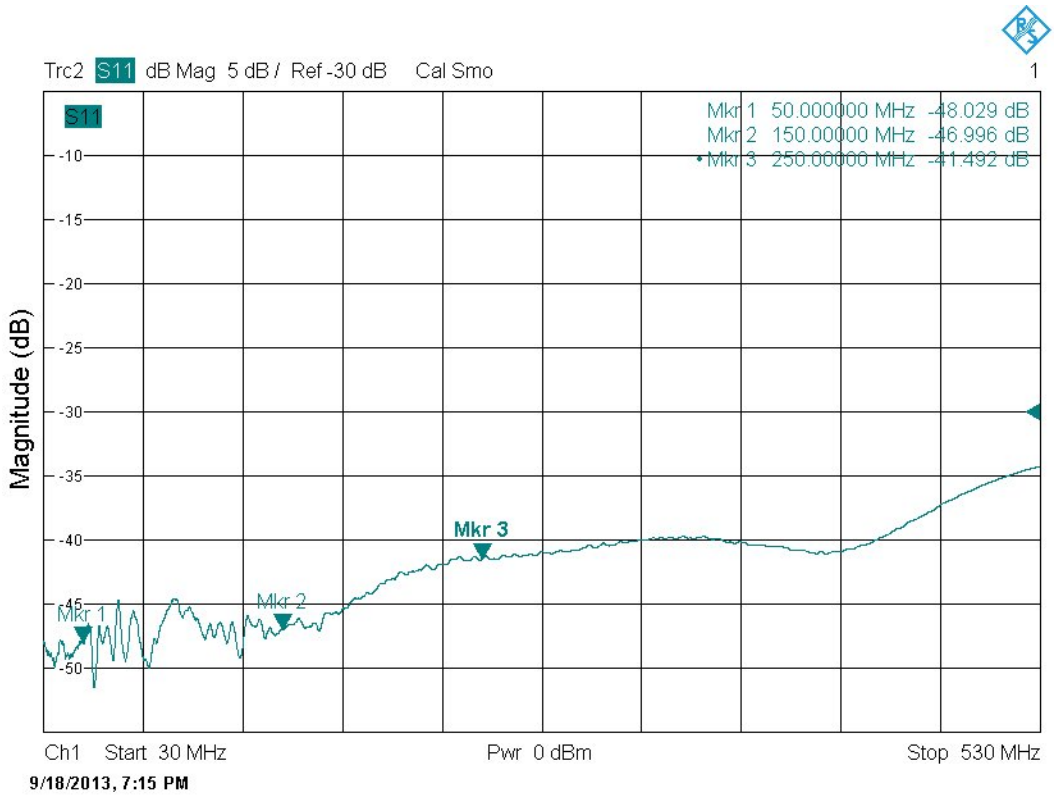

Figure 5-4 Return loss of the WAMT-5AT 50 Ω reference load

5.1.3 Receiver Cable Characteristics

The S-parameter frequency response (S21, S11, S22) of the 100 m of SPUMA-400 double screened RF cable has been measured on the Agilent VNA. The results in Figure 5-5 show a maximum insertion loss value of -6.7 dB at 250 MHz, close to the expected value from Eq 4-7 and a worst case return loss of 25.6 dB

(or Γ<0.052). The level markers on the graphs display the S-parameter (S21, S11, S22) values at spot frequencies of 50 MHz, 150 MHz, 250 MHz and 400 MHz.

The frequency response plot of the cable exhibits a constant slope of 0.014 dB/MHz over the frequency band, which can be modelled using a simple linear regression fit as follows:

$$\mathrm{IL}_{SPUMA}(f) = -0.014f(\mathrm{MHz}) - 3.15 \quad [\mathrm{dB}]. \qquad \textbf{Eq 5-1}$$

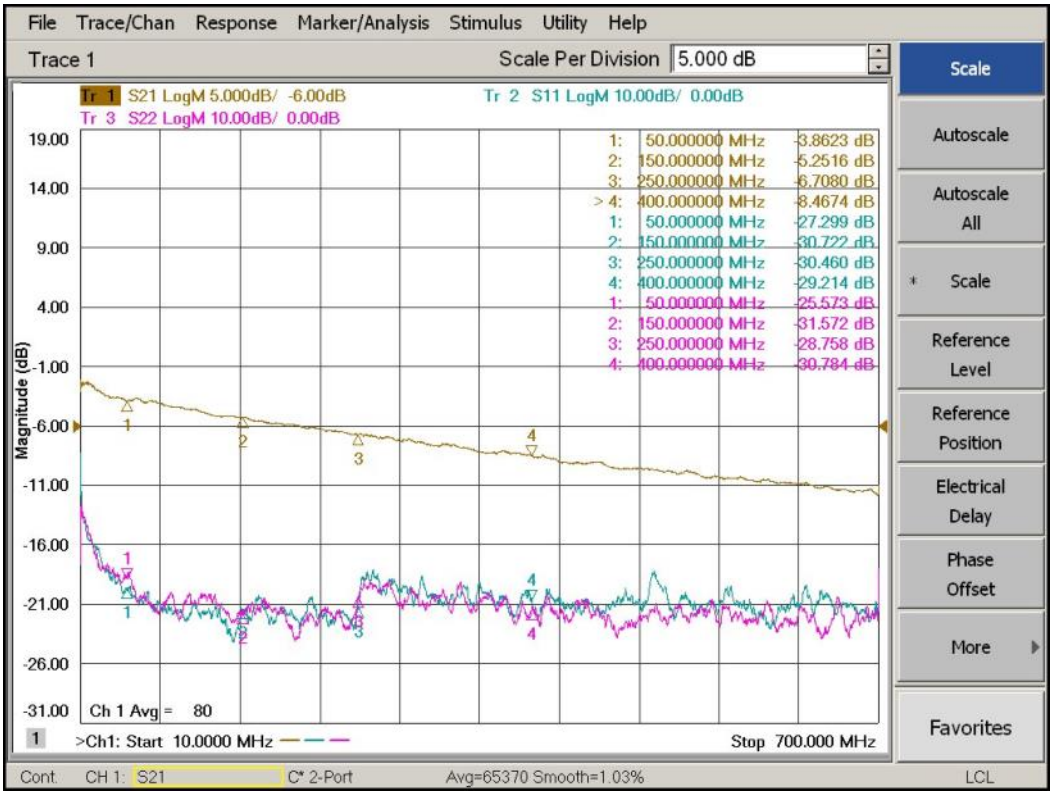

Figure 5-5 Frequency characteristics of 100 m of SPUMA-400 RF cable

5.1.4 Gain Module Characteristics

The gain module provides 41 dB amplification and an output power of 14dBm at 1 dB gain compression. The s-parameter frequency response of the gain module is shown in Figure 5-6, where S21, S11, S22 are the forward gain, the input return loss and the output return loss of the channel 1 of the gain module (assembly serial number MST-0512-SN5) respectively. Channel 2 of the gain module has similar gain characteristics.

The R&S VNA measurements have been made using 16001 spectral points from 10 MHz to 450 MHz and an averaging factor of 200 and no trace smoothing applied. Each measurement sweep lasted 4.5 s. Due to the high gain of the

amplifier the VNA had to be calibrated at a low power level of -40 dBm using the standard calibration unit (ZV-Z52). This required a full 2-port calibration to be performed prior to measurements. The input (S33) and output (S44) return losses have been manually tuned to better than 16 dB over the band. The input return loss (S33 pink trace) in the graph shows a fuzzy trace due to VNA low input power level. The level markers, Mkr1, Mkr2, Mkr3, Mkr4 on the graphs display the S-parameter values at 50 MHz, 150 MHz, 250 MHz, and 480 MHz, respectively.

The S21 plot also reveals the anti-alias filter characteristics of the gain module, having -9 dB gain at around 480 MHz, indicating more than 51 dB of stopband suppression.

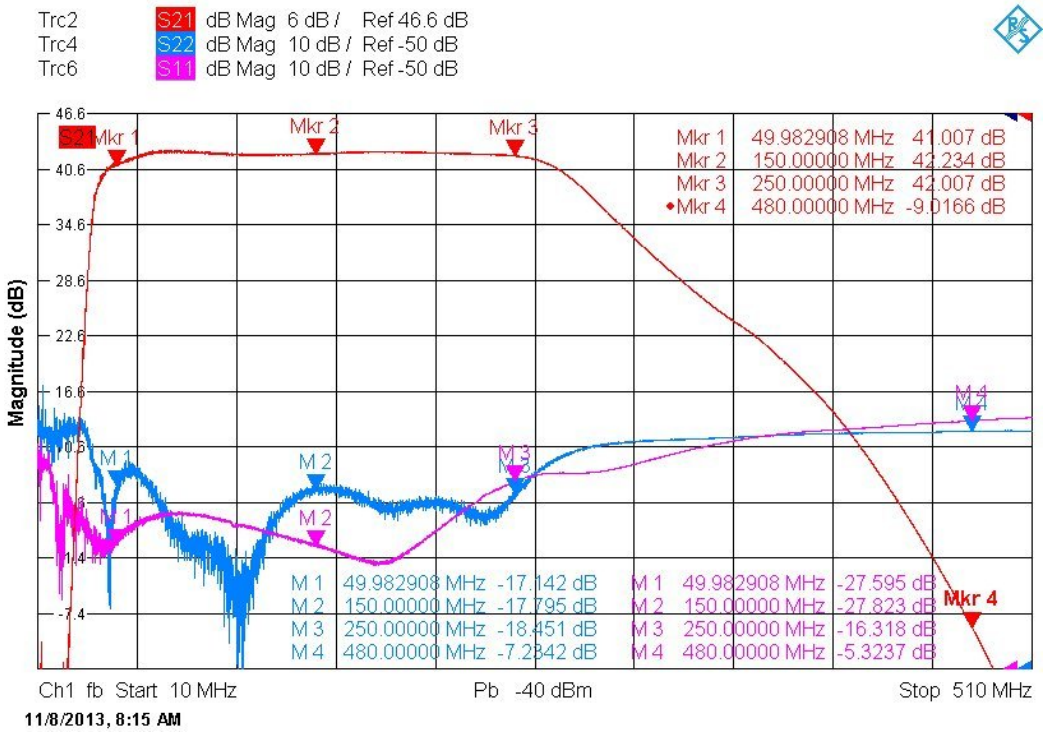

Figure 5-6 Frequency response of the gain module (MST-0512-SN5)

Next, the Agilent PNA-X network analyser has been calibrated using its calibration module configured as an impedance tuner and Agilent 346 external noise source to measure the noise temperature of the gain module over the frequency band. The gain module amplifiers have been manually tuned and optimised for noise temperatures below 100 K.

The noise temperature of the gain module is approximately 100±20 K over the 200MHz band as shown in Figure 5-7. The y-scale unit has been converted to Kelvin

and the analyser displays that in 0.1 kK (or 100 K) per division. The level markers, M1, M2 and M3 on the graphs display the noise temperature values at 50 MHz, 150 MHz, and 250 MHz, respectively.

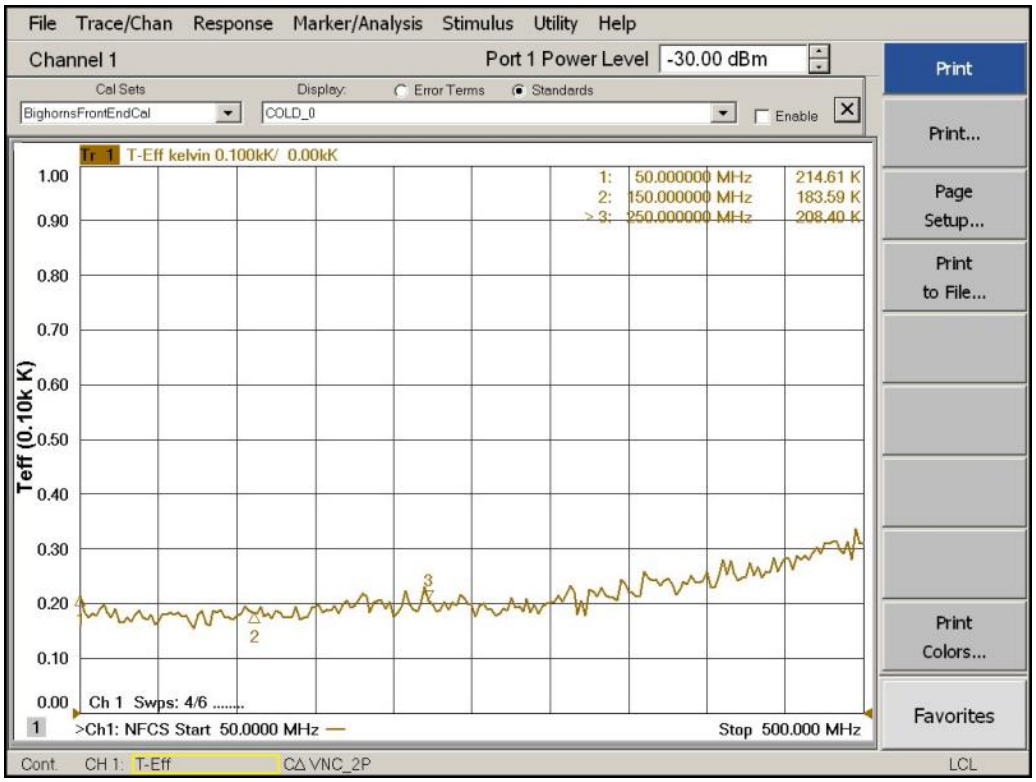

Figure 5-7 The noise temperature of the gain module (MST-0512-SN5)

The gain module has dual purpose functionality. As the gain module is to be used as the second stage of amplification at the far end of the 100 m RF cable in the back-end rack (refer to proposed setup in Figure 4-1), the module noise temperature is not critical in determining the total system noise temperature. However, due to its low input noise temperature characteristics, the gain module may also be used as a high gain LNA for spectrum monitoring and RFI measurements at the proposed sites during field trials.

The gain module also includes a digital step attenuator for the control of the output gain. Figure 5-8 shows the attenuation steps of the gain module when the internal digital step attenuator was varied from 0 dB (41 dB gain) to 30 dB (11 dB gain). The highpass and lowpass filter characteristics of the module can also be observed in Figure 5-8. There is at least 40dB suppression (that < 0dB gain when the gain is at maximum) for frequencies below 25MHz.

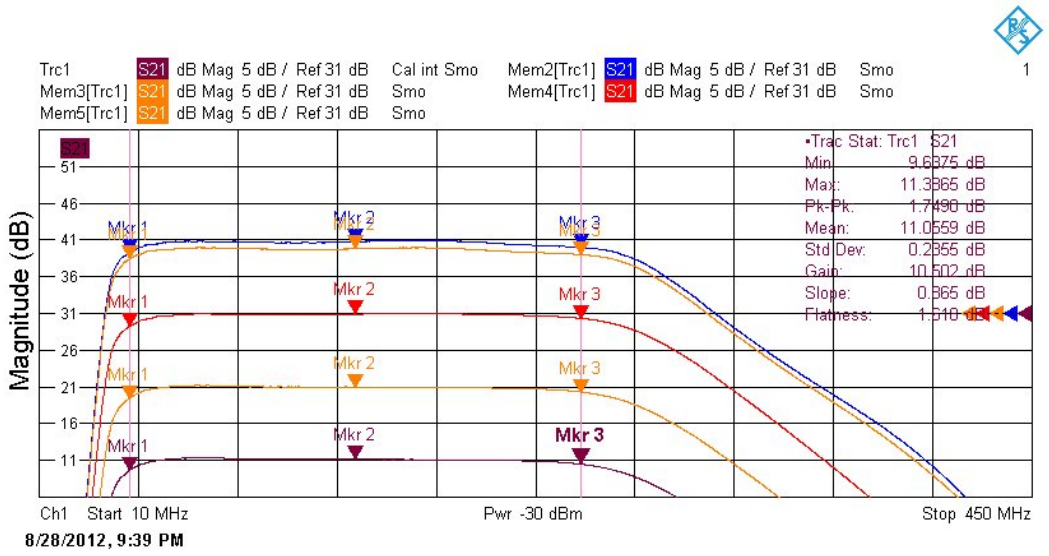

Figure 5-8 The gain module attenuation steps from 0 (41 dB) to 30 (11 dB)

Furthermore, a typical output spectrum of the gain module, when the input has been terminated with a 50 Ω connectorised resistor, is shown in Figure 5-9. The gain module shows a flatness response of less than 1 dB between 50-250 MHz. The Agilent spectrum analyser (E4407B) has been used at 30 kHz resolution bandwidth and maximum of 8192 spectral points.

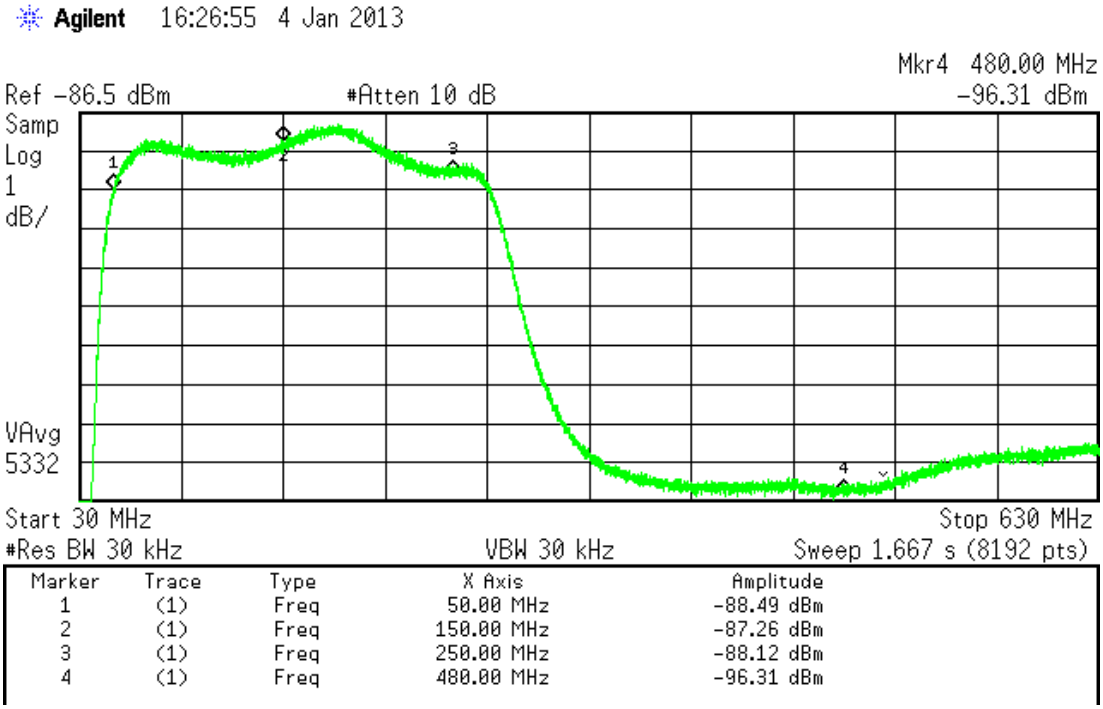

Figure 5-9 The CH1 output spectrum of the gain module (MST-0512-SN5)

The above and other main parameters of the gain module (Ch1) including the residual phase noise have been measured using Poseidon's ODIN phase noise analyser and are tabulated in Table 5.

Table 5 Measured parameters of the gain module (MST-0512-SN5)

Parameter	Value
Input return loss (or reflection coefficient)	>16 dB (0.15) between 50-250 MHz
Output return loss (or reflection coefficient)	>17 dB (0.14) between 50-250 MHz
Output 1 dB compression	+14 dBm
Gain	41.5 dB (50-250 MHz)
Gain flatness	±0.5 dB (50-250 MHz)
Number of gain stages	3
Attenuation	0 to -31.5 dB
RSSI calibrated range	50 dB (-90 to -40dBm)
Anti-alias filter stop frequency	Down by 56 dBc @ 480 MHz
Noise figure (or noise temperature)	1.28 dB (100 K) @ 150 MHz
Residual Phase Noise @ 150 MHz	-128 dBc/Hz@ 10 Hz -136 dBc/Hz@ 100 Hz -142.3 dBc/Hz@ 400 Hz -142.5 dBc/Hz@ 1 kHz -142.5 dBc/Hz@ 10 kHz
Power supply voltage	6 V_{min} to 20 V_{max} (15V nominal)
Current consumption	500 mA one amplifier chain, 830 mA two amplifier chains
Weight	~2 kg

Finally, the photo of the RF section of the completed gain module is shown in Figure 5-10. The various RF sections, the three cascaded low noise amplifier chains, attenuators, logarithmic detectors (referred to as RSSI), anti-alias lowpass (LP) filters and humidity sensor are marked in red. As can be seen in the figure, the middle stage amplifiers in both chains have been enclosed in an EMI metal shielding box to reduce radiated cross coupling between the cascaded stages. The low pass filters in both chains have also been enclosed in an EMI shielding box. The picture shows the shielded boxes with the lids removed.

Moreover, the amplifiers have also been heatsinked to chassis through a metal block under the PCB for improved thermal stabilisation of the amplifiers.

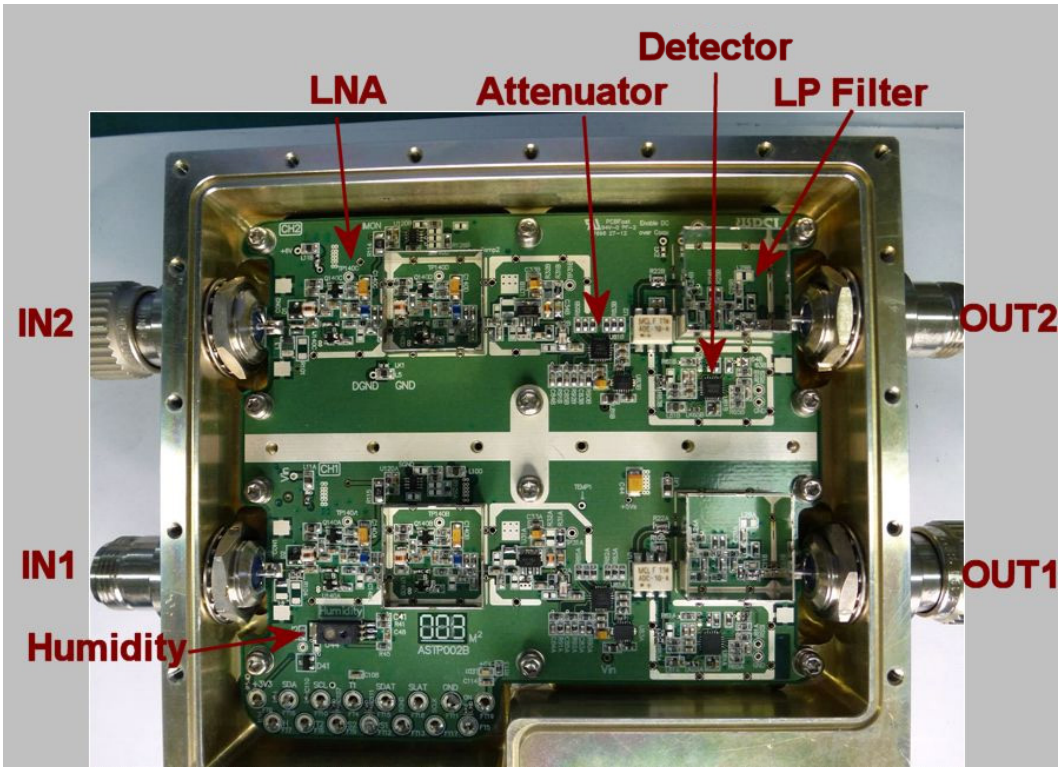

Figure 5-10 Photo of the RF section of the gain module (MST-0512-SN5)

5.1.5 Receiver System Noise Temperature

The receiver noise temperature, T_{Rec} , at the receiver front-end module includes contributions from the internal components such as Dicke switch, coupler, LNA and other receiver components following the front-end module, including 100 m interconnecting cable and gain module contributions, through to the back-end digitiser. This can be written as follows:

$$T_{Rec} = T_{SW} + T_{Coupler} + T_{LNA} + \sum \frac{T_i}{G_{i-1}} \,, \qquad \text{Eq 5-2}$$

where T_i is the noise temperature of the ith component in the receiver and G_{i-1} is the insertion gain at the input to that ith component. However, the noise temperature is mostly dominated by the first three terms shown above, in the front-end module, and is calculated as 214 K (equivalent to noise figure of 2.4 dB).

In general, the total noise temperature of the BIGHORNS system also includes the balun and cable loss connecting the balun to the front-end module. Consequently, the total system noise temperature may be written as follows:

$$NT_s = T_{balun} + T_{cable} + T_{sw} + T_{coupler} + T_{LNA} + \sum \frac{T_i}{G_{i-1}} . \qquad \textbf{Eq 5-3}$$

Figure 4-1 in the previous chapter shows the conceptual block diagram of the BIGHORNS field setup, where the input of the receiver front-end module is connected to the antenna via a balun and a short RF cable, and on the output side connected to a follow-up gain module 100 m away in the digital backend rack.

In this configuration, the system total noise temperature, mainly dominated by the first five terms in Eq 5-3, can be calculated as shown in Figure 5-11. The estimated total system noise temperature, NT_s, is 345 K (or NF_s = 3.4 dB) including 1.5 dB insertion loss between antenna and the receiver front-end module due to balun and cable losses. It is also assumed that a 3 dB attenuator has been placed between the gain module and the data acquisition system in the back-end rack to improve match between the gain module and the data acquisition input.

Input Power: -80 dBm

					Output Values				
Component Name	Gain (dB)	NF (dB)	IP3 (dBm)	NT Comp (K)	Pwr (dBm)	Gain (dB)	NF (dB)	NT (K)	IP3 (dBm)
Ant/Bal Cable	-0.2	0.2	999	13.667	-80.2	-0.2	0.200	13.667	999.00
Balun (ADT3-1T)	-0.5	0.5	999	35.385	-80.7	-0.7	0.700	50.720	995.73
Ant/Rec Cable	-0.3	0.3	999	20.741	-81	-1	1.000	75.088	993.85
SW/Coupler Insertion Loss	-1.2	1.2	999	92.294	-82.2	-2.2	2.200	191.280	991.74
LNA1	37.5	1.2	30	92.294	-44.7	35.3	3.400	344.451	30.00
100m Cable	-6.5	6.5	999	1005.382	-51.2	28.8	3.402	344.748	23.50
Gain Module	41.5	1.2	38	92.294	-9.7	70.3	3.403	344.869	37.99
Attenuator	-3	3	999	288.626	-12.7	67.3	3.403	344.869	34.99

Figure 5-11 BIGHORNS receiver system noise figure calculations

5.1.6 Receiver Gain Module Noise Leakage

During one of the field trips it was observed that the gain module CH1 output spectrum suffers from unwanted spurious noise spikes. Moreover, it required an extra gain stage, for a total gain greater than 40 dB, to increase the input level to the back-end data acquisition to the required level.

The module was tested in the laboratory, modified and reconfigured, to improve the leakage. The spurious spikes were observed approximately 3 dB above the power spectrum at $-138\ \frac{\mathrm{dBm}}{\mathrm{Hz}}$ in the middle of the band. These spurious spikes had been present even when the input had been terminated with a 50 Ω resistor, which had made it easier to diagnose and investigate the sources of oscillation. A spectrum analyser (Agilent E4407B) has been utilised for debugging the circuitry in the laboratory. Figure 5-12 shows the spurious spectrum in 1 dB scale per

division as measured in the laboratory, when the analyser had been adjusted for a maximum of 8192 spectral points.

Initially, to ensure that the RF amplifier board was not the source of spurious noise, the microcontroller board was totally powered down and disconnected. Then the RF board was powered up separately using the on board 6 V regulator and the output spectrum was monitored on the analyser. In this case, no spurious noise spikes were observed in either CH1 or CH2 sections.

Then the microcontroller board was reconnected and powered up again. RF field probes were used to detect any spurious conducted or radiated emissions on the microcontroller circuitry. It was observed that the harmonics of the microcontroller 10 MHz reference clock, I2C clock and RS485 transceiver internal oscillator on the board have been mixed, up-converted and coupled to the RF board through feedthrough capacitors.

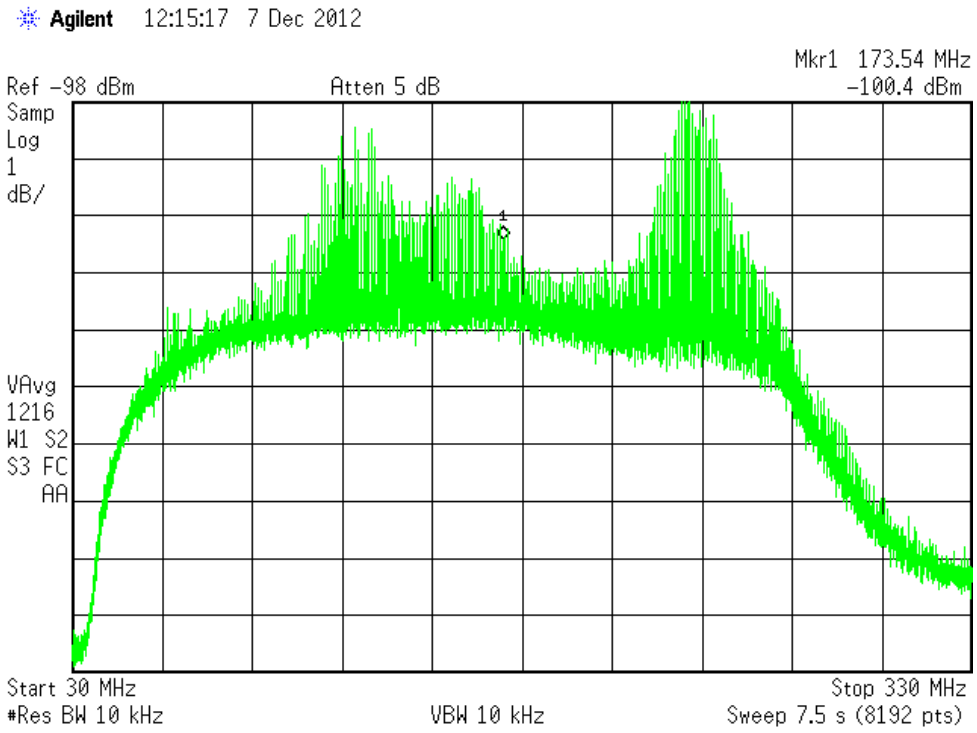

Figure 5-12 Gain module output spectrum before modification

Both RF and controller lids are RF sealed and isolated from the external environment. However, C-section feedthrough capacitors (Tusonix 4400-076-100pF and 4400-093-10nF) have been used to pass DC, switching signals, and SPI and I2C lines (SCL/SDA) from the PIC microcontroller to the RF amplifier

side. The SPI lines have been routed to the RF board to adjust and control the attenuation settings in the digitally controlled attenuators.

Furthermore, the I2C digital isolators (Analog Devices ADUM1251) isolating the microcontroller I2C lines were used to monitor supply voltages of the RF amplifiers on the RF board in the gain module. Due to wrong terminations of I2C tracks on the RF boards the high impedance tracks were carrying and injecting spurious signals to the RF amplifiers through power supply lines.

Once the sources of spurious noise were identified, a series of methodical modifications have been carried out on the circuit boards one by one to clean the gain module output spectra which included the following:

- To completely remove the key source of radiation without modifying the circuit board layout, it was decided to disconnect the I2C tracks on both RF and MC boards completely and remove the amplifier voltage monitoring feature.
- The three SPI lines (SCLK/SDAT/SLAT) were modified to increase line filtering using low pass RC filter networks (320 kHz bandwidth).
- Power supply filtering was also increased by 10 times to reduce any possible RF leakage through power supply lines in the RF attenuators.
- The RS485 transceiver ground (DGND) on the chip was isolated from the local system ground (Chassis GND) via an insertion of a 100 Ω (replaced ASTP003A-R75=100 Ω) resistor as recommended by the RS485 standard.
- The reference 10 MHz oscillator supply rail was further filtered to reduce RF leakage through to MC board supply lines.

Finally, a third stage amplifier which was not populated, was added to increase the gain to above 40 dB. The need for this was identified from experience in early field experiments. Figure 5-13 shows the gain module spectrum after the two modifications described above. No spurious signals were observed in the spectrum at 1 dB scale per division using 10 kHz resolution bandwidth on the spectrum analyser and 8192 spectral points.

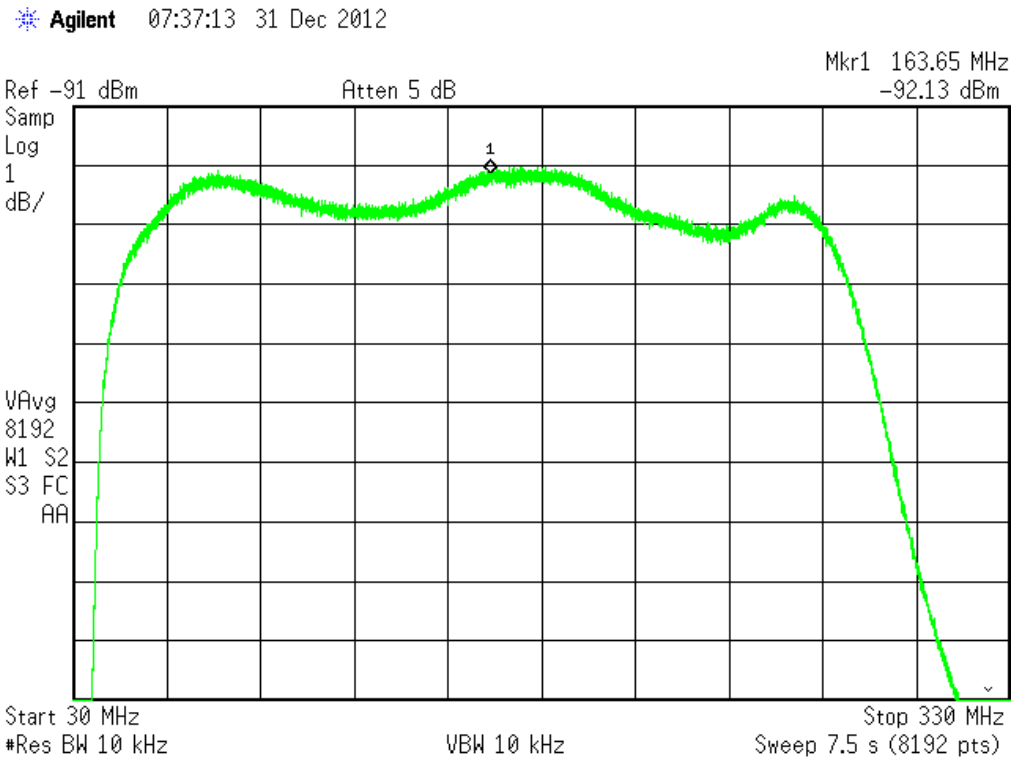

Figure 5-13 Gain module output spectrum after modifications and addition of a third stage amplifier to increase the overall gain

5.2 Radiometer Output Voltage

Next the radiometer output and its switching transients have been observed and examined in the time domain.

The typical radiometer output voltage has been measured and captured on an oscilloscope by using a coaxial Schottky detector (DRZ124AA). The test has been conducted when the two receiver modules have been connected back-to-back using a short semi-rigid cable while an external hot noise source (NoiseCom NC3201-ENR32) was connected to the input of the front-end module.

Figure 5-14 shows the RF and the detected output voltage plots as captured by a high speed digital oscilloscope. The figure displays the radiometer output when the front-end microcontroller was set to toggle the relay switches at every 10 s intervals through the four distinct states, namely the reference load, the reference load plus noise, the antenna and the antenna plus noise states respectively.

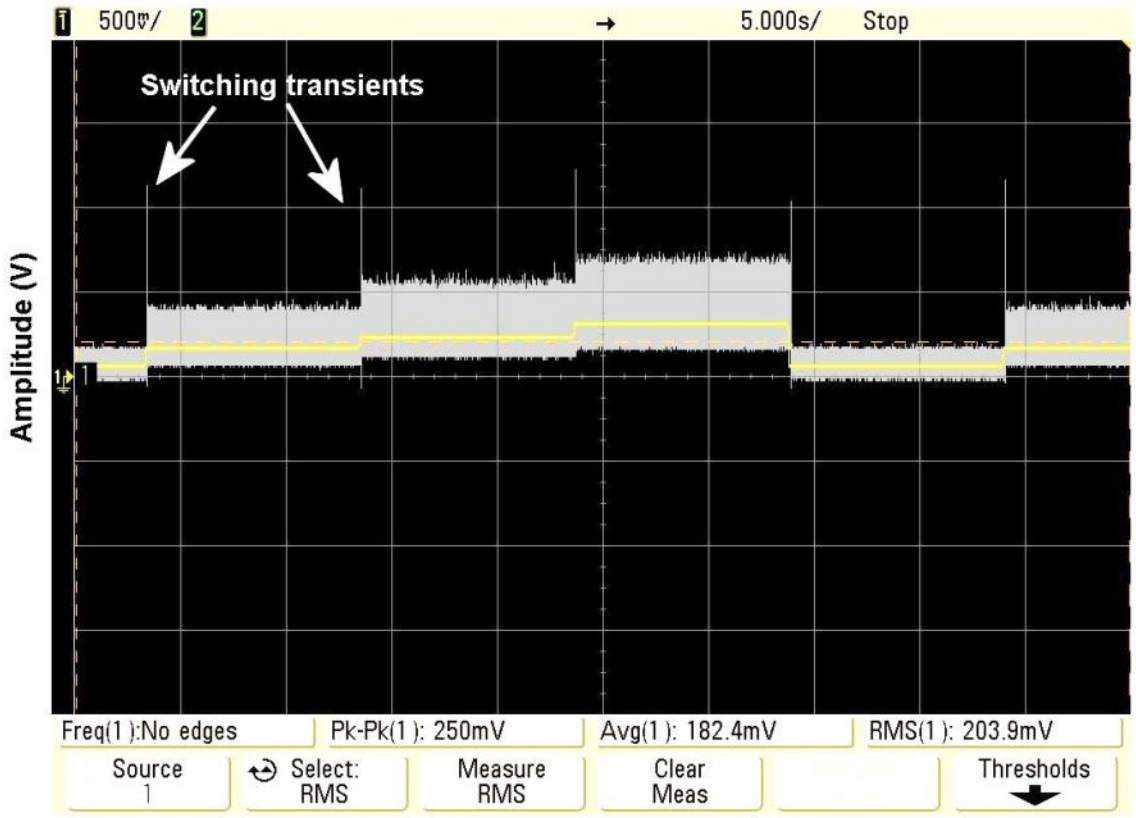

Figure 5-14 Radiometer detected output voltage measured on an oscilloscope

In the figure the transient spikes of the RF relays are shown to be a fraction of a second wide (less than 10ms). Hence, the back-end data acquisition post processing routine can confidently use this information to discard single time samples around each state change.

5.3 Radiometer Thermal Tests

In order to develop an accurate model of the receiver, the performance of the radiometer over temperature was also investigated. This would result in a set of linear temperature coefficients that would define the receiver temperature responses. Various RF sections in the receiver front-end and gain module PCBs have been subjected to controlled temperature variations and their performance characteristics measured in-situ. Each receiver module has been placed on a temperature controlled hot plate while the individual sections were being tested. A warm up time of at least an hour was required to ensure the enclosure is at a stable temperature prior to measurements. In addition, the measurements have been carried out in an air conditioned environment during evenings and weekends to ensure reduced disturbances during long averaging times.

5.3.1 Noise Source Thermal Characteristics

Initially, the characteristics of one of the surface mount NC4925 noise sources had been measured. The noise source had been mounted on a Rogers 4003 microstrip board and placed in an aluminium enclosure for testing. The noise source test enclosure was placed on a temperature controlled hot plate in a laboratory environment.

Figure 5-15 shows the measured frequency response of the noise source module at three separate temperatures while the noise source DC input voltage was regulated. The results have also been converted to Kelvin and are shown in Figure 5-16 . In addition, the frequency response plots show a variation of less than ±0.3 dB over the frequency range.

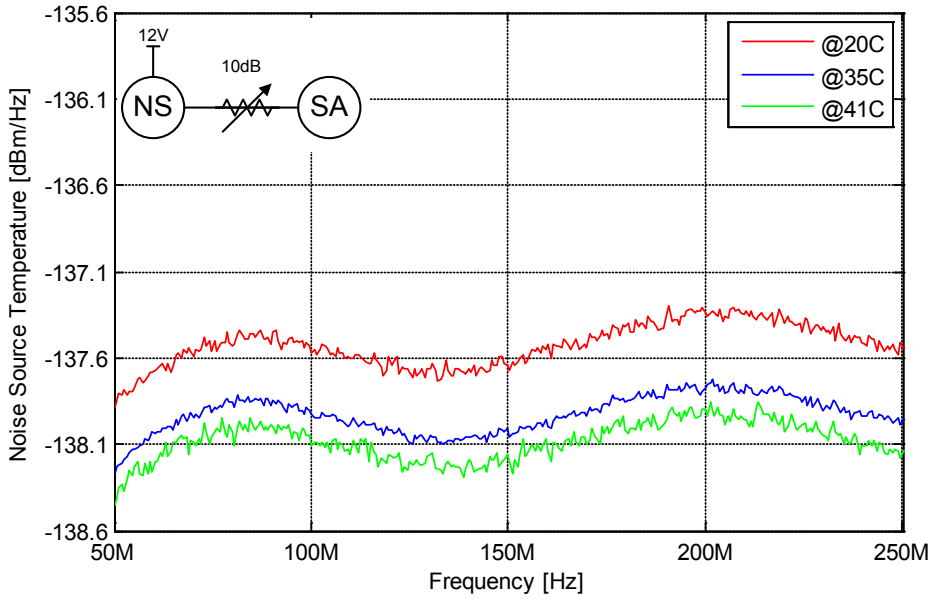

Figure 5-15 NC4925-SN5 frequency response variation over temperature (in dBm/Hz)

The measurements have been made using Agilent portable N9344C spectrum analyser with 310 spectral points and more than 500 averages between 50-250 MHz at 10 kHz resolution bandwidth. Each measurement sweep was 0.6 s.

Using the above results the noise source ENR was also estimated. A temperature sensor attached on top of the noise source module has been used to monitor its temperature. The analyser noise floor when the noise source was off was -162 dBm/Hz (4570 K) . Using the Y-factor method, the excess noise ratio at a centre frequency of 150 MHz at 35°C is:

$$ENR = 10\log\left(\frac{T_{on} - T_{off}}{T_0}\right),$$

$$\sim 10\log\left(\frac{1147923K\ - 4570\ K}{308\ K}\right) \qquad \text{Eq 5-4}$$

$$\sim 35.7\ dB\ .$$

This value of ENR estimated is consistent with the NC4925 noise source specification of 36 dB.

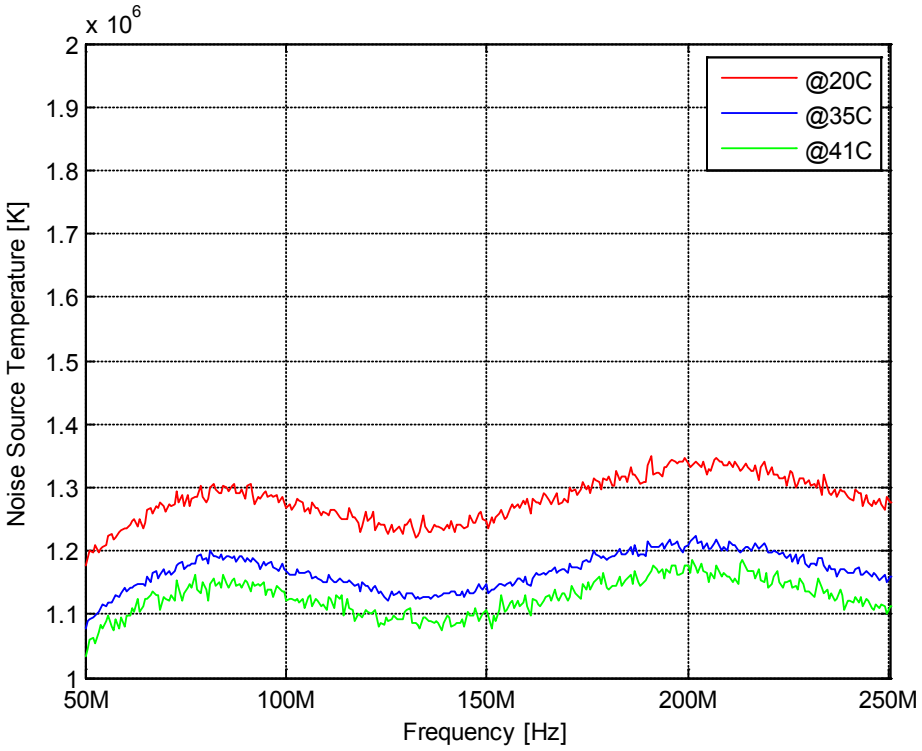

Figure 5-16 NC4925-SN5 frequency response variation over temperature (in K)

Taking the difference between the spectra in Figure 5-15, the variation due to temperature effects is 0.4 dB over 15 ºC showing an average temperature variation of 0.026 dB/ºC. This is more than twice the value expected from the manufacturer datasheet. This discrepancy may be partly due to voltage fluctuations in the voltage regulator used in the order of 0.01 dB.

The temperature effects over frequency band, as shown in Figure 5-17, can be estimated with a linear regression line as follows:

$$\mathrm{P}_{\Delta\mathrm{T}}(f) = -0.026f(GHz) - \ 0.023 \quad [\mathrm{dB/ºC}]. \qquad \text{Eq 5-5}$$

The residual plot, after the linear fit, shows peak fluctuations of less than 0.005 dB and a standard deviation of 0.0018, mostly representative of spectrum analyser trace noise stability due to instrument resolution bandwidth and averaging applied in this case.

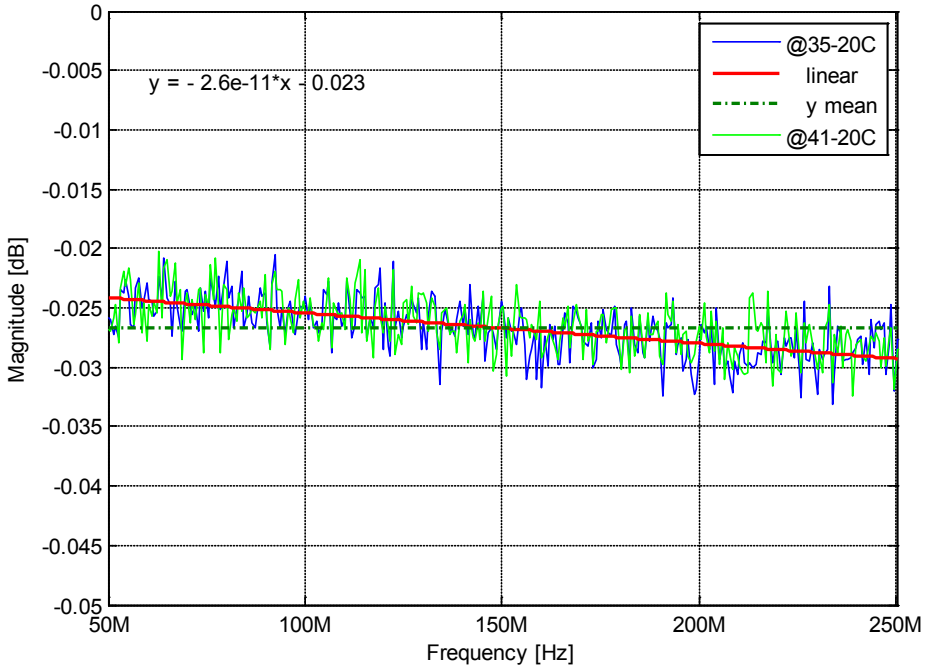

Figure 5-17 NC4925-SN5 temperature effects over frequency

In addition, the noise source frequency response was also measured with respect to power supply variations, when it was connected directly to a calibrated DC power supply (Agilent E3632A). The power supply was varied between 11.6 V and 12.2 V. The noise source showed supply variations of 0.5 dB for a 0.6 V change. This represents a 0.83 dB/V or 0.1 dB/%ΔV at 12 V consistent with a typical value in the NoisCom specifications. The main parameters of the noise source measured are shown in Table 6 below.

Table 6 Measured parameters of the noise source (NC4925-SN5)

Parameter	Value
Power output over frequency	-138±0.3 dBm/Hz
Excess noise ratio (ENR)	35.8±0.3 dB (20°C to 40°C)
Noise temperature over frequency	1.15±0.073 x10^6 K
Supply current	3 mA
Supply voltage	12 V
Temperature coefficient	0.026 dB/°C
Supply sensitivity	0.1 dB/%ΔV

5.3.2 Front-end Component Thermal Characteristics

Next the on-board radiometer components at the input of the front-end module have been characterised. The tests include the combined insertion loss of the Dicke switch and coupler, noise adding switch and coupler, and the dual stage low noise amplifier followed by the overall front-end module gain, when the internal noise source is on.

Figure 5-18 shows the frequency response variations of the combined comparison switch (S1) and coupler insertion loss (L1) section in the front-end module at two different temperatures. The VNA test port output level was set to 0dBm to decrease measurement uncertainty. The plots show 0.52 dB of variation over the 200 MHz frequency band or 0.0027 dB/MHz and 0.0026 dB/°C mean variations over the temperature range.

As can be seen in Figure 5-18, the gain of the combined input coupler and S1 switch in both plots exhibits a constant negative slope (i.e. loss) over the frequency band which can be modelled using a linear regression fit as follows:

$$\mathrm{M}_{16C}(f) = -0.0027f(\mathrm{MHz}) - 0.77 \quad [\mathrm{dB}], \qquad \textbf{Eq 5-6}$$

$$\mathrm{M}_{51C}(f) = -0.0027f(\mathrm{MHz}) - 0.86 \quad [\mathrm{dB}]. \qquad \textbf{Eq 5-7}$$

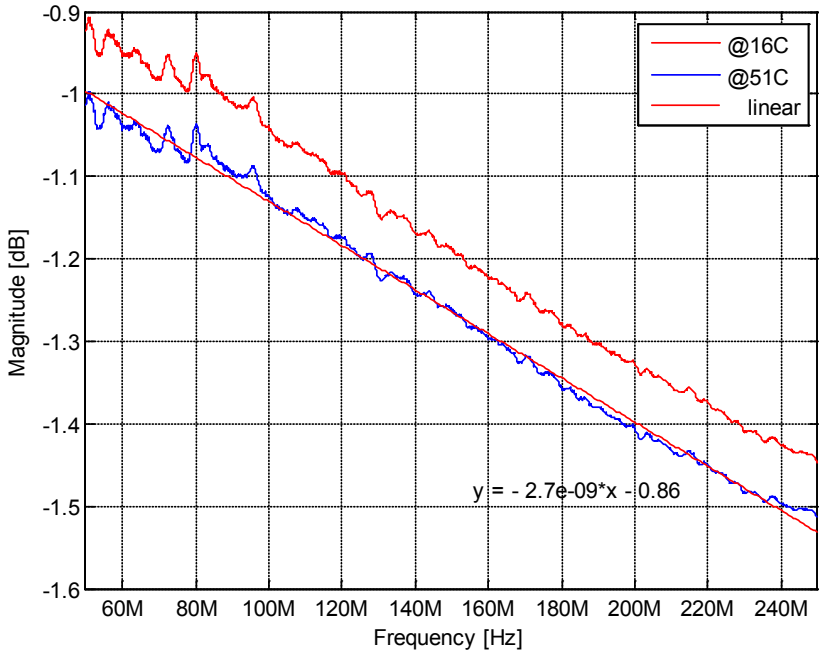

Figure 5-18 Combined loss of S1 and coupler over frequency band and temperature

When the frequency responses in Figure 5-18 are subtracted the variations (ΔM_T) are small having a mean of -0.078 dB and a slope of 0.0045. The effect can be modelled as a linear relationship:

$$\Delta \mathrm{M}_T(f) = 0.0045f - 0.0783 \quad [dB], \qquad \textbf{Eq 5-8}$$

where the fit has been centred at 150 MHz and scaled according to:

$$f = \frac{x(MHz) - 150MHz}{57.745MHz}.$$

The difference and the residuals are shown in Figure 5-19. The residual plot, after a linear fit, shows fluctuations under 0.005 dB, representative of network analyser instrument calibration limitations.

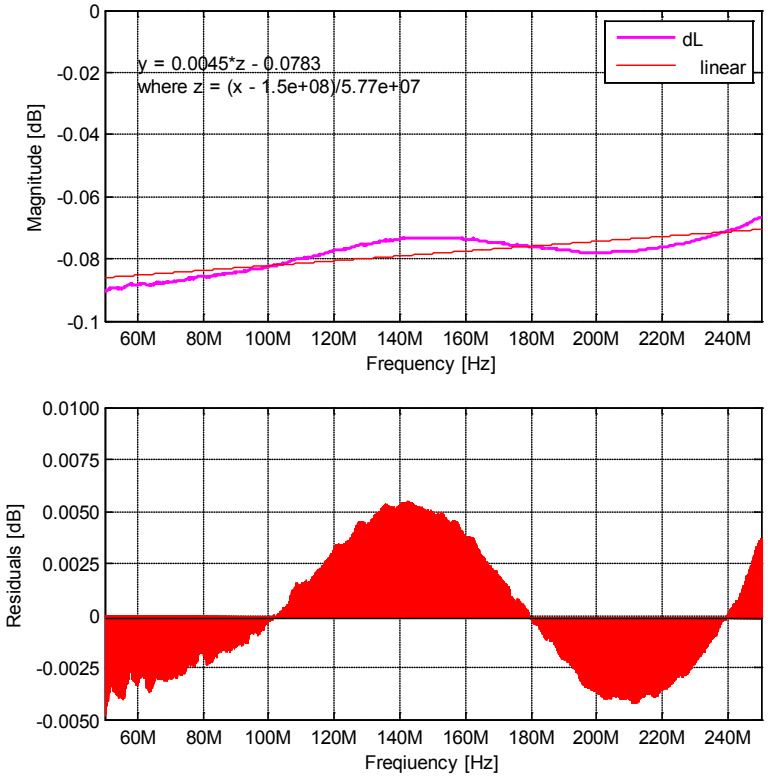

Figure 5-19 Dicke switch and coupler temperature variation & residuals over frequency

To verify that the residual fluctuations are due to instrument calibration limitations, estimates of errors in reflection and transmission coefficients have been carried out using the VNA for output port levels of -40dBm and 0dBm. The results indicate that at low output port levels, magnitude and phase errors can pose a challenge, and cause some uncertainties in how accurately the s-parameters S11

and S21 can be measured. The measurements at low input levels of -40 dBm can introduce residual errors of 0.01 dB in transmission, after removing the fit to the DUT response. At higher levels this error can reduce to 0.003 dB (or fractional accuracy of ~70 mK in 100K). This confirms the results seen for the Dicke switch and coupler residuals in Figure 5-19 above.

Based on Eq 5-6, Eq 5-7 and Eq 5-8, the input gain due to the comparison switch and coupler, M_1, can be combined and modelled over the frequency and temperature range as follows:

$$M_1(f,T) = -0.0027f(\text{MHz}) - 0.0026T - 0.728 \quad [\text{dB}]. \qquad \textbf{Eq 5-9}$$

Eq 5-9 can be used to predict the insertion loss characteristics of the input Dicke switch and coupler over the frequency band and temperatures. In this case, the temperature monitors, T1, T2 and T3, can be extracted and time-stamped along with the captured power spectra for later post processing and temperature correction.

Next, the noise adding radiometer arm has been tested and characterised. Figure 5-20 shows the frequency response variations of the combined loss of the coupled output arm of the coupler and noise adding switch, S2, and the series attenuator (set to 0dB) in the front-end module. The VNA test port output level was, in this case, set to 0dBm to decrease measurement uncertainty. The plot shows approximately 1 dB of variation over the frequency band and 0.0067 dB/°C variation over the temperature range. The curves can be estimated with a 2nd order polynomial.

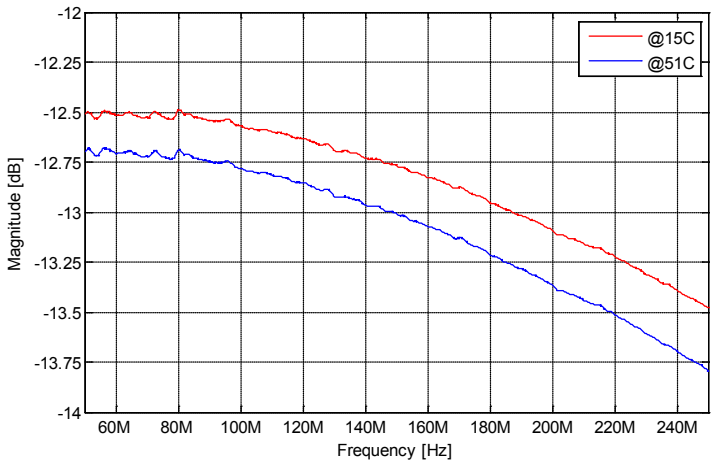

Figure 5-20 Combined loss of S2 and coupler over frequency band and temperature

As seen in Figure 5-20, the insertion gain of the combined input coupler and switch (S2) in both plots exhibits a smooth negative slope (i.e. loss) over the frequency band which can be modelled using second order equations as follows:

$$\mathrm{M}_{15C}(f) = -0.07f^2 - 0.3f - 12.77 \quad [\mathrm{dB}], \qquad \textbf{Eq 5-10}$$

$$\mathrm{M}_{51C}(f) = -0.07f^2 - 0.3f - 13.01 \quad [\mathrm{dB}], \qquad \textbf{Eq 5-11}$$

where the frequency axis was scaled as $f = \frac{x(MHz) - 150MHz}{57.745MHz}$.

By subtracting the two coupled loss responses in Figure 5-20, the additional variations over frequency due to changing temperature can be plotted as shown in Figure 5-21. This variation is linear and can be modelled as a linear regression as follows:

$$\Delta\mathrm{M}(f) = -0.00063f(\mathrm{MHz}) - 0.1479 \quad [\mathrm{dB}]. \qquad \textbf{Eq 5-12}$$

When the frequency responses in Figure 5-20 are subtracted the variations (ΔM) are small having a slope of 0.00063 dB/MHz.

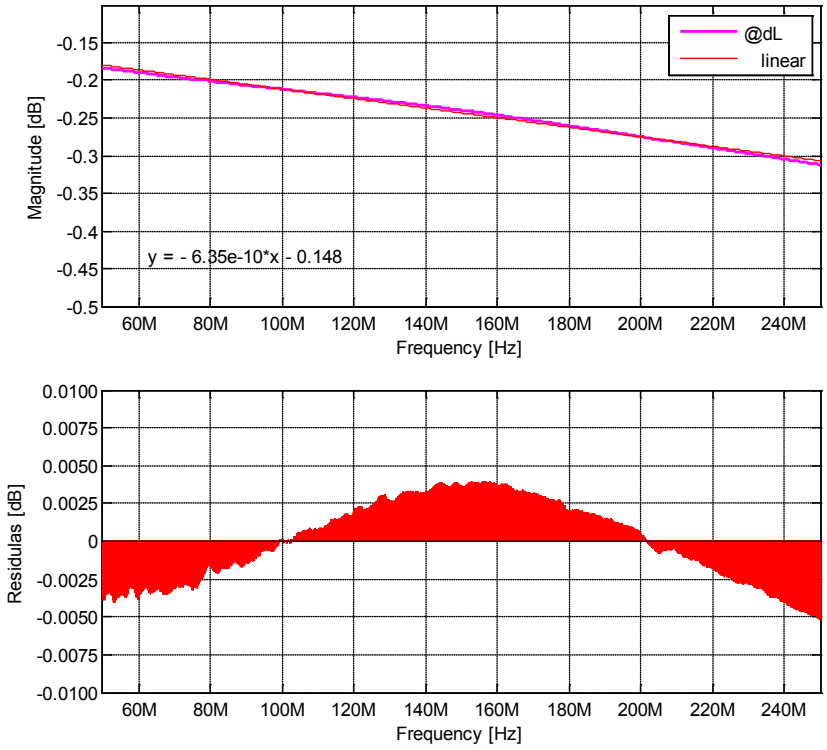

Figure 5-21 Residual after temperature variations subtracted

The residuals after a linear fit shows fluctuations under 0.004 dB, representative of network analyser instrument calibration limitations.

Similarly, based on Eq 5-10, Eq 5-11 and Eq 5-12, the coupled insertion responses, M_2, can be combined and modelled over the frequency and temperature range as follows:

$$M_2(f,T) = -0.07f^2 - 0.3f - 0.0067T - 12.67 \quad [\text{dB}]. \qquad \textbf{Eq 5-13}$$

Next, the gain response of the front-end amplifier has been measured when its input was disconnected from the input coupler. Figure 5-22 below shows the gain variations of the dual amplifier section in the front-end module. The frequency response measurements have been made at an input level of -40 dBm to avoid the amplifier saturation. Large averaging factors were also required to increase sensitivity and reduce measurement uncertainties. The dual amplifier frequency response shows 0.8 dB of variation over the frequency band.

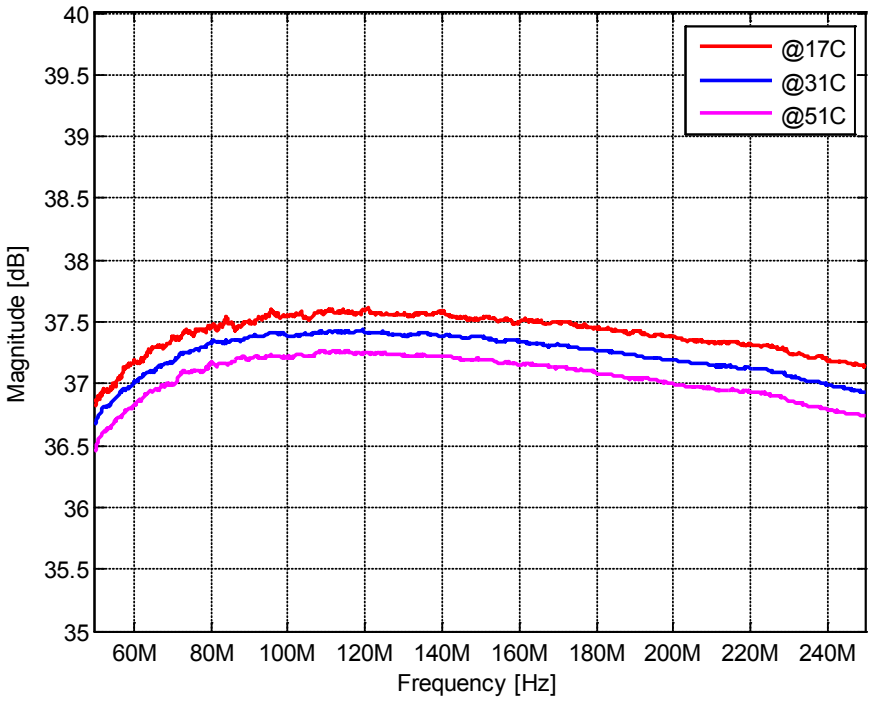

Figure 5-22 Front-end amplifier gain response variations over temperature

The data in Figure 5-22 are fit with a 4th order polynomial having residual fluctuations less than 0.05 dB as follows:

$$G_{17C}(f) = -0.05f^4 + 0.07f^3 - 0.03f^2 - 0.16f - 37.53 \quad [\text{dB}], \qquad \textbf{Eq 5-14}$$

$$G_{31C}(f) = -0.05f^4 + 0.07f^3 - 0.03f^2 - 0.16f - 37.36 \ \text{[dB]}, \quad \textbf{Eq 5-15}$$

$$G_{51C}(f) = -0.05f^4 + 0.07f^3 - 0.03f^2 - 0.16f - 37.19 \ \text{[dB]}, \quad \textbf{Eq 5-16}$$

where $f = \dfrac{x(MHz) - 150MHz}{57.745MHz}$.

When the difference is taken between the 51°C and 31°C plots against the 17°C plot, the temperature effect can be estimated as having a mean of 0.17 dB and 0.34dB at 31 °C and 51 °C, respectively. This indicates a mean temperature variation of 0.01 dB/°C for the amplifier.

As a result, based on Eq 5-14, Eq 5-15 and Eq 5-16, the amplifier gain responses, G , can be combined and modelled over the frequency and temperature range as follows:

$$G(f,T) = -0.05f^4 + 0.07f^3 - 0.03f^2 - 0.16f + 0.01T - 37.7 \ \text{[dB]}. \quad \textbf{Eq 5-17}$$

It should be noted that in the case of the 3-position switching to estimate the antenna temperature the effects of the receiver gain can be calibrated out as described in section 3.8.1, assuming no noise perturbations exist at the antenna input to upset the input matching. The measurements have been carried out, in this instance, to ensure no anomalies exist in the frequency response. However, if the radiometer is used in the total power mode Eq 5-17 may be used to calibrate the radiometer.

Finally, the frequency response of the combined components in the front-end module has been measured when the antenna input has been terminated and internal noise source has been switched on. Figure 5-23 below shows the combined gain variations of the front-end module. The data in Figure 5-23 are fit with a 6th order polynomial having residual fluctuations less than 0.05 dB as follows:

$$P_{19C}(f) = -0.03f^6 + 0.11f^5 + 0.08f^4 - 0.36f^3 - 0.20f^2 + 0.43f - 113.24 \ \text{[dBm/Hz]}, \quad \textbf{Eq 5-18}$$

and

$$P_{41C}(f) = -0.03f^6 + 0.11f^5 + 0.08f^4 - 0.36f^3 - 0.20f^2 + 0.43f - 113.69 \ \text{[dBm/Hz]}, \quad \textbf{Eq 5-19}$$

where $f = \dfrac{x(MHz) - 150MHz}{57.923MHz}$.

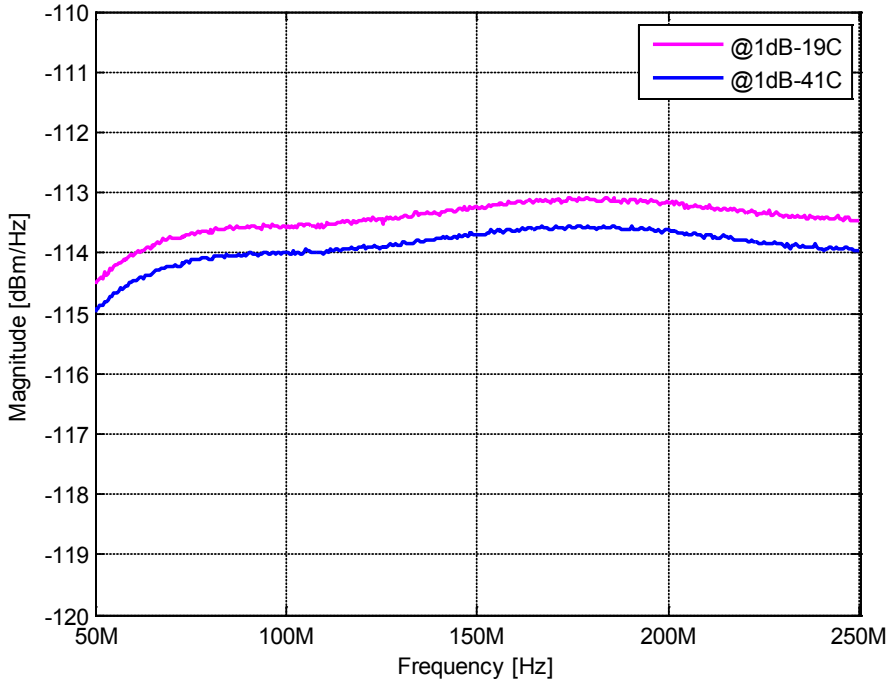

Figure 5-23 Front-end module response when internal noise source was on

Combining the two equations above, the front-end response over frequency and temperature range of 19 °C and 41 °C can be modelled as follows:

$$\mathrm{P}_{FE}(f,T) = -0.03f^6 + 0.11f^5 + 0.08f^4 - 0.36f^3 - 0.20f^2 + 0.43f - 0.02\mathrm{T} - 112.87 \left[\frac{\mathrm{dBm}}{\mathrm{Hz}}\right]. \quad \textbf{Eq 5-20}$$

The equation above defines the front-end module characteristics over temperature and frequency for the internal noise source attenuation setting of 1 dB.

5.3.3 Gain Module Thermal Characteristics

Finally in this section, the gain module temperature variations have been examined and analysed for any anomalies or inconsistencies in the frequency response. The measurements have been made using the Agilent N9344C spectrum analyser with 460 spectral points and more than 3000 averages between 50-250 MHz at 10 kHz resolution bandwidth and sweep time of 12s. The spectrum analyser noise floor contribution, when the amplifier was off, has also been measured and calibrated out.

Figure 5-24 shows the output spectral desnity variations of the combined amplifier, attenuator and filter sections in the gain module at two different temperatures. The gain module input had been terminated with a 50 Ω and set to maximum gain (42 dB@150 MHz). The curve shows a maximum of 1.2 dB variation over the 200 MHz frequency band and 0.009 dB/°C mean variation over temperature, which indicates a good thermal stability for a multi-stage amplifier.

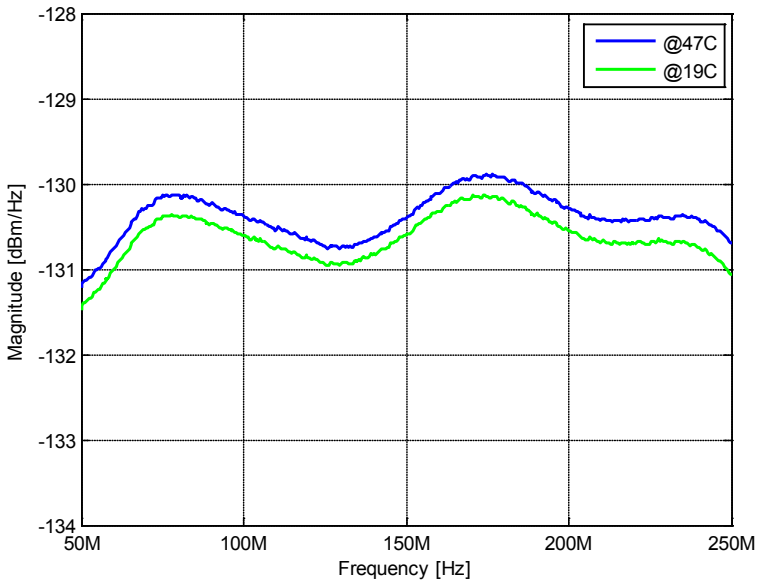

Figure 5-24 Variation of gain module output power spectrum with temperature

5.4 Radiometer Stability Performance

The radiometer minimum detectable temperature is determined by the noise fluctuations appearing at the receiver output. Accordingly, the statistical properties of the detected output voltage from the gain module are measured to evaluate the radiometer stability over time. In this case, the Standard Error of the Mean (SEM) and Allan deviation (ADEV) methods are used as quantitative measures to estimate the uncertainty in the sample mean of the input noise temperature measured by the internal RF detector. The stability test setup is shown in Figure 5-25.

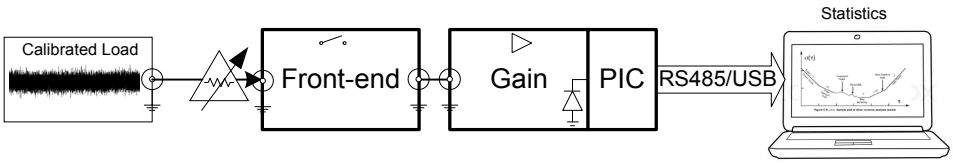

Figure 5-25 Stability Measurement Setup

5.4.1 Standard Error of the Mean

Initially, to determine the accuracy of the sample mean, the standard error of the mean is estimated during measurements. The standard error of the mean represents how well the sample mean approximates the population mean and is estimated by the sample estimate of the population standard deviation divided by the square root of the sample size as (Walker, 1989):

$$SEM_{\bar{x}} = \frac{\sqrt{\frac{\sum_{i=1}^{N}(x_i - \bar{x})^2}{N-1}}}{\sqrt{N}} = \frac{\tilde{s}}{\sqrt{N}} \ . \qquad \text{Eq 5-21}$$

Where N is the sample size, $\bar{x}$ is the average of all of the values, $\tilde{s}$ is the sample standard deviation. The larger the sample, the smaller the standard error and the closer the sample mean approximates the population mean. For a white Gaussian noise, the SEM vs N plotted on a log-log graph is linear with a slope of -0.5. For other types of noise such as low frequency drift noise, the plot starts to deviate from -0.5.

The standard error of the mean is in fact the minimum detectable signal derived from the radiometer equation, Eq 3-3, where the sensitivity, ΔT_n , is the standard deviation of the estimate of the mean, the system noise temperature T_{sys} is the standard deviation of the power fluctuations, and the term $B\tau$ is the number of samples (N).

The point by point plot of the SEM provides a useful measure of the uncertainty in the mean of the input noise temperature graphically and hence radiometer stability. This is a valuable tool while temperature measurements are in progress in the laboratory or in the field environment and was implemented in the analysis routine as shown in Figure 5-26. In this case, the live SEM plot indicates a value under 0.6K after 10k samples (~ 23 hours of integration) for a hot load value of 4108K.

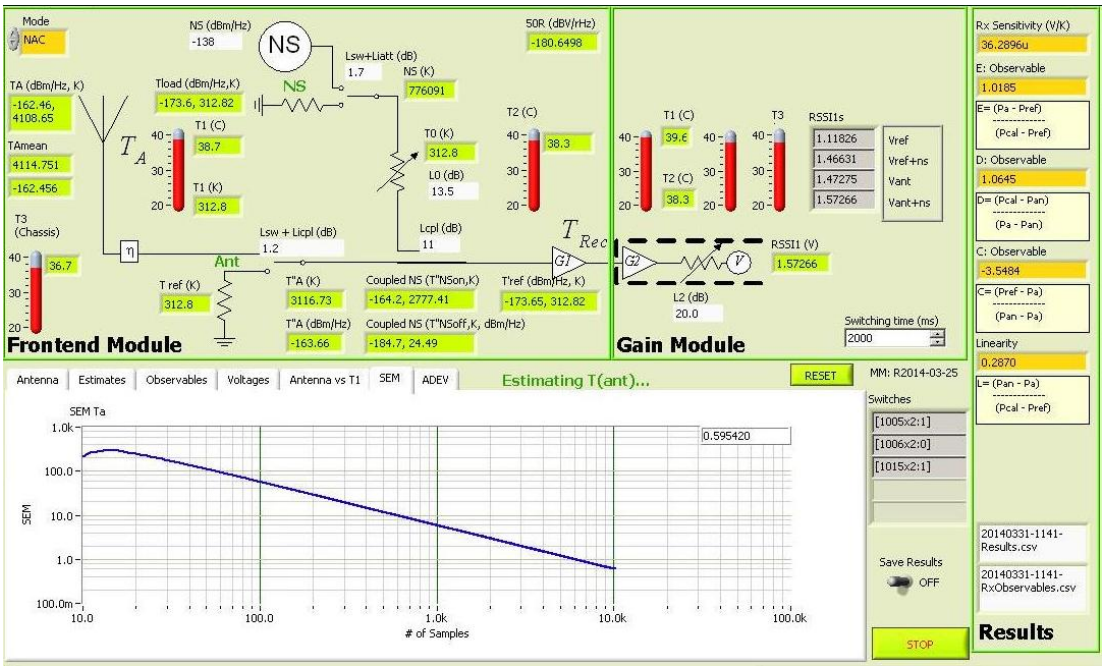

Figure 5-26 Point by point plot of the SEM of the estimated input noise temperature

5.4.2 Allan Deviation

Another measurement of the stability can also be obtained from Allan variance, σ_y^2, and provides the longest integration time, τ, for which the best radiometric sensitivity can be obtained. It is defined as a two sample variance formed by the average of the squared differences between successive values of a regularly measured quantity taken over sampling periods from the measuring interval up to half the maximum measurements time (Allan, 1987):

$$\sigma_{\bar{y}}^2(\tau) = \frac{1}{2}.\frac{\sum_{i=1}^{N-1}\{\bar{y}_{i+1}(\tau) - \bar{y}_i(\tau)\}^2}{(N-1)}, \qquad \text{Eq 5-22}$$

where τ is sampling period of N measurements of y_i for $i=1..N$. The Allan deviation is the square root of Allan variance as follows:

$$ADEV_y = \sigma_y(\tau) = \sqrt{\frac{1}{2}.\frac{\sum_{i=1}^{N-1}\{\bar{y}_{i+1}(\tau) - \bar{y}_i(\tau)\}^2}{(N-1)}}. \qquad \text{Eq 5-23}$$

In radiometric measurements, Allan deviation (or variance) method is useful as it has the ability to identify instabilities of a signal as being white noise, flicker noise or random walk drift. By calculating the Allan deviation for different averaging time, τ, in a log-log plot, these different noise processes can be

identified by the slope of the plot in various time regions as (Land, Levick, & Hand, 2007):

i. A slope of -0.5, ($\tau^{-0.5}$), for Gaussian white noise which is associated with the thermal noise of the system and internal components,
ii. A slope of 0, (τ^{0}), for 1/f flicker noise which may be associated with active components in the radiometer,
iii. A slope of +0.5, ($\tau^{0.5}$), for random-walk noise (low frequency drift noise) which may be associated with short term variations of circuit losses and gains over temperature.

5.4.3 Controlled Measurement Results

In the laboratory controlled environment, the radiometer stability was tested over 12 hours when its input was connected to a known hot reference source, which was a combination of a calibrated high stability noise source (NoiseCom NC3201) and an 18 dB attenuator. The 18 dB attenuator response was measured separately to be equal to 17.4 dB on average within the frequency band. The radiometer components (that is switch losses, coupler losses and internal noise source) were measured and calibrated earlier by using a 50 Ω reference load attached to the input.

The front-end module RF board was stabilised at 35.9 ± 0.2 °C while the gain module RF board was stabilised at 36.6 ± 0.2 °C. The receiver parameters were then monitored over time by logging the four output voltages, $V_{Ref}, V_{Cal}, V_A, V_{AN}$ measured by the detector for each switch state as well as the three temperature monitors T_1, T_2, T_3 in both the front-end and gain modules. Using the NAC radiometer mode of operation, the hot source noise temperature was estimated at regular intervals over 12-hour period as per Eq 4-21.

Over the last 6 hour period, the input noise temperature, T_a , had a mean of 6778.3 K with a standard error of the mean of ±1.02 K after 12-hour period. The standard error of the mean of the input noise temperature (T_a) was plotted against time in a log-log graph and is shown in Figure 5-27.

The plot shows a linear slope of -0.5 as expected indicating a reduction in the SEM as the number of samples increases over time and reaches its min at 1 K.

The input noise temperature of 6778.3 K indicates a power level of -160.288 dBm/Hz or an ENR of:

$$ENR = -174\frac{dBm}{Hz} + 160.288\frac{dBm}{Hz} - 17.4\,dB \approx 31.1\,dB\,. \qquad \textbf{Eq 5-24}$$

This is consistent with the value of the ENR shown in the NC3201 datasheet at the three spot frequencies of 10 MHz, 100 MHz and 500 MHz.

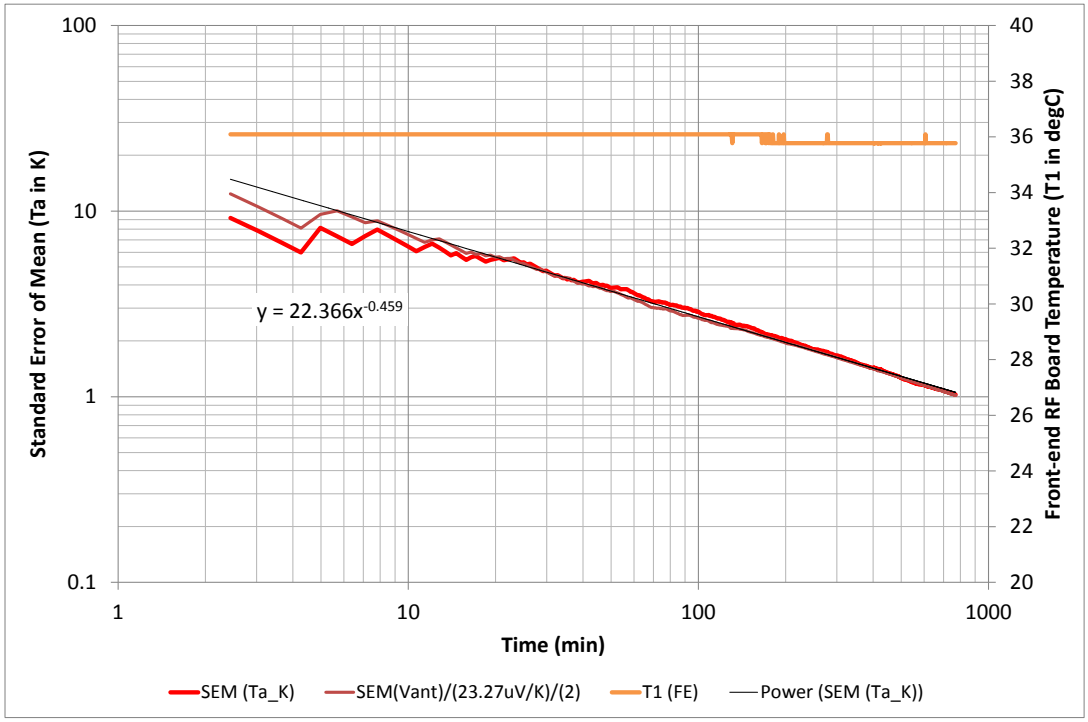

Figure 5-27 Standard error of the mean measured for the input hot source

It should be noted that in the stability measurements shown here, the integration time is fixed for the on-board RF detector (~10 ms). As such, the post-detection integration period is (unlike a traditional radiometer) non-continuous.

The Allan deviation was also plotted in a log-log graph against averaging time, τ, in 5 min intervals. The red trace indicates the Allan deviation of the antenna temperature measured for the total power mode (i.e. at V_A switch state only) whereas the black trace shows that antenna temperature for the NAC mode as calculated from Eq 4-21. The NAC mode has a slope of -0.5 and the longest integration time.

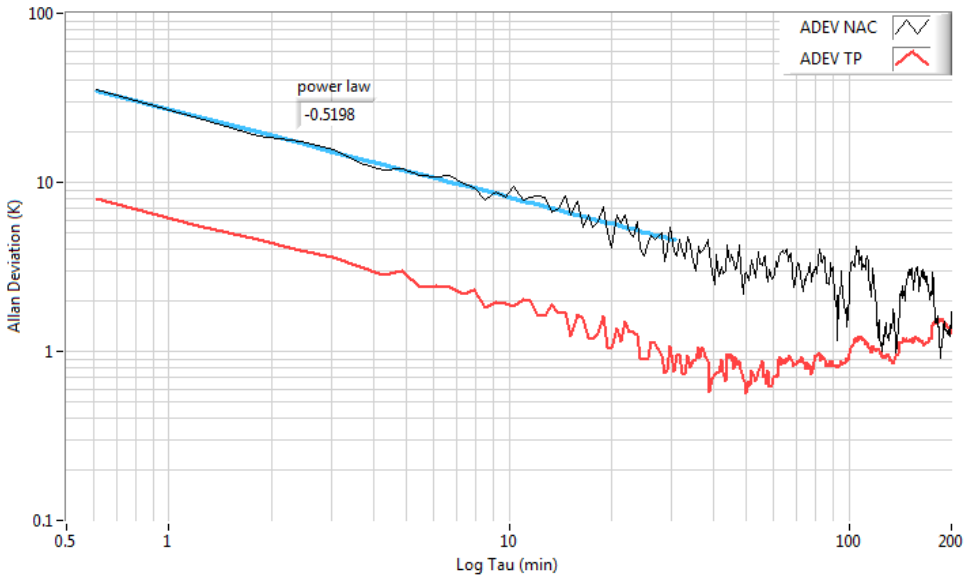

Figure 5-28 Allan deviation of NAC vs TP Mode in a controlled temperature environment

In calculating the input noise temperature, the NAC radiometer uses E ratio which does not depend on the G, T_{rec} and it can be seen that it is stable over a longer averaging time of more than 100 min and was still decreasing compared to the TP mode of only ~30min.

5.4.1 Room Temperature Measurement Results

In this case, a similar setup was carried out when the receiver modules were connected back to back with a reference hot load at the antenna input and sampled at 8 sec intervals while subjected to the room temperature drifts. Both the hot source and modules were allowed to drift over a day in the room.

The input noise temperature was calculated based on the previously measured receiver gain sensitivity of 29uV/K and voltages (i.e. V_A) measured at the output of the detector at regular intervals. As room temperature changed from 34.6 ºC to 36.4 ºC, the mean input noise temperature measured drifted from 5962K to 5984K as shown in Figure 5-29, indicating 12 K/ºC thermal drift due to physical temperature change inside the receiver enclosures.

It can be seen that the input noise temperature measured by the radiometer (based on the V_A detected voltage) follows the room temperature drift over time as expected.

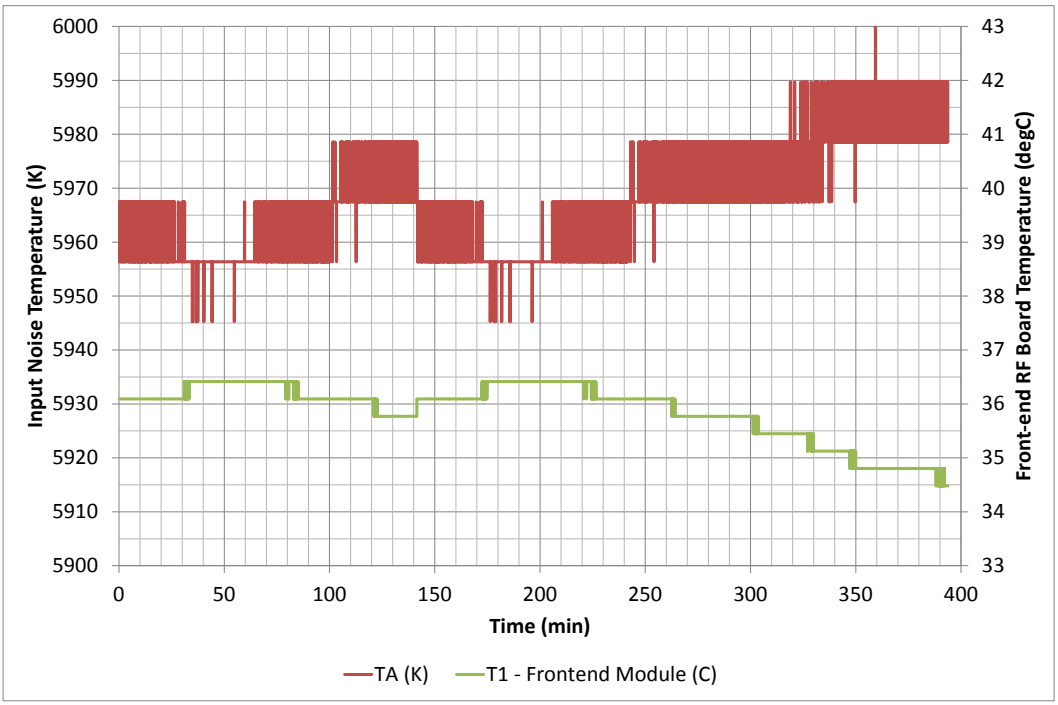

Figure 5-29 Measured input noise temperature drift in TP mode

The Allan deviation, in this case, plotted in a log-log graph against averaging time, τ, shows a lowest value ($\sigma_y(\tau) \sim 0.9K$) at averaging time of 1 min as shown in Figure 5-30. On the plot, the slope of -0.45 identifies a region of largely Gaussian noise, the slope of +0.7 shows a temperature drift component merging with the Gaussian noise which predominates above 3 min averaging time.

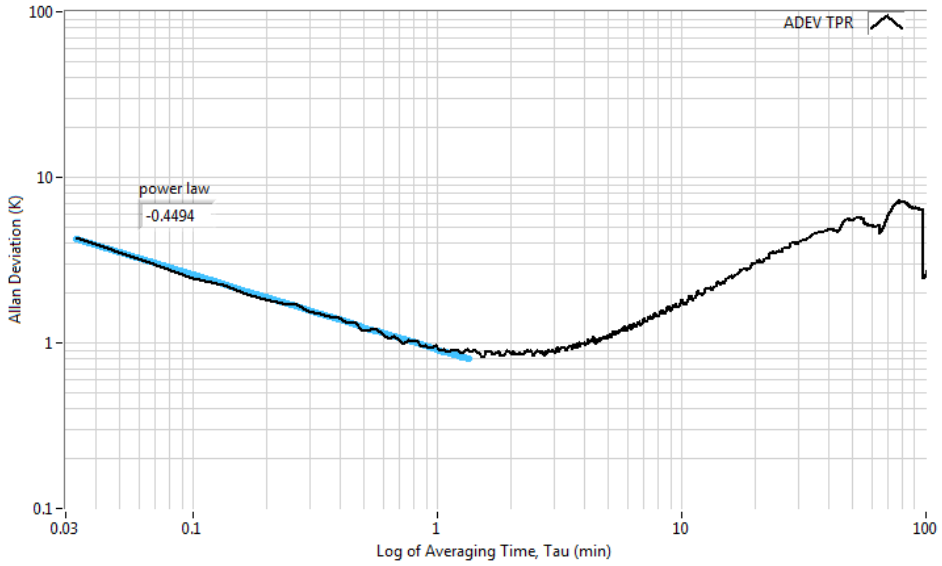

Figure 5-30 Allan deviation of the hot load for the TP Mode in the room

For the case of NAC mode, the input noise temperature was calculated based on the voltage ratio in each state and Eq 4-21. As room temperature changed from

36.4 ºC to 38.3 ºC, the mean input noise temperature measured drifted from 4114 K to 4118 K as shown in Figure 5-31, indicating 2 K/ºC thermal drift due to physical temperature change inside the receiver enclosures.

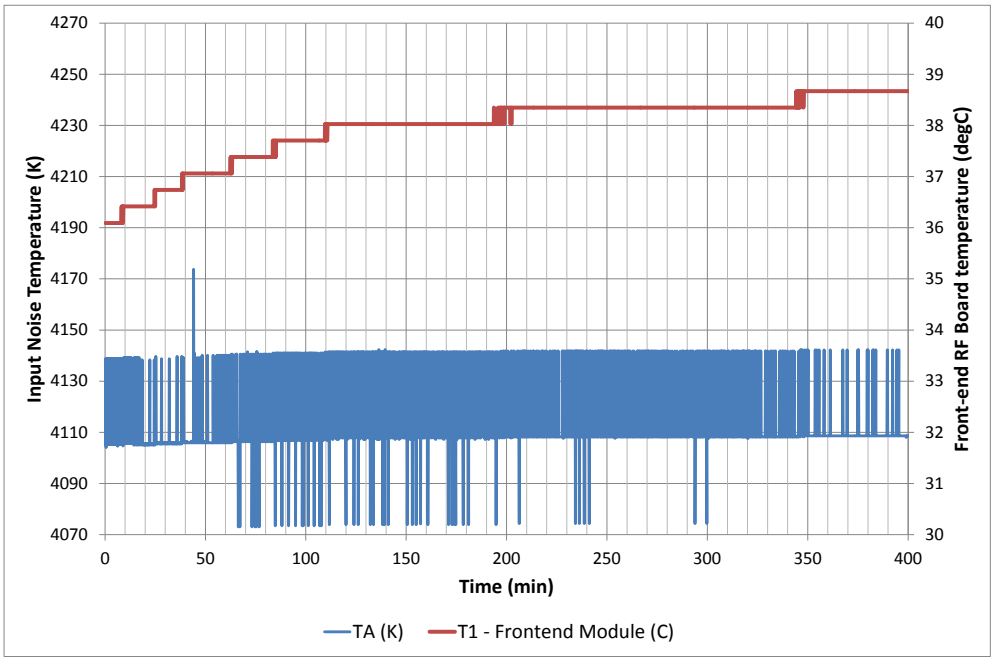

Figure 5-31 Measured input noise temperature drift in NAC mode

The Allan deviation plotted in a log-log graph against averaging time, τ, shows a lowest value ($\sigma_y(\tau) \sim 1.8K$) at averaging time of 6 min as shown in Figure 5-32 and beyond that 1/f noise and drift noise dominate.

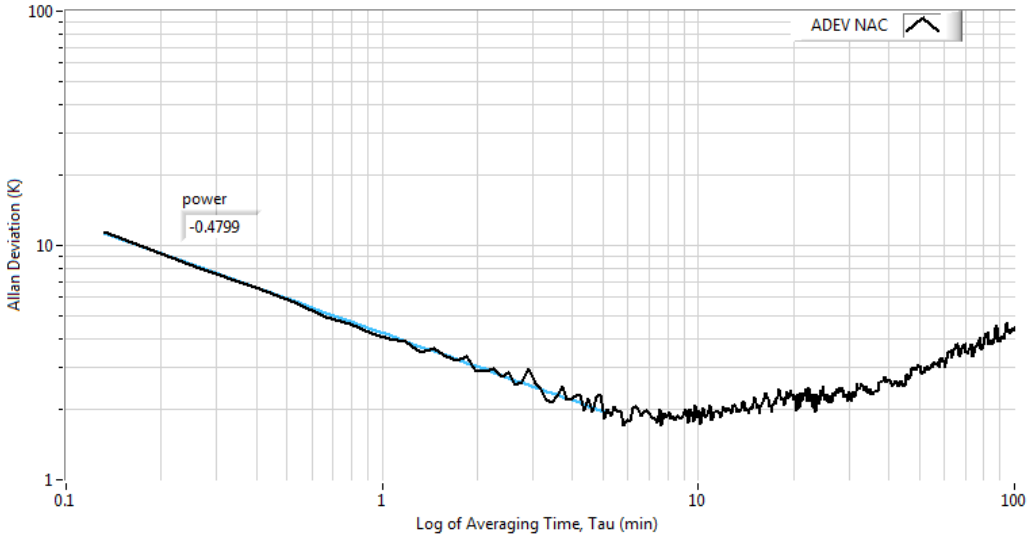

Figure 5-32 Allan deviation of the hot load for the NAC Mode in the room

5.5 Discussion of Results

Thermal tests of individual radiometer components such as internal noise source, amplifier, coupler, RF switches have been conducted successfully in the laboratory. It was found that each component has nearly linear temperature sensitivity with negative temperature coefficients in the range of 0.0026 dB/ºC for the front-end input components, to 0.026 dB/ºC for the internal calibrated noise source.

In practice, the results establish some bounds within which the radiometer may remain stable in the presence of time varying temperature gradients as seen from the Allan deviations plots. Assuming the radiometer is operating in an environment in which the temperature changes slowly, the application of linear corrections, as suggested in section 5.3, based on calibration at two different temperatures should enable measured quantities to be corrected for temperature changes up to the accuracy dictated by the measurement equipment. Enclosing the radiometer front-end components in a 2kg aluminium enclosure, as implemented in this project, dampens any fast varying temperature fluctuations to a minimum.

External (i.e. outside of the front-end enclosure) effects such as antenna mismatch and interconnecting cable loss between the antenna and receiver front-end input would also introduce noise errors. As such, corrections would need to be made for the noise contributed by these effects. For the case of a single reflection due to antenna mismatch and the cable loss, L_c, the antenna temperature seen at the receiver front-end connector, T_{AR}, would be:

$$T_{AR} = (1 - |\Gamma|^2)\left[\frac{T_A}{L_c} + \left(1 - \frac{1}{L_c}\right)T_p\right], \qquad \textbf{Eq 5-25}$$

where T_A is the antenna temperature at the antenna terminals, T_p is the physical temperature of the interconnecting cable of loss L_c and Γ is the antenna reflection coefficient.

Eq 5-25 indicates that when the mismatch loss is significant, the antenna temperature is reduced by the impedance mismatch loss. However, in the case of a well matched system when $(1 - \Gamma^2) \sim 1.00$ and a low loss factor, when $L_c \sim 1.00$, the antenna temperature seen at the front-end connector, T_{AR} , closely resembles the true antenna temperature, $T_{AR} \sim T_A$.

In a more complex scenario with multiple reflections due to additional impedance mismatch interactions between the broadband antenna (interconnecting cables and balun if used) and the receiver front-end, further measurements and calibration steps would be required to determine the true antenna temperature. As these mismatches change the effective receiver noise temperature, due to additional reflected noise bouncing back and forth at the antenna input, additional corrections need to be performed as suggested by Rogers and Bowman (2012) using noise wave analysis with a vector network analyser.

CHAPTER 6

6 Conclusion

The primary focus of this thesis was to design and develop a flexible and portable low noise sensitive radiometric receiver. This receiver may be employed in the BIGHORNS epoch of reionisation experiment to measure the sky averaged spectrum for detection of the red-shifted 21 cm global signal. Extrapolating the measured receiver results indicates that to achieve under 50 mK resolution, as discussed in section 3.8.2., a successful measurement requires at least 9 days of observation, neglecting daylight observations.

6.1 Project Summary

In summary, the contributions in this project include:

1. A successful design and development of a multi-configurable radiometric receiver consisting of a front-end module and a high gain module working in the frequency range 50-250 MHz.
2. A multi-mode receiver which can operate as a total power, noise adding or noise adding comparison radiometer with the initial implementation as a noise adding comparison radiometer.
3. The derivation of the antenna temperature and radiometer resolution equations for a noise adding comparison radiometer.
4. A very detailed evaluation of the RF performance of the radiometer and its major components as a function of frequency and temperature.
5. The derivation of the models for the frequency response and temperature characteristics of the front-end module, which is essential for data analysis in the BIGHORNS system, and improving final system sensitivity for long observation times (in days).
6. Tests of radiometer stability using the standard error of the mean and the Allan deviation have also been carried out over a number of hours in the laboratory. In the case of a hot load input connected to the radiometer and both subjected to a room temperature drift, the Allan deviation was about 1.8 K for an integration time of 6 min before it started to drift.

The table below shows a final summary of the receiver parameters based on the measured results.

Table 7 Summary of the receiver parameters

Parameter	Value
Receiver noise temperature	214 K (NF~2.4) between 50-250 MHz
Theoretical radiometric resolution, ΔT_t , for BW=100 kHz and τ=2 hrs	~50 mK @ T_a = 300 K ~510 mK @ T_a = 5000 K
Measured radiometer resolution using internal detector (τ~10 ms), ΔT_m	1.02 K @ T_{hot} = 6778 K
Radiometric range	50-5000 K
Gain module temperature coefficient	0.009 dB/ºC
Front-end module temperature coefficient	0.02 dB/ºC
Front-end Dicke switching rate	0 to 65535 in 0.25sec step
RS485 communication data rate	32kbps
Instrument control and monitor	x3 Temperature sensors: T1, T2, T3 x1 Humidity sensor: H Voltage and Current monitors Receiver gain adjustment Radiometer noise injection adjustment
Input DC voltage	15 to 18V
Current consumption (Front-end and gain modules)	< 700 mA @ 15V
1 dB Bandwidth	Front-end module: 50 – 250 MHz Gain module: 50 – 250 MHz
Gain flatness (50 – 250 MHz)	Front-end module: 36.4 ± 0.6 dB Gain module: 41.5 ± 0.5 dB

6.2 Concluding Remarks

The results of the receiver tests showed that the insertion loss variations and temperature effects related to the input components are significant factors that may cause unpredictable power fluctuations and would affect the stability required for long integration time to detect the EoR global signal. As such the placement of the receiver front-end enclosure as close to the antenna as possible is critical. This level of measurement accuracy would also require temperature monitoring of the critical elements in the receiver front-end (such as the LNA, load and noise source references) in order to account for variations. In this case, as the receiver front-end is confined to a physically small area, that uses small surface mount components (such as 1206 SMD 50 Ω reference resistor and an SMD noise diode) compared with

connectorised parts, temperature measurements of the input components are relatively easier to be monitored and used for compensation during post processing.

In addition, the frequency and temperature responses of the key components of the receiver that were measured and characterised are shown in chapter 5. The BIGHORNS system can, later on, make use of the temperature sensor data from the receiver module. The power spectra which are captured by the back-end data acquisition need to take these effects into account to extract sky temperature and achieve lower resolution. This is required to correct for the frequency and temperature dependent effects (such as diurnal atmospheric thermal fluctuations) that cannot be calibrated out. Based on the temperature variations monitored, and knowing the temperature effects of the radiometer components as derived in chapter 5, realistic corrections and normalisation can be applied to the power spectra during post processing and data analysis to further improve the receiver stability.

Based on the receiver internal RF detector used in the gain module to measure the antenna temperature, the sensitivity was limited by the resolution of the detector and 10-bit ADC in the microcontroller to be statistically 1.02 K. The BIGHORNS back-end data acquisition and spectrometer can be used later on to measure the radiometer sensitivity using the power spectra within the frequency range. This requires careful calibration of the BIGHORNS system as a whole, which was not within the scope of this thesis.

Moreover, the BIGHORNS system needs to take into account other effects such as antenna balun loss and digitiser nonlinearities. When testing in an outside environment, radio frequency interference (RFI), effects of the Sun, atmospheric conditions, surrounding objects and other human generated interferences need to also be taken into account. Surrounding objects such as trees and hills where the antenna gain is reduced drastically would also affect the measurements. Atmospheric conditions exhibit diurnal temperature variations which might affect the measurements some of the time during the year. RFI, in particular television and FM radio stations are major noise contributors in a field experiment, which makes this kind of experiment extremely challenging. As a result, site selection is a crucial step towards reducing RFI. An FM radio transmitter, in particular, could introduce hundreds of K noise temperature, at 100km from the observation site. A number of

field trips have been scheduled to search for an extremely remote RFI quiet site by ICRAR personnel.

6.3 Future Experiments

Further testing and calibration in a controlled laboratory environment using a digital spectrometer is required to measure the output power spectra over the discrete frequency ranges, rather than the averaged signal using the on-board detector in the receiver. In this case, other external factors and systematic uncertainties such as resolution of the data acquisition, its reference clock timing jitter, and stability of the spectrometer itself should also be considered. Other systematic errors may well be discovered during field trips which need to be mitigated by careful modifications to the RF components.

Extra enhancement to the receiver hardware may be carried out by replacing the 10 dB input coupler by a 20 dB coupler to reduce input insertion loss by approximately 0.4 dB, and consequently lowering total noise temperature from 345 K (refer to section 5.1.5) to 290 K. This would improve the receiver sensitivity at frequencies above 140 MHz where the receiver noise temperature is expected to be comparable to the sky temperature (refer to Figure 2-9).

In addition, using an active temperature control circuitry and a software compensation knowing the physical temperature at different points of the radiometer enclosure would help minimise these temperature effects. This active temperature control circuitry has been built into the controller board using a Peltier device but had not been implemented for this project.

Finally another desirable facility worth looking at is the ability to switch to short and open calibrated references, as well as a $50\,\Omega$ termination (Dicke switching), to measure antenna reflections in situ and in real time and then calibrate them out from the system response. This is similar to a network analyser port calibration using calibrated references. The reflection calibration may be applied in situ at certain intervals or as required during the measurement.

APPENDICES

7 Appendices

7.1 Appendix A: Derivation of a noise adding comparison (NAC) radiometer sensitivity

In this appendix the radiometric resolution of the noise adding comparison radiometer is derived. A model for such a radiometer is shown in Figure 7-1. The output power of the radiometer is a function of radiometer states. In the case of NAC radiometer, the output power of each state includes a fluctuating component, δ, arising from the stochastic nature of the signal at the receiver input and instabilities within the receiver. The random term is a small fraction of the expected value and is assumed to be modelled as an additive zero mean random Gaussian variable: $P_i = P_i(1 + \delta_i)$.

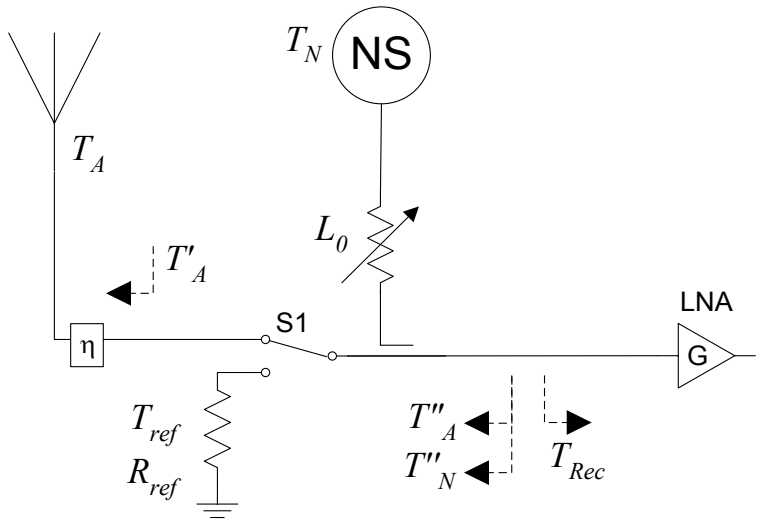

Figure 7-1 NAC radiometer

The output power in each state can be written as follows:

$$P_{Ref} = \left(T'_{Ref} + T_{Rec}\right)(1 + \delta_r)\kappa BG\,, \quad \textbf{Eq 7-1}$$

$$P_{Cal} = \left(T'_{Ref} + T''_N + T_{Rec}\right)(1 + \delta_c)\kappa BG\,, \quad \textbf{Eq 7-2}$$

$$P_A = (T''_A + T_{Rec})(1 + \delta_a)\kappa BG, \quad \textbf{Eq 7-3}$$

where δ_a, δ_r and δ_n correspond to noise fluctuation in the antenna, reference and calibration noise respectively, assumed to be . The voltage ratios can then be written as:

$$E = \frac{P_A - P_{Ref}}{P_{Cal} - P_{Ref}}. \qquad \textbf{Eq 7-4}$$

The estimate of the antenna temperature at the input of the LNA, $\hat{T}"_A$, can be derived from:

$$\hat{T}"_A = T"_N E + T'_{Ref}\ . \qquad \textbf{Eq 7-5}$$

Substituting into Eq 7-5 and removing the gain factors, gives:

$$\hat{T}"_A = \qquad \textbf{Eq 7-6}$$

$$= T"_N \frac{(T"_A + T_{Rec})(1+\delta_a) - (T'_{Ref} + T_{Rec})(1+\delta_r)}{(T'_{Ref} + T"_N + T_{Rec})(1+\delta_c) - (T'_{Ref} + T_{Rec})(1+\delta_r)}$$

$$+ T'_{Ref},$$

Then expanding and simplifying, the above can be written as:

$$\hat{T}"_A = T"_N \frac{(T"_A - T'_{Ref}) + (T"_A + T_{Rec})\delta_a - (T'_{Ref} + T_{Rec})\delta_r}{T"_N + (T'_{Ref} + T"_N + T_{Rec})\delta_c - (T'_{Ref} + T_{Rec})\delta_r} \qquad \textbf{Eq 7-7}$$

$$+ T'_{Ref},$$

Factoring out $T"_N$ from the numerator and denominator results in:

$$\hat{T}"_A = \frac{(T"_A - T'_{Ref}) + (T"_A + T_{Rec})\delta_a - (T'_{Ref} + T_{Rec})\delta_r}{1 + \left(\frac{T'_{Ref} + T"_N + T_{Rec}}{T"_N}\right)\delta_c - \left(\frac{T'_{Ref} + T_{Rec}}{T"_N}\right)\delta_r} \qquad \textbf{Eq 7-8}$$

$$+ T'_{Ref}\ .$$

Using small signal approximation $\left(\frac{1}{1-\varepsilon}\right) \cong 1 + \varepsilon$, the estimate of the antenna temperature at the input to the LNA can be written as:

$$\hat{T}"_A \cong \{(T"_A - T'_{Ref}) + (T"_A + T_{Rec})\delta_a - (T'_{Ref} + T_{Rec})\delta_r\} \qquad \textbf{Eq 7-9}$$

$$* \left\{1 - \left(\frac{T"_N + T'_{Ref} + T_{Rec}}{T"_N}\right)\delta_c + \left(\frac{T'_{Ref} + T_{Rec}}{T"_N}\right)\delta_r\right\}$$

$$+ T'_{Ref}\ .$$

Since the random terms are assumed to be much smaller than 1, the first order terms may only be retained, and the above can be simplified to:

$$\hat{T}''_A \cong \left(T''_A - T'_{Ref}\right) - \left(T''_A - T'_{Ref}\right)\left(1 + \frac{T'_{Ref} + T_{Rec}}{T''_N}\right)\delta_c \qquad \textbf{Eq 7-10}$$

$$+\left(T''_A - T_{Ref}\right)\left(\frac{T'_{Ref} + T_{Rec}}{T''_N}\right)\delta_r + \left(T''_A + T_{Rec}\right)\delta_a$$

$$-\left(T'_{Ref} + T_{Rec}\right)\delta_r + T'_{Ref}\,.$$

Simplifying:

$$\hat{T}''_A \cong T''_A + \left(T''_A + T_{Rec}\right)\delta_a \qquad \textbf{Eq 7-11}$$

$$-\left(T''_A - T'_{Ref}\right)\left(1 + \frac{T'_{Ref} + T_{Rec}}{T''_N}\right)\delta_c$$

$$+\left(T'_{Ref} + T_{Rec}\right)\left(\frac{T''_A - T'_{Ref}}{T''_N} - 1\right)\delta_r\,.$$

Eq 7-11 shows the estimate of the antenna temperature at the input to the LNA plus three error terms. The radiometric resolution can then be estimated as the quadratic sum of the components of the error terms in Eq 7-11 as:

$$\Delta T_{rms} = \sqrt{\left(T''_A + T_{Rec}\right)^2\delta_a} \qquad \textbf{Eq 7-12}$$

$$+\sqrt{\left(T''_A - T_{Ref}\right)^2\left(1 + \frac{T'_{Ref} + T_{Rec}}{T''_N}\right)^2\delta_c}$$

$$+\sqrt{\left(T'_{Ref} + T_{Rec}\right)^2\left(\frac{T''_A - T_{Ref}}{T''_N} - 1\right)^2\delta_r}\,.$$

Assuming equal integration times and independent noise contribution in each state of the switches, fractional noise in each switch position is:

$$\delta_a = \delta_c = \delta_r = \sqrt{\frac{1}{B(\tau/3)}}. \qquad \textbf{Eq 7-13}$$

The radiometric resolution is then:

$$\Delta T_{rms} = \sqrt{\frac{1}{B(\tau/3)}}\sqrt{\left(T''_A + T_{Rec}\right)^2} \qquad \textbf{Eq 7-14}$$

$$+\sqrt{\frac{1}{B\tau/3}}\sqrt{\left(T''_A - T'_{Ref}\right)^2\left(1+\frac{T'_{Ref}+T_{Rec}}{T''_N}\right)^2}$$
$$+\sqrt{\frac{1}{B\tau/3}}\sqrt{\left(T'_{Ref}+T_{Rec}\right)^2\left(\frac{T''_A - T'_{Ref}}{T''_N}-1\right)^2}\,.$$

If $T''_N \gg T'_{Ref}$ the radiometer sensitivity can be simplified to:

$$\Delta T_{rms} = \sqrt{\frac{(T''_A + T_{Rec})^2 + \left(T''_A - T'_{Ref}\right)^2 + \left(T'_{Ref}+T_{Rec}\right)^2}{B(\tau/3)}}. \qquad \textbf{Eq 7-15}$$

7.2 Appendix B: The Receiver Circuit Diagrams

The receiver front-end PCB layouts of the top and bottom side of the RF board are shown in Figure 7-2 and Figure 7-3 respectively below. The 3D views show both chain 1 and chain 2 arms of the RF board including the two internal noise sources and four relay switches. In this project, the top chain (CH1) of the RF board including one noise source has been enabled and discussed. The bottom side view shows the ground patches where the heat sinks have been attached for the low noise amplifiers. The receiver front end module top level schematic diagram of the RF board is shown in Figure 7-4.

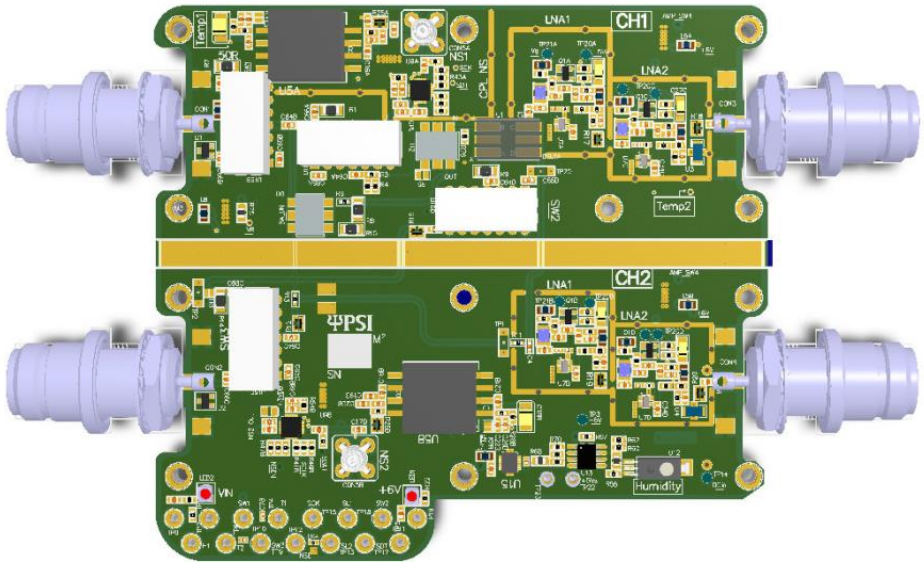

Figure 7-2 The front-end module RF board 3D view - top side

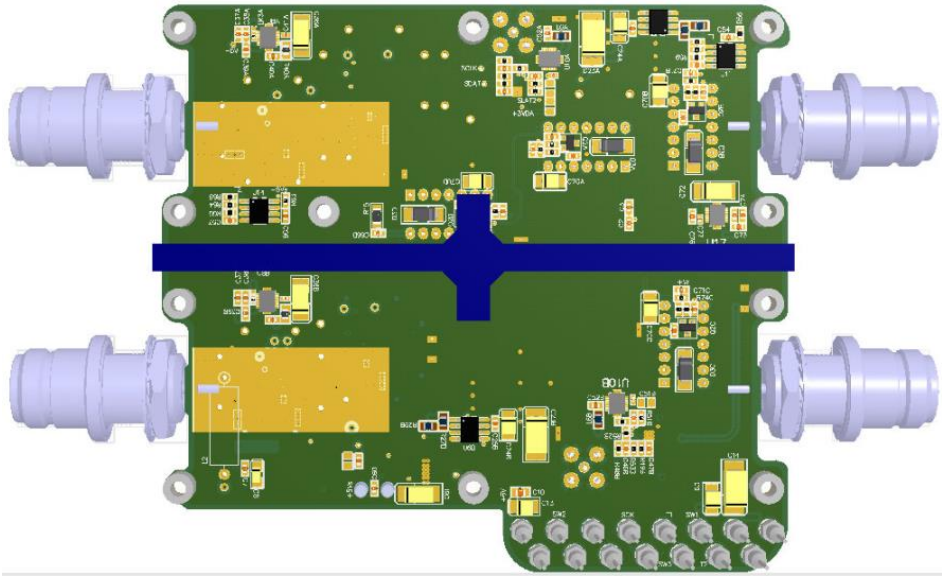

Figure 7-3 The front-end module RF board 3D view - bottom side

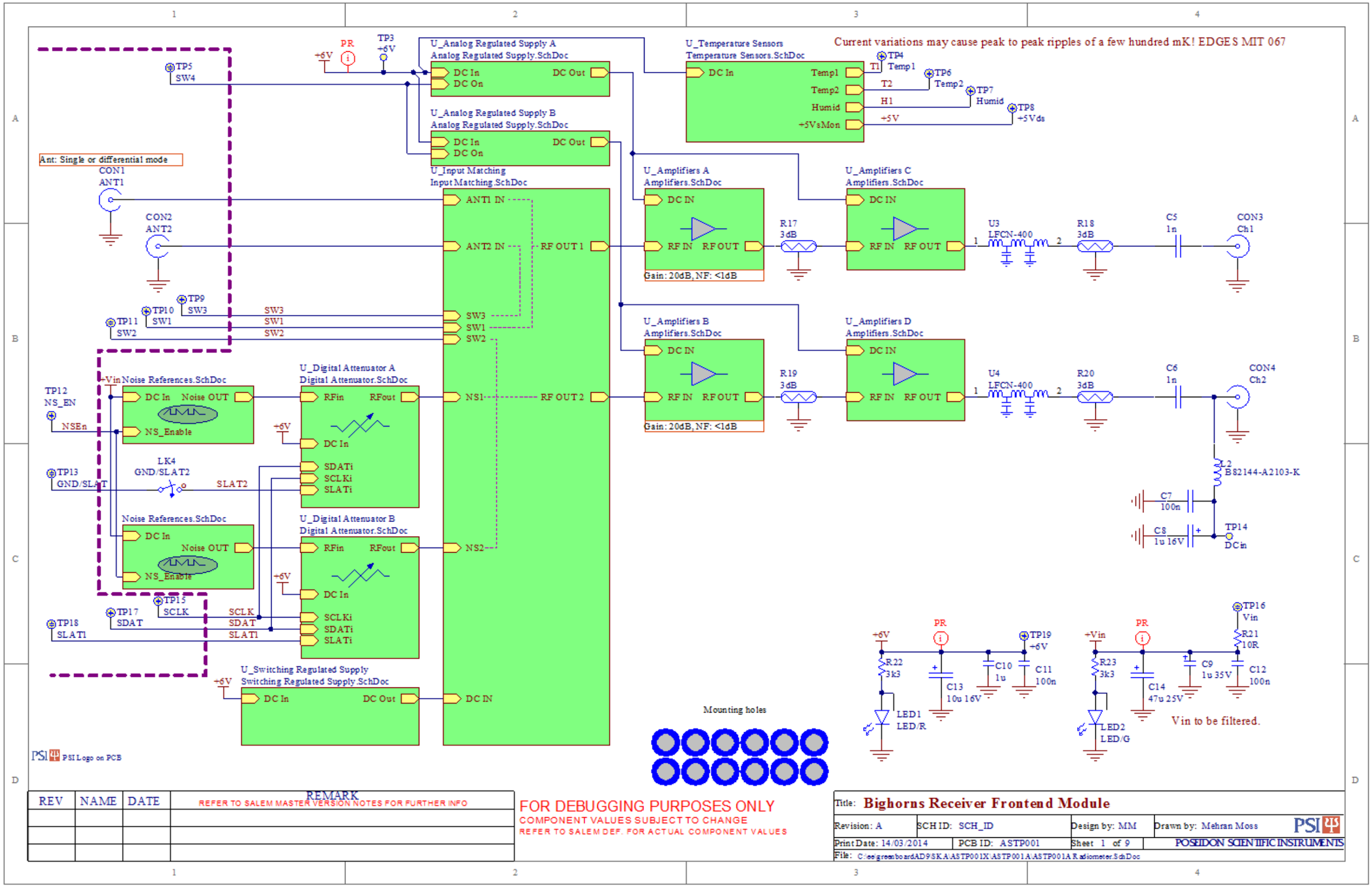

Figure 7-4 The receiver front-end top level schematic diagram

The receiver gain module PCB diagram of the RF board is shown in Figure 7-6 and Figure 7-7.

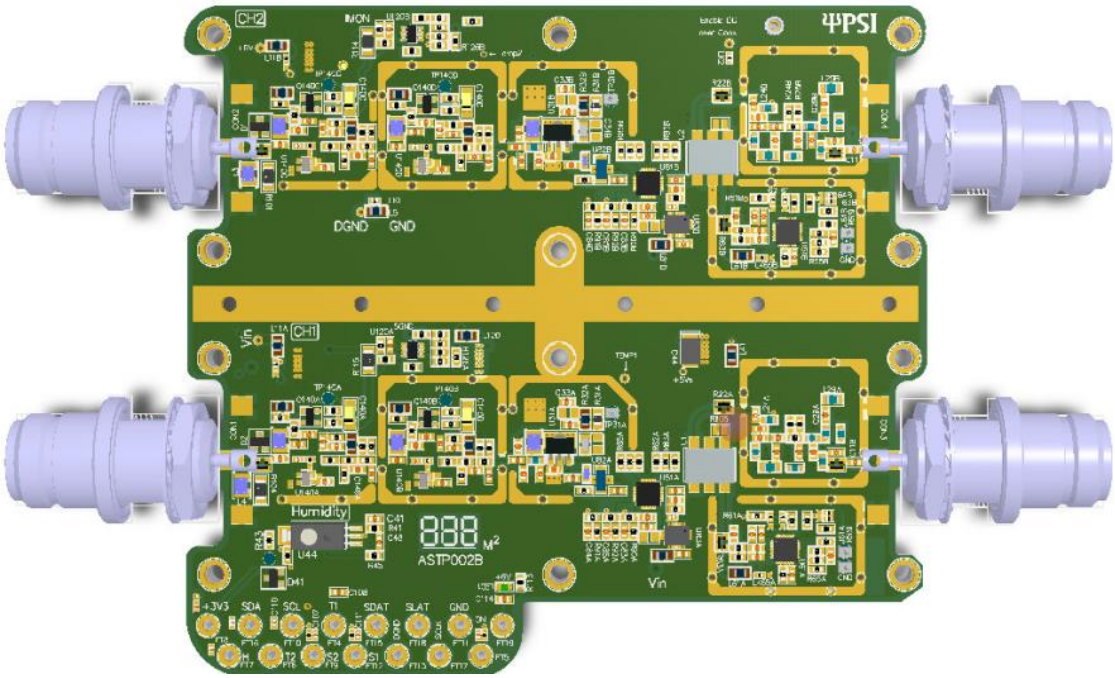

Figure 7-6 The gain module RF board 3D view - top side

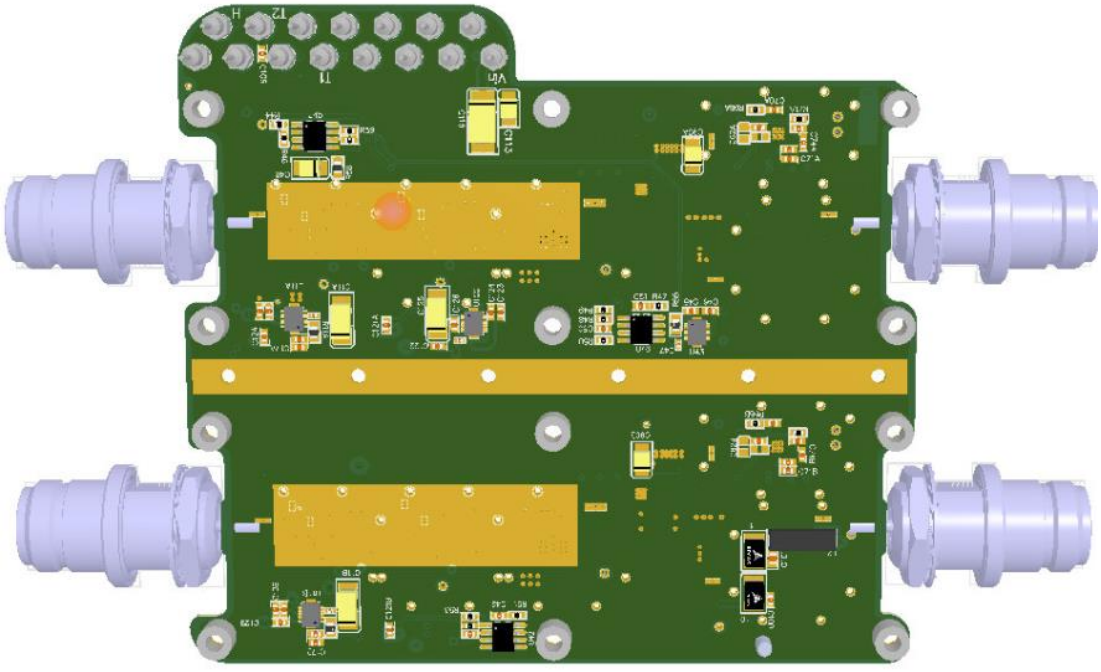

Figure 7-7 The gain module RF board 3D view - bottom side

.

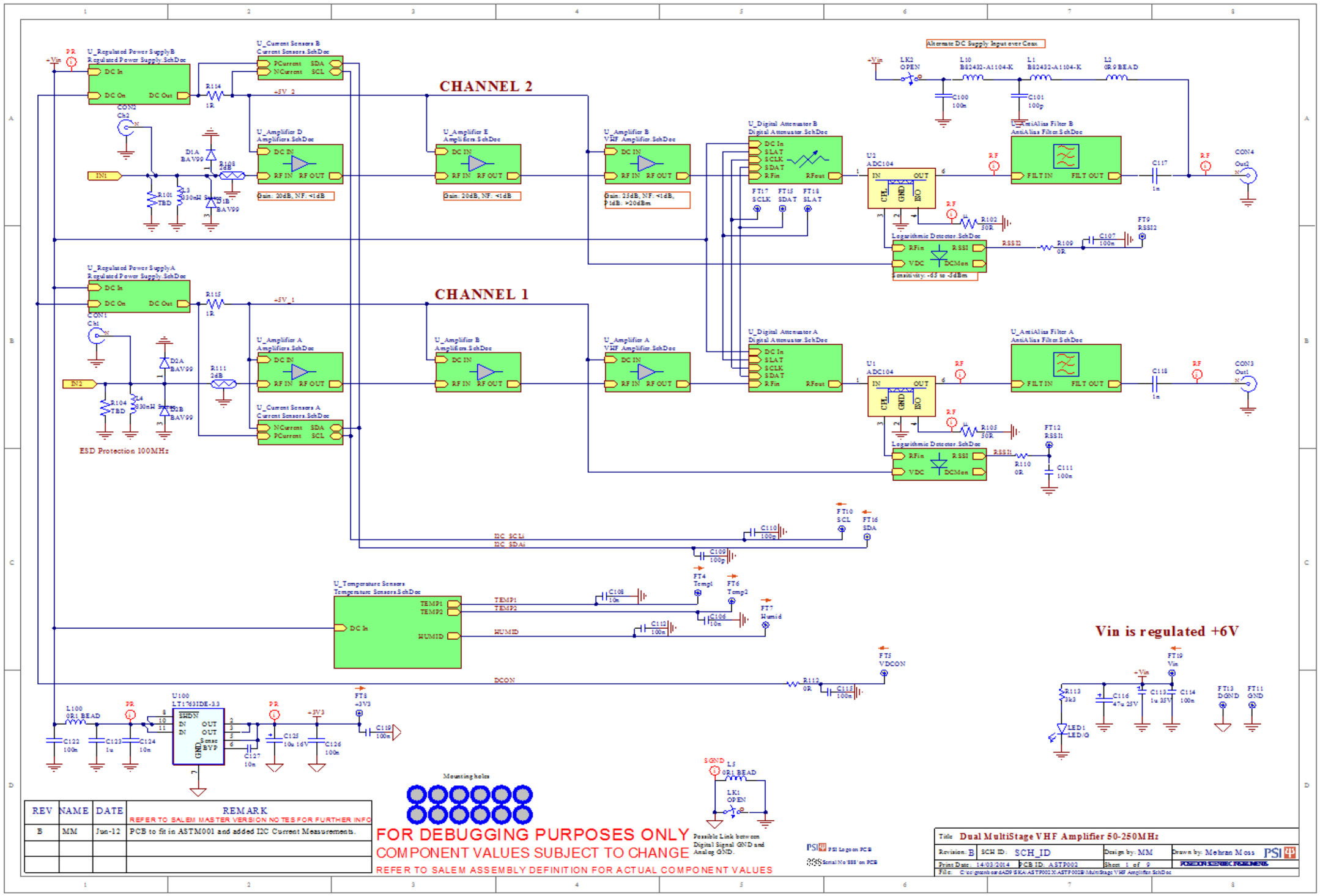

Figure 7-8 The receiver gain module top level schematic diagram

Figure 7-9 and Figure 7-10 show 3D view of the receiver controller PCB diagrams. The 6-pin blue connector (CON2) can be used to program the microcontroller using RS232 protocol. The 3-pin blue connector (CON1) is the RS232 debugging port. The 2-pin black connector (JMP2) is the fan power connector. The 12-pin connector (JMP3) is configuration connector for enabling RS232 debugging port, setting gain or front-end module bit, etc and SW1 resets the PIC. The top level schematic diagram of the controller board in the receiver front-end and gain modules is shown in the next page

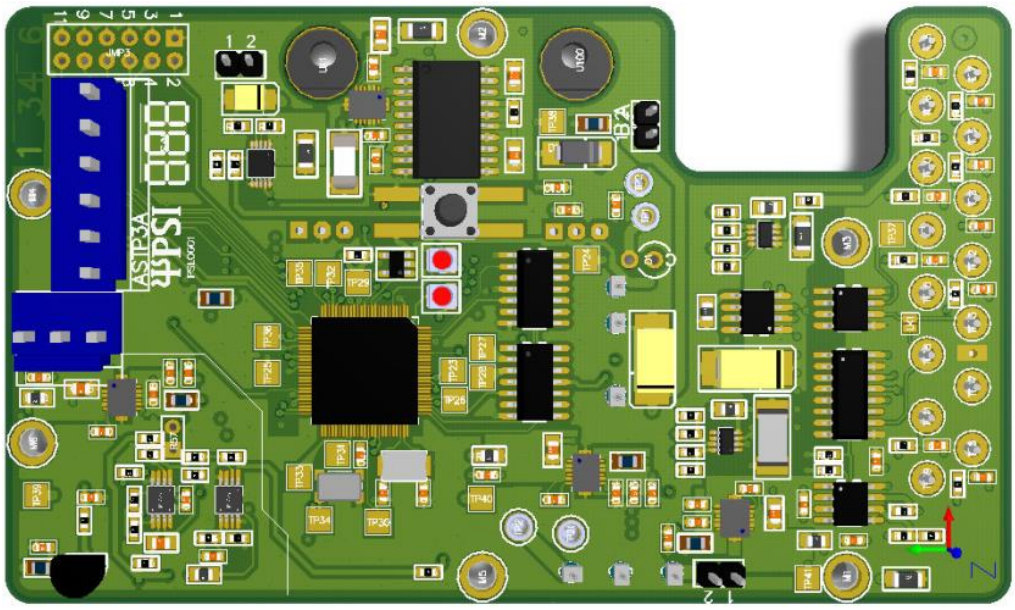

Figure 7-9 The controller board 3D view - top side

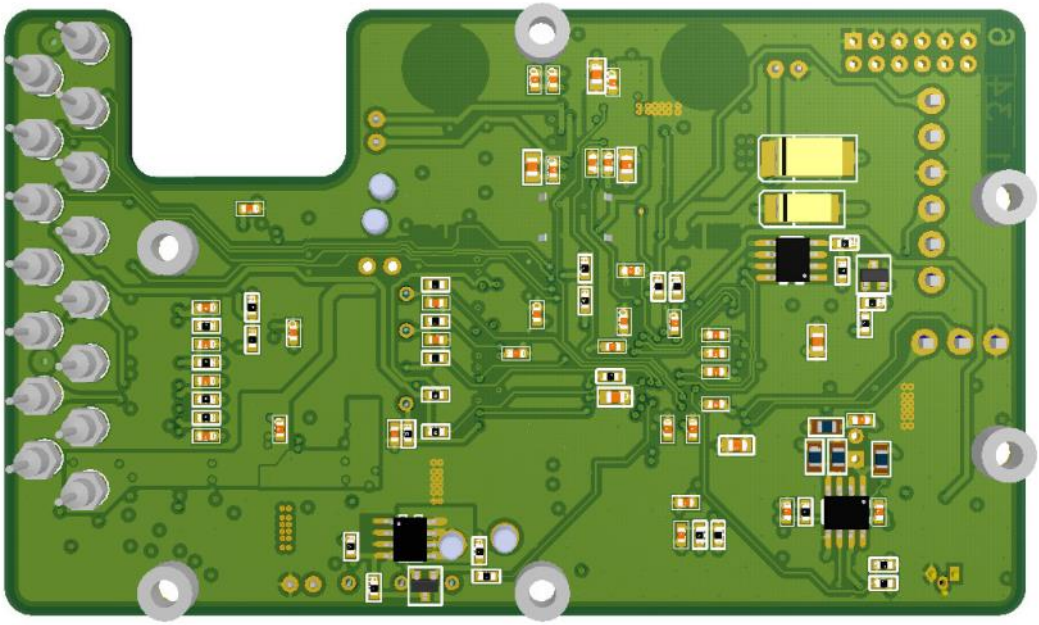

Figure 7-10 The controller board 3D view – bottom side

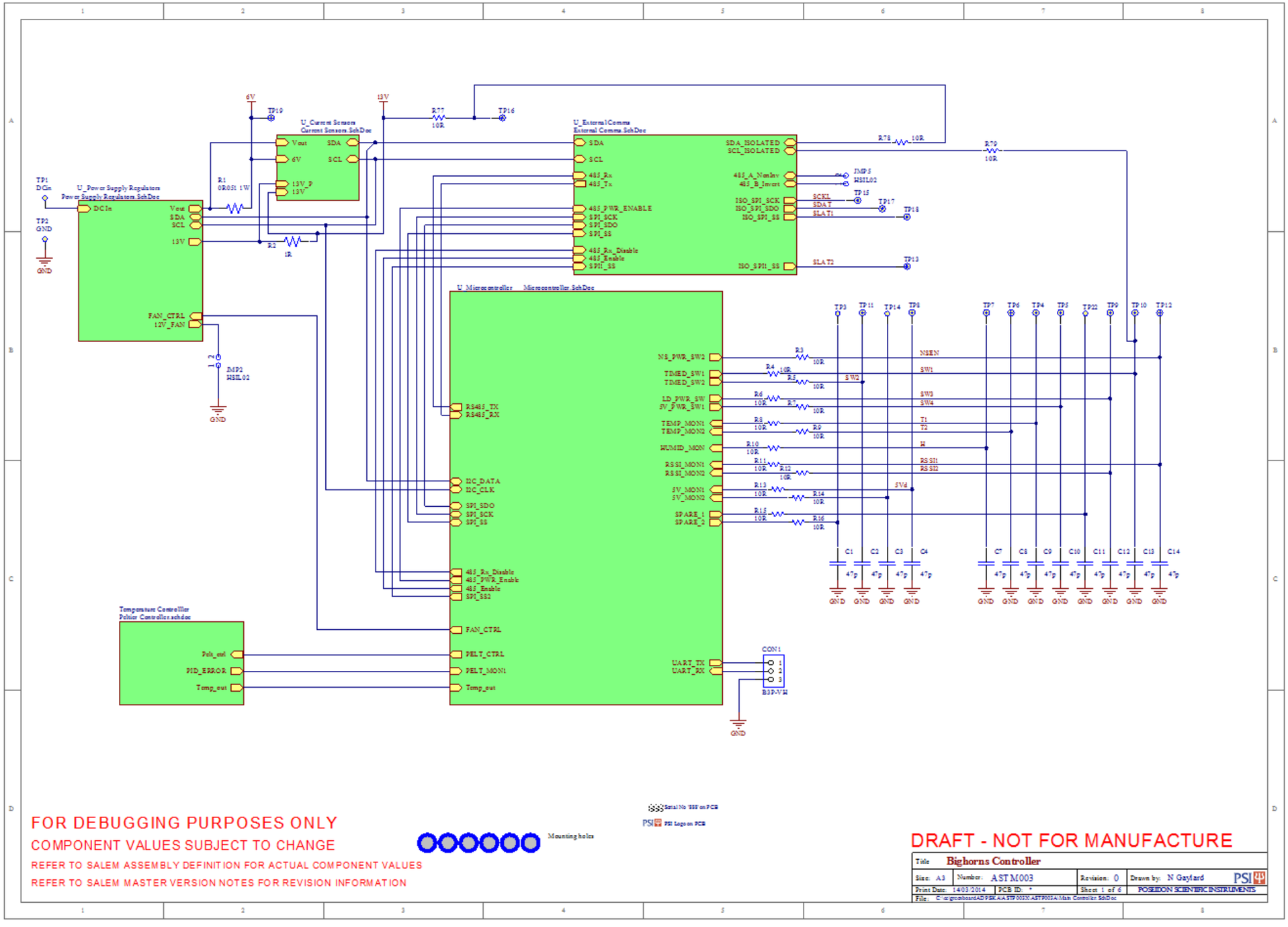

Figure 7-11 The receiver controller top level circuit diagram

Figure 7-12 shows the layout of the feedthrough connectors for the receiver front-end and gain modules as viewed from the RF board side in the receiver enclosure.

Figure 7-12 The feedthrough connection diagram for the receiver RF boards

Lastly, the references MST-0512-SN2 and MST-0512-SN5 in figure captions refer to the built front-end serial number 2 and gain module serial number 5 assemblies respectively.

7.3 Appendix C: MATLAB/LabVIEW Source Codes

LabVIEW codes have been written under Windows 7 environment to estimate the Allan deviation and the standard error of the mean from the measured data. The block diagrams of the codes are shown in Figure 7-13 and Figure 7-14.

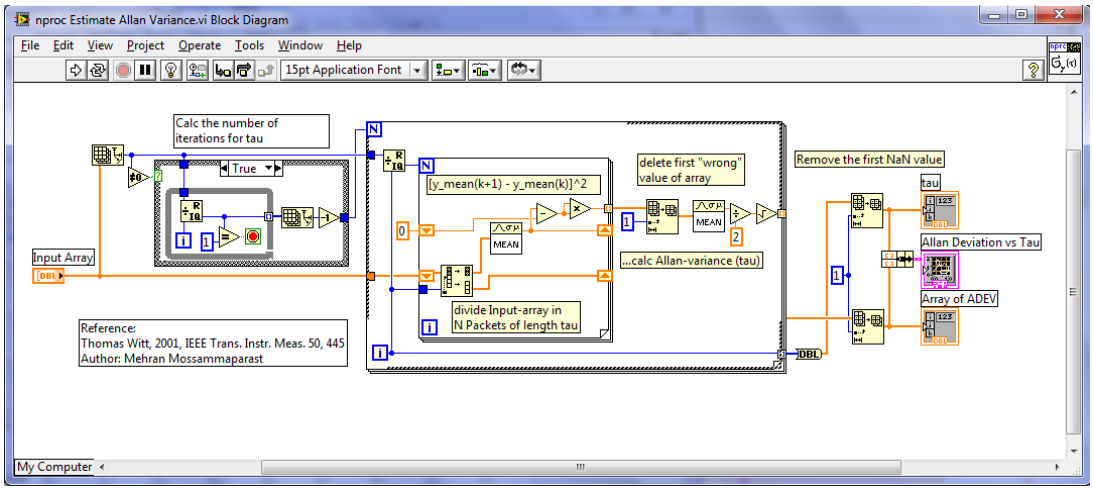

Figure 7-13 LabVIEW block diagram of the Allan deviation code

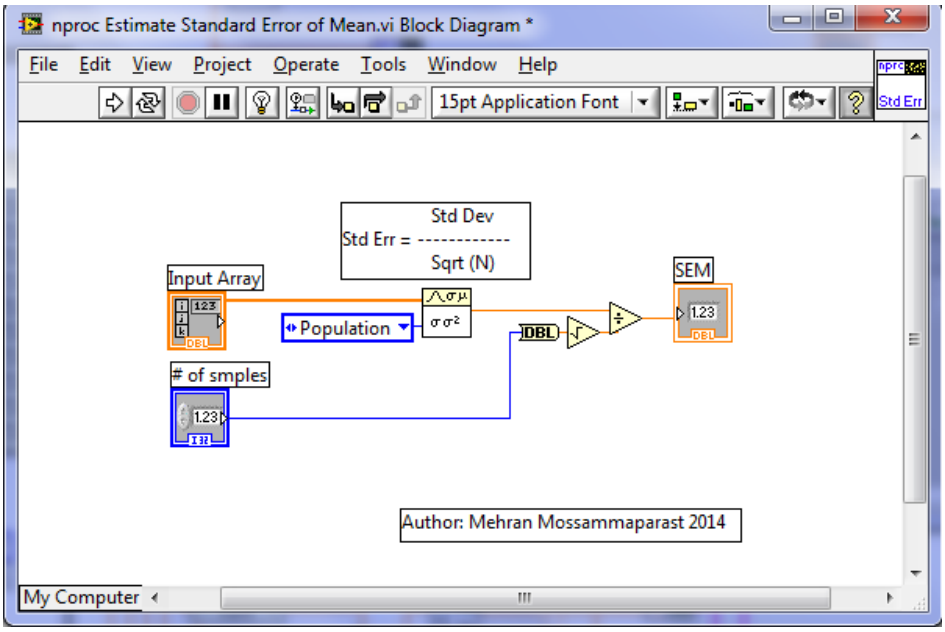

Figure 7-14 LabVIEW block diagram of the SEM algorithm

The Matlab codes have also been developed to simulate and compare the resolution capability of different types of radiometer discussed in this project. The top level diagram is shown in Figure 7-15.

```
function [ NAR_rad_resolution ] = FindNADResolution(tcal,BW,tau )

% Find resolution of an ideal,  NAC , NAR radiometers
% BW is band width in Hz and tau is Integration time in seconds
% eg FindNADResolution (1147932, 100000, 3600);
% Defining constants

narginchk(3,3);
ta=0:10:5000;
i=ones(size(ta));          % Initialising vector same size as ta
L1_dB = 1.2;               % Ins loss of the coupler/Dicke switch
Lcpl_dB = 11;              % Coupled loss of the 10dB coupler
L0_dB = 1.7;               % Insertion loss of the NA switch/att.
La_dB = 11;                % Attenuator setting in dB
trec = 90;                 % Receiver noise temperature of LNA in K
tref_C = 26.60;            % Reference temperature in Celsius
tref = tref_C + 274.15;    % Reference temperature in K
%% Calculating t'ref, tref measured at the coupler output
L1 = 10^(L1_dB/10);        % Insertion loss as a ratio
T1_K = tref;               % coupler/switch temperature
t1ref = tref/L1 + T1_K*(1-1/L1)  % Assuming a constant value
%% Calculating t"a, ta measured at the coupled output of the coupler

t2a = ta./L1 + T1_K*(1-1/L1);
%% Calculating t"cal, tcal measured at the coupler coupled output

Lcpl = 10^(Lcpl_dB/10);
L0 = 10^((La_dB+L0_dB)/10);  % Ins loss of att./switch as a ratio
T0_K = tref;                 % coupler/noise adding switch temp.
Tload = tref;                % Load resistor is the same as tref in
K.
t2noff = 1/Lcpl * (Tload/L0 + T0_K*(1-1/L0));
t2non = 1/Lcpl * (tcal/L0 + T0_K*(1-1/L0));
t2cal = t2non - t2noff ;     % Calibration noise source value
%

kappa = 1.380662*10^-23;            % Boltzman Constant
Boltzman_dBm=10*log10(kappa/0.001); % Boltzman Constant to dBm
MDS_ta = Boltzman_dBm + 10*log10(ta(:)) + 10*log10(BW); % in dBm
tcal_dBmpHz = Boltzman_dBm + 10*log10(tcal(:));
t2cal_dBmpHz = Boltzman_dBm + 10*log10(t2cal(:));
%

delta = 1/sqrt(BW*tau);
SW_a = 3/9;                  % Switching delay on Ant
SW_c = 3/9;                  % Switching delay on Calib.
SW_r = 3/9;                  % Switching delay on Reference
delta_a = delta*sqrt(1/SW_a);% Uncertainty in Antenna Temp.
delta_c = delta*sqrt(1/SW_c);% Uncertainty in Calib. Temp.
delta_r= delta*sqrt(1/SW_r);% Uncertainty in Reference Temp.

%% Defining different terms in the radiometer resolution
term_t2a  = sqrt((t2a(:) + trec).^2);
term_t1ref = sqrt((t2a(:) - t1ref).^2 *(1+(t1ref + trec)/t2cal)^2);
```

```
term_trec  = sqrt ((t1ref + trec)^2 *(((t2a(:)-t1ref)./t2cal)-
1).^2);
NAD_rad_res =
term_t2a.*delta_a+term_t1ref.*delta_c+term_trec.*delta_r;

[min_NAD,min_indices] = nanmin(NAD_rad_res);
[max_NAD,max_indices] = nanmax(NAD_rad_res);

IDEAL_rad_res = delta * ((t2a(:) + trec));
NAR_rad_res = 2*delta*((t2a(:) + trec).*(1+(t2a(:)+trec)/t2cal));
NAR_cal_res = 2 * delta * t2cal * (1+(t2a(:)+trec)/t2cal);
[max_NAR,max_NAR_indices] = nanmax(NAR_rad_res);

%% Printing data to screen
fprintf('T"(a),[T''(ref)+T(rec)],[T"(a)-T''(ref)],
        [T"(a)+T(rec)],NAD,NAR,IDEAL \n');
res_terms = [ta',term_trec, term_t1ref,term_t2a,
NAD_rad_res,NAR_rad_res,IDEAL_rad_res];
formatSpec = ' %8.4f ';
res_terms = num2str(res_terms,formatSpec)
fprintf('NAC Noise Source Parameters: T"noff = %6.2fK,
         T"non = %6.2fK. \n',t2noff, t2non);
fprintf('NAC Calibration Parameters: T"cal = %6.2fK / %6.2fdBm/Hz,
         Tcal = %6.2fdBm/Hz. \n',t2cal,t2cal_dBmpHz,tcal_dBmpHz);
fprintf('NAC Min Resolution of %6.2f mK at
         Ta:%6.0fK. \n',min_NAD*1000 , ta(min_indices));
fprintf('NAC Max Resolution of %6.2f mK at
         Ta:%6.0fK. \n',max_NAD*1000 , ta(max_indices));
fprintf('NAR Max Resolution of %6.2f mK at
         Ta:%6.0fK. \n',max_NAR*1000 , ta(max_NAR_indices));
%% Plotting
figure(1);subplot(211);
plot(ta,term_t2a,'-m','LineWidth',2);hold on;
plot(ta,term_t1ref,'-r','LineWidth',2);
plot(ta,term_trec,'-g','LineWidth',2);hold off;
legend('t2a+trec','t2a-t''ref','t''ref+trec');
legend('Location','NorthWest' );
title('NAC Terms');
set(get(gca,'title'),'FontWeight','bold');
xlabel('Antenna Temperature, Ta [K]');
set(gca, 'XTickMode', 'auto');
set(gca, 'XTickLabelMode', 'auto');
ylabel('Radiometer Resolution [K]');grid('on');

figure(1);subplot(212);
plot(ta,NAD_rad_res,'-b','LineWidth',2);hold on;
plot(ta,NAR_rad_res,'-r','LineWidth',2);
plot(ta,IDEAL_rad_res,'-m','LineWidth',2);hold off;

legend('Noise Adding Comparison (NAC)','Noise Adding (NA)','Ideal');
legend('Location','NorthWest' );
title('NAC vs NA vs Ideal Radiometer Resolution');
set(get(gca,'title'),'FontWeight','bold');
xlabel('Antenna Temperature, Ta [K]');
set(gca, 'XTickMode', 'auto');
set(gca, 'XTickLabelMode', 'auto');
ylabel('Radiometer Resolution [K]');grid('on');
figure(gcf);
```

Figure 7-15 Matlab code to compare the resolution of radiometers

7.4 Appendix D: LabVIEW Receiver Monitoring and Control

In this project, LabVIEW software programs have been developed under Windows platform to monitor and control the receiver status parameters through RS485 two wire differential signalling protocol. The communication can also be time stamped and logged for later post-processing. The programs have been used in the laboratory to communicate with, debug and calibrate the receiver modules prior to the deployment in the field.

Figure 7-16 and Figure 7-17 show the front panel and block diagram interfaces of the monitor program to communicate with and debug the individual receiver modules remotely. The front panel shows the status of the receiver module parameters graphically.

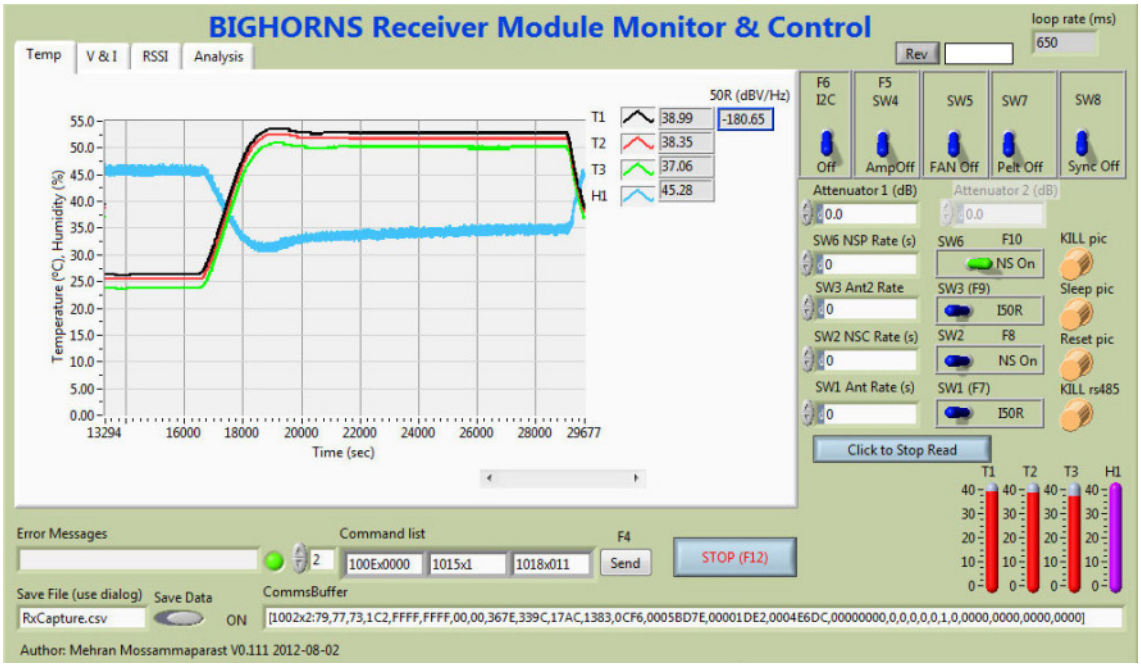

Figure 7-16 The receiver module monitoring & control – LabVIEW front panel

In the diagram above, the thermometers show the temperature of the radiometer components (T1), amplifiers (T2) and enclosure (T3) on the boards as well as internal humidity (H1) of the enclosure as marked in Figure 4-5 and Figure 4-10. The switches (SW1, SW2, SW3 and SW6) can be toggled manually or set to toggle automatically at pre-defined intervals by the user. In addition, SW8 can be used to synchronise Dicke (SW1) and noise adding radiometer (SW2/SW6) switches as shown in Figure 4-4 and Figure 4-5. The attenuator in the noise adding arm can be

programmed from 0 to 31.5 dB at 0.5 dB steps to adjust the excess noise temperature into the amplifiers.

In other receiver configuration, if thermoelectric Peltier module and external fan are installed and running for an active temperature controller, SW5 and SW7 can be used to toggle them on and off. The RF amplifiers in the second chain are also turned off by default but can be activated using SW4.

The micro-controller can be set to sleep mode during between each state of the switch to reduce any possible noise interferences. The data can also be saved to disk using Save Data button. Furthermore, once the receiver modules have been programmed remotely, the RS485 signalling may be disabled using Kill RS485 button on the front panel and turned off from the back-end rack. This can help reducing RFI picked up by the antenna which is caused by RS485 signalling when the RS485 cables lying on the ground. To recover from this mode the front-end module dc power needs to be cycled off and on.

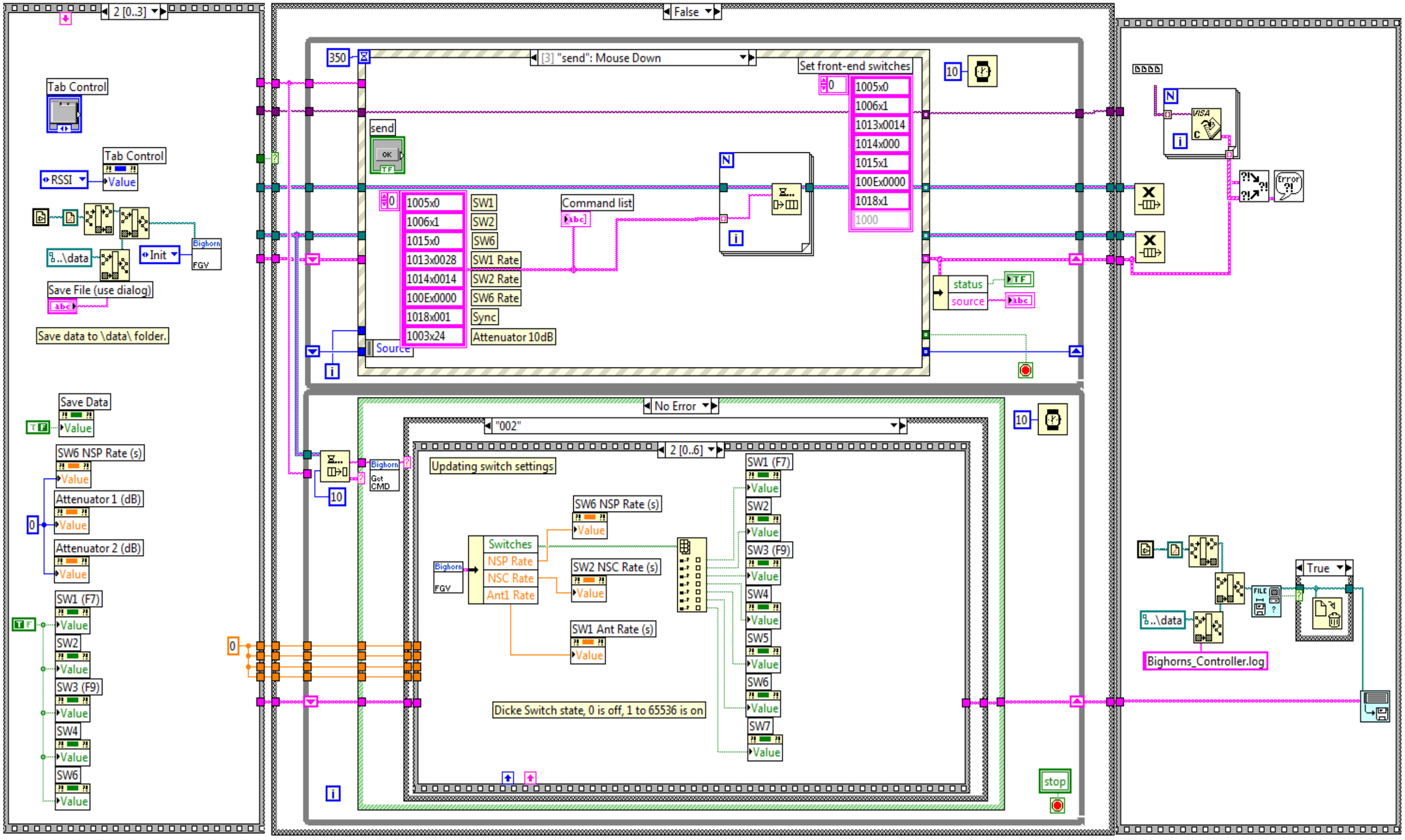

Figure 7-17 The receiver module monitoring & control - LabVIEW main block diagram

Figure 7-18 and Figure 7-19 show the front panel and block diagram interfaces of the program used to calibrate the full receiver chain which includes the frontend and gain modules. The diagram in Figure 7-18 shows the radiometer status at pre-defined intervals set by the user. The red thermometers display the current values of the temperature sensors for both receiver modules at 53ºC. The estimated values of Vref, Vref + ns, Vant, Vant + ns as measured by the gain module detector are shown on the right hand side in the diagram. Additionally, the plots show the radiometer temperature (in ºC) and measured antenna temperature (in K and dBm/Hz) values graphically while the receiver module were in a temperature chamber over a few hours.

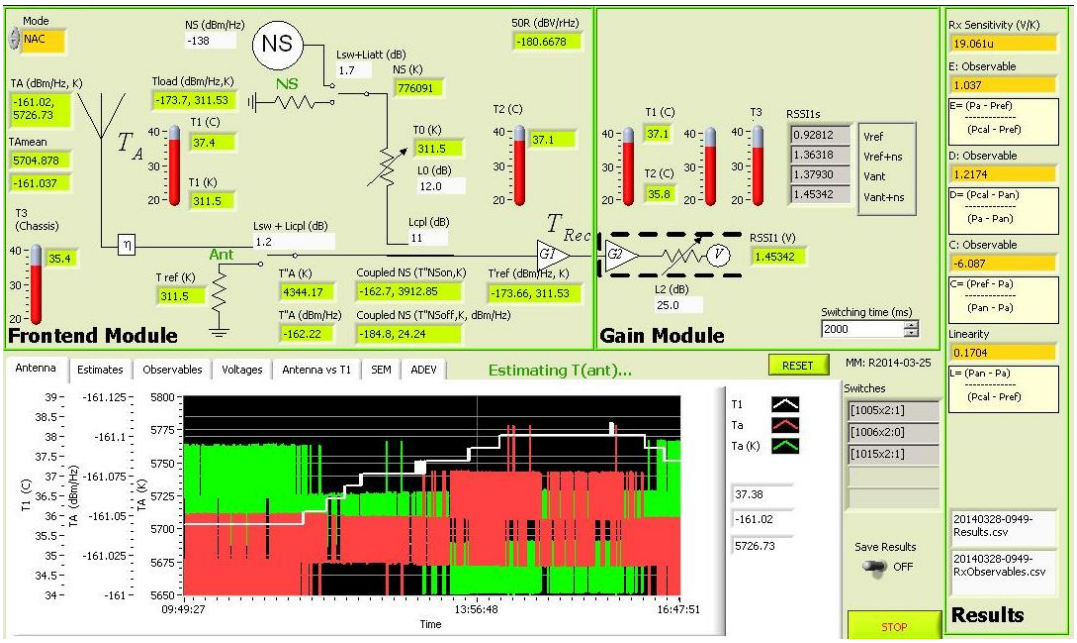

Figure 7-18 The radiometer calibration – LabVIEW front panel

Finally the specific command set developed to communicate with the receiver modules for this purpose is tabulated in Table 8 .

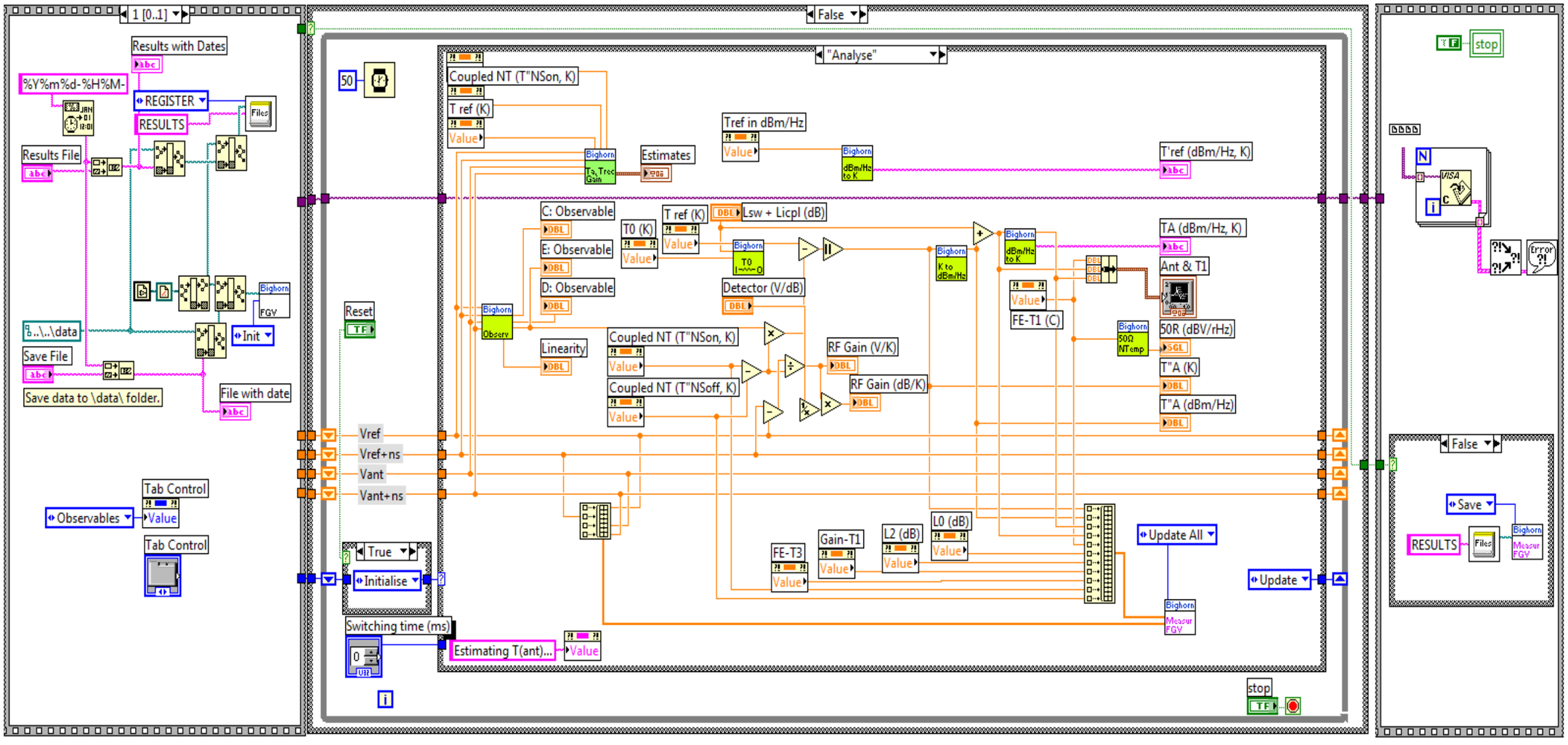

Figure 7-19 The radiometer calibration - LabVIEW main block diagram

Table 8 The BIGHORNS receiver module RS485 command set

Address	Description	Acknowledgement	Module	Update
M001	Request module serial number and software version	[M001xSVn.nnn]	FE/Gain	2012/07/01
M002	Request module serial number and its status	[M002xS: Status]	FE/Gain	2012/07/01
M003xnn	Sets module chain 1 attenuation	[M003xS:nn]	FE/Gain	2012/07/01
M004xnn	Sets module chain 2 attenuation	[M004xS:nn]	FE/Gain	2012/07/01
M005xn	Set SW1 to 0(Low/0V) or 1(High/5V) – Ch1 Ant/I50R	[M005xS:n]	FE	2012/07/01
M006xn	Set SW2 to 0(Low/0V) or 1(High/5V) – Ch1 NSC/50R	[M006xS:n]	FE	2012/07/01
M007xn	Set SW3 to 0(Low/0V) or 1(High/5V) – Ch2 Ant/I50R	[M007xS:n]	FE	2012/07/01
M008xn	Set SW4 to 0(Low/0V) or 1(High/5V) – Amps chain 2 Enable/Disable	[M008xS:n]	FE/Gain	2012/07/01
M009xn	Not yet used.	[M009xS:n]	FE	2012/06/01
M00A	Read Module Channel 1 RSSI. Not used.	[M00AxS:n]	Gain	2012/06/01
M00B	Read Module Channel 2 RSSI. Not used.	[M00BxS:n]	Gain	2012/06/01
M00C	Read voltages and currents V1,V2, ...,V5 (in mV) and I1, I2, …, I4 (in uA)	[M00CxS:vvvv, vvvv, vvvv, vvvv, vvvv, iiiiii, iiiiii, iiiiii, iiiiii]	FE/Gain	2012/07/01
M00Dxn	Set SW5, FAN switch, to 0(Low/0V) or 1(High/5V). Not implemented.	[M00DxS:n]	FE/Gain	2012/07/01
M00Exnnn	Set SW6 switching rate in steps of 0.5sec (counts from 0, 1, to 65536)	[M00ExS: nnnn]	FE	2012/07/01
M00F	Error Message	[M00FxS:n]	FE/Gain	2012/06/01

Address	Description	Acknowledgement	Module	Update
M010	Clear RS232 debug screen	[M010xS:n]	FE/Gain	2012/07/01
M011	Read ADC	[M011xS:n]	FE/Gain	2012/06/01
M012	Set PIC to SLEEP mode. Requires powering up the controller to re-start again.	[M012]	FE/Gain	2012/07/01
M013	Set SW1 Switching rate in steps of 0.5sec (counts from 0, 1, to 65536)	[M013xS: nnnn]	FE	2012/07/01
M014	Set SW2 Switching rate in steps of 0.5sec (counts from 0, 1, to 65536)	[M014xS: nnnn]	FE	2012/07/01
M015	Set SW6 (Enable/Disable regulator supplying dc voltage to the Noise Source) to 0(Low/0V) or 1(High/5V)	[M015xS:n]	FE	2012/07/01
M016	Set SW3 Switching rate in steps of 0.5sec (counts from 0, 1, to 65536)	[M016xS:n]	FE/Gain	2012/07/01
M017	Turn Peltier Control On or Off. Not implemented.	[M017xS:n]	FE/Gain	2012/06/01
M018	Synchronise toggling of switches (SW1 to Low/0, or High/1), (SW2 to Low/0, or High/1), (SW6 to Low/0, or High/1)	[M018xS:n]	FE/Gain	2012/07/01
M019	Turns off regulator supplying power to RS485 IC. Requires powering up the controller to re-start again.	[M019]	FE/Gain	2012/07/01
M020	Kills PIC and turns off RS485. Requires powering up the controller to re-start again.	[M020]	FE/Gain	2012/07/01
M0AA	Reset PIC	[M0AA]	FE/Gain	2012/08/15
M021.FFF	Available		-	2012/06/01

If opcode is not in range: [MFFFxS:NotValid,Error-nnn]

8 Bibliography

Ade, P. A. R., Aghanim, N., Armitage-Caplan, C., Arnaud, M., Ashdown, M., Atrio-Barandela, F., . . . Zonca, A. (2013). Planck 2013 results. XXIII. Isotropy and statistics of the CMB. *ArXiv e-prints, 1303*, 5083-5132. http://adsabs.harvard.edu/abs/2013arXiv1303.5083P doi:10.1051/0004-6361/201321534

Agilent Technologies. (2013). Operating and Service Manual for Agilent 346A/B/C Noise Source. *Agilent Technologies Products*. Retrieved from Agilent Technologies Document Library website: http://cp.literature.agilent.com/litweb/pdf/00346-90148.pdf

Allan, D. W. (1987). Time and Frequency (Time-Domain) Characterisation, Estimation, and prediction of Precision Clocks and Oscillators. *IEEE Transactions on Ultrasonics, Ferroelectrics, and Frequency Control, UFFC-34*(No. 6), 647-660.

Barkana, R., & Loeb, A. (2001). In the beginning: the first sources of light and the reionization of the universe. *Physics reports, 349*, 125-238.

Barkana, R., & Loeb, A. (2005). Detecting the Earliest Galaxies through Two New Sources of 21 Centimeter Fluctuations. *The Astrophysical Journal, 626*, 1-11.

Becker, R. H., Fan, X., Richard, L. W., Michael, A. S., Vijay, K. N., Robert, H. L., . . . York, D. G. (2001). Evidence for Reionization at z ~ 6: Detection of a Gunn-Peterson Trough in a z = 6.28 Quasar. *The Astronomical Journal, 122*(6), 2850.

Bennett, C. L., Banday, A. J., Gorski, K. M., Hinshaw, G., Jackson, P., Keegstra, P., . . . Wright, E. L. (1996). Four-Year COBE DMR Cosmic Microwave Background Observations: Maps and Basic Results. *The Astrophysical Journal Letters, 464*, L1. doi: 10.1086/310075

Bowman, J. D., & Rogers, A. E. E. (2010). A lower limit of $\Delta z>0.06$ for the duration of the reionization epoch. *Nature, 468*, 796-798.

Bowman, J. D., Rogers, A. E. E., & Hewitt, J. N. (2008). Toward Empirical Constraints on the Global Redshifted 21cm Brightness Temperature During the Epoch of Reionization. *The Astrophysical Journal, 676*(1), 1.

Briggs, F. (2012). *Pursuit of Primordial Hydrogen.* Paper presented at the CAASTRO EoR Global Signal Workshop - 19–21 Nov 2012, Sydney, Australia.

Burke, B. F., & Graham-Smith, F. S. (1997). *An introduction to Radio Astronomy*: Cambridge University Press.

Burns, J. O., Lazio, T. J. W., Bale, S. D., Bowman, J. D., Bradley, R. F., Carilli, C. L., . . . Pritchard, J. R. (2012). Probing the First Stars and Black Holes in the Early Universe with the Dark Ages Radio Explorer (DARE). *Advances in Space Research, 49*, 433-450. doi: 10.1016/j.asr.2011.10.014

Chippendale, A. P. (2009). *Detecting cosmological reionization on large scales through the 21 cm HI line.* (Doctor of Philosophy), University of Sydney, Australia. Retrieved from http://adsabs.harvard.edu/abs/2009PhDT.....301C

Ciardi, B., & Madau, P. (2003). Probing beyond the Epoch of Hydrogen Reionization with 21 Centimeter Radiation. *The Astrophysical Journal, 596*(1), 1.

Dicke, R. H. (1946). The Measurement of Thermal Radiation at Microwave Frequencies. *Review of Scientific Instruments, 17*(7), 268-275. doi: 10.1063/1.1770483

Ewen, H. I. (1951). Observation of a Line in the Galactic Radio Spectrum: Radiation from Galactic Hydrogen at 1,420 Mc./sec. *Nature, 168*(4270), 356. doi: 10.1038/168356a0

Fan, X., Carilli, C. L., & Keating, B. G. (2006). Observational Constraints on Cosmic Reionization. *Annual Review of Astronomy & Astrophysics, 44*, 415-462. doi: 10.1146/annurev.astro.44.051905.092514

Fan, X., Strauss, M. A., Becker, R. H., White, R. L., Gunn, J. E., Knapp, G. R., . . . Fukugita, M. (2006). Constraining the Evolution of the Ionizing Background and the Epoch of Reionization with z ~ 6 Quasars. II. A Sample of 19 Quasars. *The Astronomical Journal, 132*(1), 117.

Furlanetto, S., Oh, S. P., & Briggs, F. H. (2006). Cosmology at low frequencies: The 21cm transition and the high-redshift Universe. *Physics reports, 433*(4-6), 181-301.

Furlanetto, S. R., Lidz, A., Loeb, A., McQuinn, M., Pritchard, J. R., Alvarez, M. A., . . . Zaldarriaga, M. (2009). *Astrophysics from the Highly-Redshifted 21cm Line*. Paper presented at the astro2010: The Astronomy and Astrophysics Decadal Survey. http://adsabs.harvard.edu/abs/2009astro2010S..83F

Furlanetto, S. R., Zaldarriaga, M., & Hernquist, L. (2004). Statistical Probes of Reionization with 21 Centimeter Tomography. *The Astrophysical Journal, 613*, 16-22.

Gawiser, E., & Silk, J. (2000). The Cosmic Microwave Background Radiation. *Physics reports, 333*, 245-267. doi: 10.1016/S0370-1573(00)00025-9

Giovanelli, R., & Haynes, M. (1988). Extragalactic Neutral Hydrogen, *Galactic and Extragalactic Radio Astronomy* (pp. 522-562): Springer, US.

Gleser, L., Nusser, A., & Benson, A. J. (2008). De-contamination of cosmological 21-cm maps. *Monthly Notices of the Royal Astronomical Society, 391*(1), 383.

Gnedin, N. Y., & Shaver, P. A. (2004). Redshifted 21 Centimeter Emission from the Pre-Reionization Era. I. Mean Signal and Linear Fluctuations. *The Astrophysical Journal, 608*, 611-621.

Gunn, J. E., & Peterson, B. A. (1965). On the Density of Neutral Hydrogen in Intergalactic Space. *The Astrophysical Journal, 142*, 1633-1641. doi: 10.1086/148444

Haiman, Z., Knox, L., & Tegmark, M. (1999). *Reionization of the Intergalactic Medium and its Effect on the CMB*. Paper presented at the ASP Conference Series, Microwave Foregrounds, San Francisco, USA. http://adsabs.harvard.edu/abs/1999ASPC..181..227H

James, C. W., Ekers, R. D., Álvarez-Muñiz, J., Bray, J. D., McFadden, R. A., Phillips, C. J., . . . Roberts, P. (2010). LUNASKA experiments using the Australia Telescope Compact Array to search for ultrahigh energy neutrinos and develop technology for the lunar Cherenkov technique. *Physical Review D, 81*, 42003.

Jelic, V. (2010). *Cosmological 21cm experiments: Searching for a needle in a haystack*. Paper presented at the ISKAF2010 Science Meeting. http://adsabs.harvard.edu/abs/2010iska.meetE..28J

Jena, T., Norman, M. L., Tytler, D., Kirkman, D., Suzuki, N., Chapman, A., . . . Fechner, C. (2005). A Concordance model of the Lyman-alpha forest at z = 1.95. *Mon.Not.Roy.Astron.Soc., 361*, 70-96.

Keel, W. (2002, January 2010). William C. Keel Home Page. from http://www.astr.ua.edu/keel/agn/forest.html

Kerr, F. J. (1969). The Large-Scale Distribution of Hydrogen in the Galaxy. *Annual Review of Astronomy and Astrophysics, 7*(1), 39-66.

Komatsu, E., Smith, K. M., Dunkley, J., Bennett, C. L., Gold, B., Hinshaw, G., . . . Wright, E. L. (2011). Seven-year Wilkinson Microwave Anisotropy Probe (WMAP) Observations: Cosmological Interpretation. *The Astrophysical Journal Supplement Series, 192*(2), 18.

Kraus, J. D. (1986). *Radio Astronomy* (November 2004, 2nd ed.): Cygnus-Quasar Books.

Land, D. V., Levick, A. P., & Hand, J. W. (2007). The use of the Allan deviation for the measurement of the noise and drift performance of microwave radiometers. *Measurement Science and Technology, 18*(7), 1917. doi: 10.1088/0957-0233/18/7/018

Loeb, A., & Pritchard, J. R. (2012). 21 cm Cosmology in the 21st Century. *Reports on Progress in Physics, 75*, 086901. doi: 10.1088/0034-4885/75/8/086901

Loeb, A., & Zaldarriaga, M. (2004). Measuring the Small-Scale Power Spectrum of Cosmic Density Fluctuations through 21 cm Tomography Prior to the Epoch of Structure Formation. *Physical Review Letters, 92*(21), 211301.

Lonsdale, C. J., Cappallo, R. J., Morales, M. F., Briggs, F. H., Benkevitch, L., Bowman, J. D., . . . Williams, C. (2009). The Murchison Widefield Array: Design Overview. *Proceedings of the IEEE, 97*(8), 1497-1506. doi: 10.1109/JPROC.2009.2017564

McGreer, I. D., Mesinger, A., & Fan, X. (2011). The first (nearly) model-independent constraint on the neutral hydrogen fraction at z ˜ 6. *Monthly Notices of the Royal Astronomical Society, 415*, 3237-3246.

NASA WMAP Science Team. (2010a, Tuesday, 05-25-2010). Timeline of the Universe. from http://map.gsfc.nasa.gov/media/060915/060915_CMB_Timeline150.jpg

NASA WMAP Science Team. (2010b, Friday, 10-12-2010). WMAP9 Cosmic Microwave Background (CMB) Image. from http://wmap.gsfc.nasa.gov/media/121238/ilc_9yr_moll1024.png

Ohm, E. A., & Snell, W. W. (1963). A Radiometer for a Space Communications Receiver. *Bell System Technical Journal, 42*, 34. doi: 10.1002/j.1538-7305.1963.tb00959.x

Paciga, G., Chang, T.-C., Gupta, Y., Nityanada, R., Odegova, J., Pen, U.-L., . . . Sigurdson, K. (2011). The GMRT Epoch of Reionization experiment: A New upper limit on the neutral hydrogen power spectrum at z~8.6. *Mon.Not.Roy.Astron.Soc., 413*, 1174-1183.

Parsons, A. R., Backer, D. C., Bradley, R. F., Aguirre, J. E., Benoit, E. E., Carilli, C. L., . . . Wright, M. C. H. (2009). The Precision Array for Probing the Epoch of Reionization: 8 Station Results. *The Astronomical Journal, 139*(4), 1468-1480. doi: 10.1088/0004-6256/139/4/1468

Pradhan, A. K., & Nahar, S. N. (2011). *Atomic Astrophysics and Spectroscopy*: Cambridge University Press.

Pritchard, J. R., & Loeb, A. (2008). Evolution of the 21cm signal throughout cosmic history. *Physical Review D, 78*(10). doi: 10.1103/PhysRevD.78.103511

Pritchard, J. R., & Loeb, A. (2010). Constraining the unexplored period between the dark ages and reionization with observations of the global 21cm signal. *Physical Review D, 82*(2). doi: 10.1103/PhysRevD.82.023006

Rogers, A. E. E., & Bowman, J. D. (2008). Spectral Index of the Diffuse Radio Background Measured from 100 to 200 MHz. *The Astronomical Journal, 136*(2), 641-648. doi: 10.1088/0004-6256/136/2/641

Rogers, A. E. E., & Bowman, J. D. (2012). Absolute calibration of a wideband antenna and spectrometer for accurate sky noise temperature measurements. *Radio Science, 47*(4). doi: 10.1029/2011RS004962

Santos, G., Amblard, A., Pritchard, J., Trac, H., Cen, R., & Cooray, A. (2008). Cosmic Reionization and the 21cm Signal: Comparison between an Analytical Model and a Simulation. *The Astrophysical Journal, 689*(1), 1.

Santos, M. G., Silva, M. B., Pritchard, J. R., Cen, R., & Cooray, A. (2011). Probing the first galaxies with the SKA. *Astronomy & Astrophysics, 527*, 13 pp. doi: 10.1051/0004-6361/201015695

Schneider, R. (2004). The Cosmic Dawn: from first stars to the the observable universe. *Memorie della Societa Astronomica Italiana Supplementi, 5*, 307.

Seeds, M., & Backman, D. (2010). *Foundations of Astronomy* (11th ed.): Cengage Learning.

SeongYoup, S. (2004). A novel low-profile, dual-polarization, multi-band base-station antenna element - the fourpoint antenna. *IEEE 60th Vehicular Technology Conference, 1*, 225-229. doi: 10.1109/VETECF.2004.1399972

Shaver, P. A., & de Bruyn, A. G. (2000). *Steps to the Reionization Epoch*. Paper presented at the Perspectives on Radio Astronomy: Science with Large Antenna Arrays, Proceedings of the Conference held at the Royal Netherlands Academy of Arts and Sciences in Amsterdam on 7-9 April 1999, Amsterdam. http://adsabs.harvard.edu/abs/2000pras.conf...45S

Shaver, P. A., Windhorst, R. A., Madau, P., & de Bruyn, A. G. (1999). Can the reionization epoch be detected as a global signature in the cosmic background? *Astronomy and Astrophysics, 345*, 380-390.

Tingay, S. J., Goeke, R., Bowman, J. D., Emrich, D., Ord, S. M., Mitchell, D. A., . . . Wyithe, J. S. B. (2013). The Murchison Widefield Array: The Square Kilometre Array Precursor at Low Radio Frequencies. *Publications of the Astronomical Society of Australia, 30*, 21 pp. doi: 10.1017/pasa.2012.007

Tiuri, M. (1964). Radio Astronomy Receivers. *IEEE Transactions on Antennas and Propagation, 12*, 930-938. doi: 10.1109/TAP.1964.1138345

Ulaby, F. T., Fung, A. K., & Moore, R. K. (1981). *Microwave Remote Sensing: Active and Passive*: Addison-Wesley Publishing Company.

van Haarlem, M. P., Wise, M. W., Gunst, A. W., Heald, G., McKean, J. P., Hessels, J. W. T., . . . van Zwieten, J. (2013). LOFAR: The LOw-Frequency ARray. *Astronomy and Astrophysics, 556*, 53 pp. doi: 10.1051/0004-6361/201220873

Walker, G. (1989). Astronomical Observations: An Optical Perspective (pp. 319-320): Cambridge University Press. (Reprinted from: 1987).

Wilson, W. J., & Tanner, A. (2002). *Ultra Stable Microwave Radiometers for Future Sea Surface Salinity Missions*. Paper presented at the Earth Science Technology Conference - 11 & 13 June 2002, Pasadena, CA, USA. http://esto.nasa.gov/conferences/estc-2002/Papers/B2P5(Wilson).pdf

Zaldarriaga, M., Furlanetto, S. R., & Hernquist, L. (2004). 21 Centimeter Fluctuations from Cosmic Gas at High Redshifts. *The Astrophysical Journal, 608*(2), 622-635. doi: 10.1086/386327

Zaroubi, S. (2012). The Epoch of Reionization. *ArXiv e-prints*, 59. Retrieved from arxiv.org website: http://arxiv.org/pdf/1206.0267.pdf